

AFWL-TR-78-8

② LEVEL III

AFWL-TR-78-8

AD A0 66929

ADVANCED ADAPTIVE OPTICS  
CONTROL TECHNIQUES

Douglas P. Glasson  
Deb K. Guha

The Analytic Sciences Corporation  
Reading, MA 01867

January 1979

Final Report



DDC FILE COPY

Approved for public release; distribution unlimited.

DDC  
RECEIVED  
APR 5 1979  
B

AIR FORCE WEAPONS LABORATORY  
Air Force Systems Command  
Kirtland Air Force Base, NM 87117

79 03 26 128

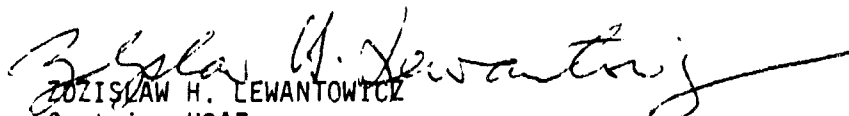
This final report was prepared by The Analytic Sciences Corporation, Reading, Massachusetts, under Contract F29601-77-C-0017, Job Order 33261806 with the Air Force Weapons Laboratory, Kirtland Air Force Base, New Mexico. Capt Zdzislaw H. Lewantowicz (ALO) was the Laboratory Project Officer-in-Charge.

When US Government drawings, specifications, or other data are used for any purpose other than a definitely related Government procurement operation, the Government thereby incurs no responsibility nor any obligation whatsoever, and the fact that the Government may have formulated, furnished, or in any way supplied the said drawings, specifications, or other data, is not to be regarded by implication or otherwise, as in any manner licensing the holder or any other person or corporation, or conveying any rights or permission to manufacture, use, or sell any patented invention that may in any way be related thereto.

This report has been authored by a contractor of the United States Government. Accordingly, the United States Government retains a nonexclusive, royalty-free license to publish or reproduce the material contained herein, or allow others to do so, for the United States Government purposes.

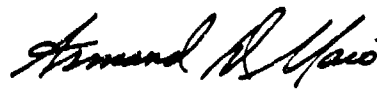
This report has been reviewed by the Information Office (OI) and is releasable to the National Technical Information Service (NTIS). At NTIS, it will be available to the general public including foreign nations.

This technical report has been reviewed and is approved for publication.

  
ZDZISLAW H. LEWANTOWICZ  
Captain, USAF  
Project Officer

  
JAMES D. DILLOW  
Lt Colonel, USAF  
Chief, Advanced Beam Control Branch

FOR THE COMMANDER

  
ARMAND D. MAIO  
Colonel, USAF  
Chief, Advanced Laser Technology Div

UNCLASSIFIED

SECURITY CLASSIFICATION OF THIS PAGE (When Data Entered)

REPORT DOCUMENTATION PAGE		READ INSTRUCTIONS BEFORE COMPLETING FORM
1. REPORT NUMBER AFWL-TR-78-8 ✓	2. GOVT ACCESSION NO.	3. RECIPIENT'S CATALOG NUMBER
4. TITLE (and Subtitle) ADVANCED ADAPTIVE OPTICS CONTROL TECHNIQUES	5. TYPE OF REPORT & PERIOD COVERED Final Report	
	6. PERFORMING ORG. REPORT NUMBER TR-996-1 ✓	
7. AUTHOR(s) Douglas P. Glasson, Deb K. Guha	8. CONTRACT OR GRANT NUMBER(s) F29601-77-C-0017	
	9. PERFORMING ORGANIZATION NAME AND ADDRESS The Analytic Sciences Corporation Reading, MA 01867	
11. CONTROLLING OFFICE NAME AND ADDRESS Air Force Weapons Laboratory (ALO) Kirtland Air Force Base, NM 87117	10. PROGRAM ELEMENT PROJECT, TASK AREA & WORK UNIT NUMBERS 62600F/33261806	
	12. REPORT DATE January 1979	
14. MONITORING AGENCY NAME & ADDRESS (if different from Controlling Office)	13. NUMBER OF PAGES 132	
	15. SECURITY CLASS. (of this report) UNCLASSIFIED	
16. DISTRIBUTION STATEMENT (of this Report) Approved for public release; distribution unlimited.		
17. DISTRIBUTION STATEMENT (of the abstract entered in Block 20. If different from Report)		
18. SUPPLEMENTARY NOTES		
19. KEY WORDS (Continue on reverse side if necessary and identify by block number) Adaptive Optics, High Energy Lasers, Kalman Filtering, Optimal Estimation, Optimal Control.		
20. ABSTRACT (Continue on reverse side if necessary and identify by block number) Optimal estimation and control methods for high energy laser adaptive optics systems are described. Three system types are examined: Active Multidither (AMD), Phase Conjugate (PC), and Beam Cleanup (BC). Sources of phasefront distortion considered include: atmospheric turbulence, backscatter speckle, base vibration, and mirror thermal distortion. Kalman-type digital algorithms for phasefront aberration estimation are developed and evaluated through computer simulation; performance		

DD FORM 1473 1 JAN 73 EDITION OF 1 NOV 68 IS OBSOLETE

UNCLASSIFIED

SECURITY CLASSIFICATION OF THIS PAGE (When Data Entered)

79 03 26 128

UNCLASSIFIED

SECURITY CLASSIFICATION OF THIS PAGE (When Data Entered)

BLOCK 20. ABSTRACT (CONT'D)

comparisons with classical estimation approaches are provided. Optimal feedback-feedforward controllers are designed for the active system components; performance comparisons with classical designs and sensitivity studies related to disturbance model mismatches and active component bandwidth are presented. Results of integrated estimation and control simulations are evaluated. Areas for further refinement of the adaptive optics approaches and potential system implementations are recommended.

ACCESSION for	
NTIS	White Section <input checked="" type="checkbox"/>
DDC	Buff Section <input type="checkbox"/>
UNANNOUNCED	<input type="checkbox"/>
JUSTIFICATION	
BY	
DISTRIBUTION/AVAILABILITY CODES	
Dist.	AVAIL. and/or SPECIAL
A	

UNCLASSIFIED

SECURITY CLASSIFICATION OF THIS PAGE (When Data Entered)

## TABLE OF CONTENTS

<u>Section</u>	<u>Page No.</u>
1. INTRODUCTION	
1.1 Motivation for Modern Estimation and Control in Adaptive Optics	1
1.2 Estimation and Control Approach	7
1.3 Overview of the Report	9
2. MODELS FOR ADAPTIVE OPTICS CONCEPTS	11
2.1 System Models	11
2.1.1 Active Multidither	11
2.1.2 Phase Conjugate	14
2.2 Optical Component Models	16
2.2.1 Tilt Mirror Model	16
2.2.2 Focus Mirror Model	18
2.2.3 Deformable Mirror Model	21
2.2.4 Laser Phasefront Model	23
2.2.5 Thermal Distortion Model	23
2.2.6 Laser-Induced Vibration Model	25
2.2.7 Relay Mirror Jitter Model	26
2.2.8 Sensor Models	28
2.3 Atmospheric Propagation Effects	29
2.3.1 Atmospheric Turbulence Models	29
2.3.2 Intensity at Target	29
2.3.3 Target Effects	31
3. MODE ESTIMATION IN ADAPTIVE OPTICS	34
3.1 Active Multidither	34
3.2 Phase Conjugate	40
3.2.1 Least Square Fit	41
3.2.2 Least Square Fit Followed by Low Pass Filter	41
3.2.3 Kalman Filter	42
3.3 Evaluation of the Estimation Algorithms	44
3.3.1 Active Multidither	44
3.3.2 Phase Conjugate	46
4. OPTIMAL CONTROL IN ADAPTIVE OPTICS	48
4.1 Introduction	48
4.2 Optimal Disturbance Nulling Control	49
4.3 Performance Indices for Adaptive Optics Control Design	53
4.3.1 Development of the State Penalty Matrix, Q	54
4.3.2 Development of the Control Penalty Matrix, R	58

TABLE OF CONTENTS (Continued)

	Page <u>No.</u>
4.4 Inner Loop Design - Tilt and Focus Mirrors	58
4.4.1 Control Objectives - Performance Indices	58
4.4.2 The Solution Technique	59
4.5 Deformable Mirror Controller Design	63
4.5.1 Psuedo-Optimal Control Design	64
4.5.2 The Mathematical Design Procedure	64
4.5.3 Description of the Deformable Mirror Controller	67
4.6 Preliminary Performance Evaluation	69
4.6.1 Tilt Channel Performance/Sensitivity	70
4.6.2 Deformable Mirror Control Evaluation	74
5. INTEGRATED ESTIMATION-CONTROL SIMULATION RESULTS	80
5.1 Integrated Phase Conjugate System Results	80
5.2 Integrated Active Multidither system	83
5.2.1 Test Cases and Simulation Results	83
5.2.2 Filter Divergence	85
6. BEAM CLEANUP SYSTEM	90
6.1 Optimum Error Budget	90
6.2 The Beam Cleanup Control System/Simula- tion Model	93
6.3 Beam Cleanup Simulation	95
6.3.1 Test Case Parameters	95
6.3.2 Simulation Results	95
6.4 Chapter Summary	100
7. SUMMARY	101
7.1 Results	101
7.2 Recommendations	103
REFERENCES	108
APPENDIX A ADAPTIVE OPTICS MODEL PARAMETER VALUES	110

## LIST OF FIGURES

<u>Figure No.</u>		<u>Page No.</u>
1.1-1	Phase Conjugate/Beam Cleanup	3
1.1-2	Active Multidither	4
1.2-1	Optimal Estimation - Control Block Diagram for Adaptive Optics System	8
1.2-2	Separation of Estimation and Control Syntheses	9
2.1-1	Active Multidither Model	12
2.1-2	Phase Conjugate System	15
2.2-1	Tilt Mirror Mechanical Model and Variable Definition for Mirror Pitch Motion	17
2.2-2	Focus Mirror Mechanical Model	19
2.2-3	Laser Induced Vibration Spectrum and Model Approximation	26
2.2-4	Assumed Relay Mirror Layout	27
2.3-1	Turbulence Spectral Representation	30
2.3-2	Turbulence Dynamic Model	30
2.3-3	Speckle Dynamic Model	32
2.3-4	Speckle Filter Approximation	33
3.3-1	Phase Conjugate	47
4.2-1	Disturbance Nulling Control Structure	49
4.2-2	Equivalent Optimal Regulator Structure	50
4.5-1	Deformable Mirror Controller	65
4.5-2	Optimal Model Following (Nulling) Control Structure	65
4.5-3	Functional Block Diagram of Two-Distur- bance Controller	68
4.5-4	Mathematical Block Diagram of Two-Distur- bance Controller	68
4.6-1	Optimal Model Following Controller for Turbulence-Induced Tilt	70
4.6-2	Classical Direct-Command Controller	70
4.6-3	Nulling Error Comparison Between Classical and Optimal Controllers	71

LIST OF FIGURES (Continued)

<u>Figure No.</u>		<u>Page No.</u>
4.6-4	Nulling Error Variance Versus Tilt Mirror Bandwidth	72
4.6-5	Tilt Channel Mismatch Sensitivity	73
4.6-6	Disturbance and Deformable Mirror Time Histories	75
4.6-7	Deformable Mirror Optimal Control System	76
4.6-8	Classical Inverse Filter Control System	76
4.6-9	Astigmatism Nulling Error Variances	79
4.6-10	Focus Cross-Coupling	79
4.6-11	Normalized Intensity Degradation	79
5.1-1	Phase Conjugate System Performance	81
5.2-1	Integrated AMD Performance, Range = 500 km	84
5.2-2	Integrated AMD Performance, Range = 100 km	85
5.2-3(a)	Divergent Filter Time History	86
5.2-3(b)	Divergent Filter Time History (Continued)	87
5.2-3(c)	Divergent Filter Time History (Continued)	87
6.2-1	Beam Cleanup Control System	94
6.3-1	Phasefront Disturbance Spectrum	96
6.3-2	Beam Cleanup System Performance	97
6.3-3	Gaussian Intensity Pattern and Quadratic Approximation	98
A.1-1	Tilt Mirror Mechanical Model and Variable Definition for Mirror Pitch Motion	A-1
A.1-2	Focus Mirror Mechanical Model	A-3
A.1-3	Laser Induced Vibration Spectrum and Model Approximation	A-7
A.1-4	PDF for Relay Mirror Vibration Gains	A-7
A.2-1	Speckle Dynamic Model	A-11



LIST OF TABLES

<u>Table No.</u>		<u>Page No.</u>
2.1-1	Implemented Optical Modes	13
2.2-1	Tilt Mirror Model Parameters	17
2.2-2	Focus Mirror Model Parameters	20
3.3-1	Turbulence Parameters (AMD)	45
3.3-2	AMD With Point Target	45
3.3-3	AMD With Speckle Return	46
3.3-4	Turbulence Parameters (PC)	46
5.2-1	Estimation Errors for Divergent and Fixed Filters	88
6.3-1	Radiation Wavelengths and Power Levels	95
6.3-2	Disturbance Spectra Parameters	96
A.1-1	Tilt Mirror Model Parameters	A-2
A.1-2	Focus Mirror Model Parameters	A-3
A.1-3	Deformable Mirror Model Parameters	A-4
A.1-4	Thermal Deformation Model Parameters	A-6
A.1-5	Relay Mirror Jitter Model Parameters	A-3
A.1-6	Beam Expander Parameters	A-9
A.2-1	Shaping Filter Parameters for AMD	A-10
A.2-2	Shaping Filter Parameters for PC	A-10
A.2-3	Receiver Model Parameters	A-12

1.

## INTRODUCTION

### 1.1 MOTIVATION FOR MODERN ESTIMATION AND CONTROL IN ADAPTIVE OPTICS

Adaptive optics concepts and technology have stimulated efforts among members of the laser, surveillance, and astronomy communities. Classical optical systems designed for such applications have reflected the premium put on optical precision. As a consequence, these systems have characteristically been heavy, larger than necessary, and very expensive. They also have been incapable of compensating for the effects of the atmosphere. Adaptive optics have the potential to ameliorate most of these drawbacks because they are designed to sense and correct optical system phasefront aberrations. Such devices permit relaxation of requirements for optical precision, thereby reducing their weight, cost, and size and can eliminate blur and power dissipation caused by the atmosphere.

The method for phasefront sensing varies among adaptive optics systems which have been implemented. Direct phasefront measurement of either backscattered energy from a target or target thermal radiation is possible, as is the inference of phasefront via observation of the effect of probe signals on signal strength at a target (active illumination) or the strength of a signal recovered from a passively radiating source. For both phasefront sensing schemes, however, the method of correcting phasefront is based upon radiation received from the target; dynamic optics (tilt mirrors for tilt errors, relative displacement of secondary and primary

mirrors in beam expanders for focus errors, and deformable mirrors for either or both tilt and focus plus higher-order aberration correction) are positioned to implement the corrections. For the direct measurement (phase conjugate) system, however, the optical path over which the phase measurement is made must be the same as that over which the correction is implemented. It is then assumed that the conjugate of the measurement will correct for the aberrations. In the direct or intensity measurement/probe signal (active multidither) scheme, the intensity can be collected over a different optical path.

Possible adaptive optics implementations in a conceptual system for maximizing high energy laser (HEL) flux density are shown in Figs. 1.1-1 and 1.1-2. The phase conjugate implementation (Fig. 1.1-1) is for a passively radiating target; energy is collected at a different wavelength than that transmitted by the HEL. The target radiation propagates through the shared optical train to a beamsplitter which reflects the target energy in a different direction than the outgoing HEL wavefront. The split target radiation is then imaged, spatially sampled, and processed to provide phase-front corrections which are implemented by the dynamic optical components, and presumably compensate for all aberrations introduced between the target and the sensor.

The phase conjugate concept will not correct for flux density loss at the target due to HEL beam aberrations. An additional beam cleanup system is included in Fig. 1.1-1 for this purpose. It includes a sensor to measure the HEL output phasefront and, possibly, a separate deformable mirror to correct it, although it appears that such corrections could be combined with those from the phase conjugate device and implemented by its dynamic optics.

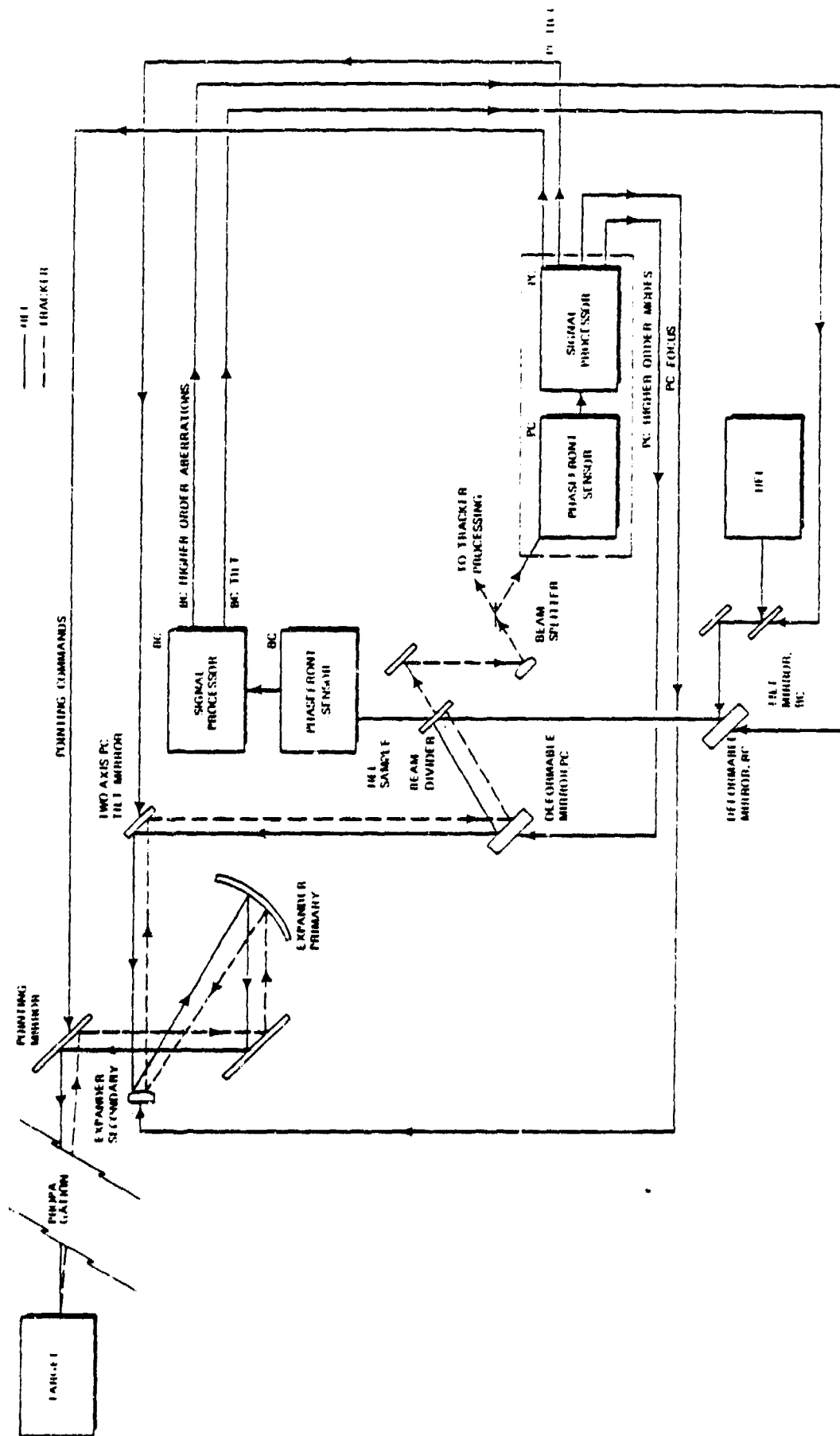


Figure 1.1-1 Phase Conjugate/Beam Cleanup

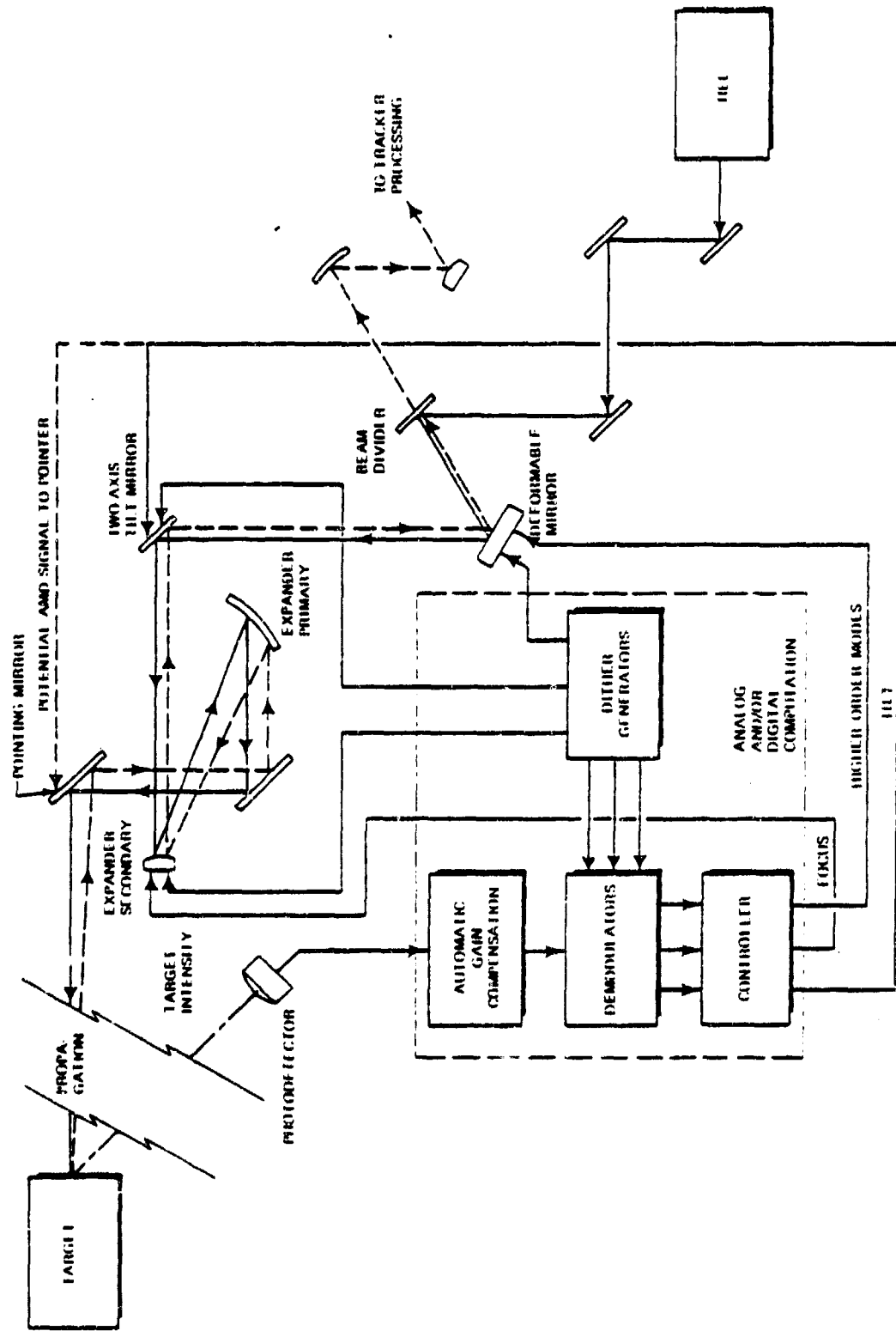


Figure 1.1-2 Active Multither

In Fig. 1.1-2 an active multidither scheme has been substituted for both the phase conjugate and beam cleanup systems. Active multidither first modulates the outgoing HEL phasefront with probe (dither) signals via the active optics. It then collects HEL energy reflected from the target and determines the effect of the dither on that intensity. If, for example, increasing the amplitude (during the positive part of the dither cycle) of a mode shape implemented on the deformable mirror increases the strength of the target return slightly, then the amplitude of that mode should be made greater to compensate for phasefront aberrations. In this way, the active multidither "hill climbs" its way to maximizing intensity on target or, equivalently, to eliminating the effect of phasefront aberrations existing in the HEL beam and created in the propagation path between the beam and the target.

Adaptive optics concepts, although promising, are far from being devoid of problems. In fact, the noisy, coupled-multivariable, time varying, potentially nonlinear, high order, and distributed (space/time) characteristics of such devices challenge the most competent controls engineer. Phase conjugate sensors are noisy and their noise properties correlate with the intensity of the received radiation, which changes because of HEL heating and the amount of aberration introduced by the system optics and atmosphere. Ambient radiation also introduces noise in these sensors. Beam cleanup sensors must contend with their internal noise and the rapidly varying intensity from the HEL. For both sensors the number of phasefront samples across the beam may be limited since, for a given strength of the sampled beam, the phasefront detector outputs decrease as the beam size is increased and/or the detector size is decreased. Active multidither sensor outputs are corrupted from internal noise, collected ambient radiation, HEL intensity variations in the target backscattered

energy and speckle. Speckle is an intensity variation characteristic of coherent radiation introduced by the non-specular nature of the target, and it can introduce severe levels of return signal modulation. Such modulation is a function of target parameters and beam spot size at the target.

In addition to the estimation problem resulting from such noise effects, the control of phasefront aberrations is difficult because multiple controlled optical elements (and potentially multiple coupled controlled elements within them, e.g., the deformable mirror) are required, which may have nonlinear dynamics. The actual position of a deformable mirror surface, in response to input commands, may not be known. Also, the control system gain in an active multidither system can vary depending on the degree of convergence of the HEL optical system. Obviously, any estimation and control structures for adaptive optics must provide good performance in the presence of the varying noise and system dynamic properties.

Modern estimation and control techniques are well suited to the solution of the problem areas described for adaptive optics systems. Kalman-type estimators, e.g., Kalman, extended Kalman, and adaptive filters, can provide optimal or near-optimal estimates of phasefronts. Correspondingly, optimal control methodology can provide control structures which derive the best possible performance from a system and equally as important, can define which variables and parameters are most important to providing good system response and how they must be varied to reduce the phasefront errors.

In the present study, the three adaptive optics system types (phase conjugate, beam cleanup, and active multidither) have been modeled and optimal estimation and control structures have been designed and evaluated for each.

## 1.2 ESTIMATION AND CONTROL APPROACH

Figure 1.2-1 illustrates the modern estimation and control approach of the present study. The environmental disturbances are characterized by a truth model. For example, turbulence spectra provided by AFWL (Ref. 1) were approximated by linear Gauss-Markov models, i.e., linear filters driven by white noise. Those truth model states which degrade the performance (target intensity) of the system are extracted by the  $H_1^T$  matrix and added to the active optics outputs which attempt to counteract these disturbances. A sensor measures the disturbed wavefront, or the effect of the wavefront disturbances on target intensity. A Kalman-type filter uses the measurement,  $\underline{y}$ , and the assumed truth model dynamics to derive a statistically optimal estimate of the truth model states,  $\hat{\underline{z}}$ . Statistically optimal implies that the Kalman filter establishes the best balance between the uncertainty of the measurement due to sensor noise and the uncertainty of the random process it is attempting to estimate. It is also significant that the Kalman filter computes an estimate of the full disturbance state; for example, if a turbulence aberration is characterized by a third order Markov model, the Kalman filter estimates the magnitude of the aberration as well as two states related to the time derivatives of the aberration. The derivative states can be used to advantage in computing controls since they give some indication of the future evolution of the disturbance process. The control gain matrix,  $K^T$ , computes the optimal linear combination of disturbance magnitude and derivative states to produce the control commands to the active optics components.

In a system design that involves linear plant and disturbance dynamics, a quadratic performance index, and Gaussian noise statistics, the separation theorem (Ref. 2)



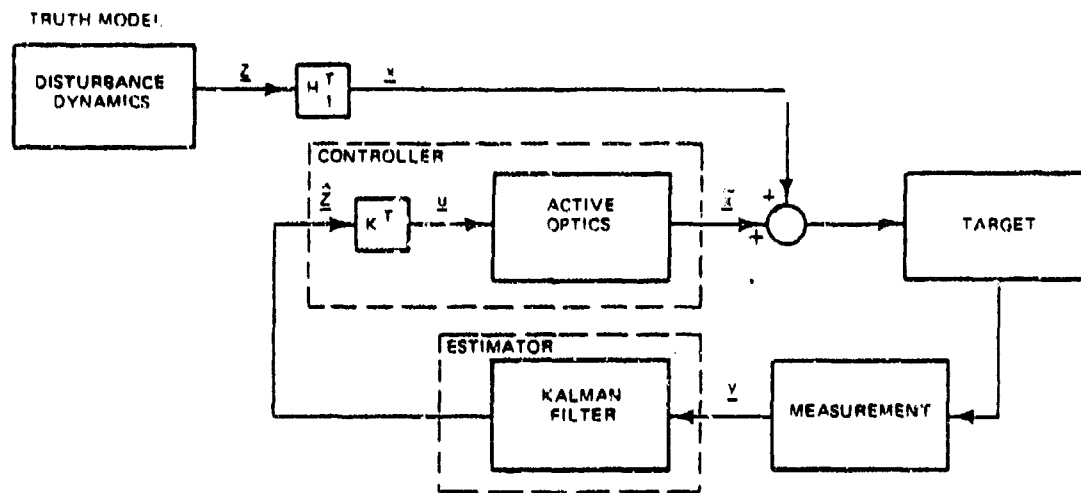


Figure 1.2-1 Optimal Estimation - Control Block Diagram for Adaptive Optics System

allows the estimation and control syntheses to be performed independently. Figure 1.2-2 illustrates the application of this theorem to the present study. In estimation design and development, perfect control is assumed (i.e., instantaneous response of the active optics); the control design is carried out assuming perfect state estimation (i.e., estimated states are identical to truth states). In the context of modern estimation and control synthesis, AMD and PC are alternative estimation methods; the optimal control design approach applies to both the AMD and PC systems.

It should be noted that the nonlinear measurement involved in the AMD system precludes dogmatic application of the separation theorem. Separation of the estimation and control syntheses is a practical, though approximate,

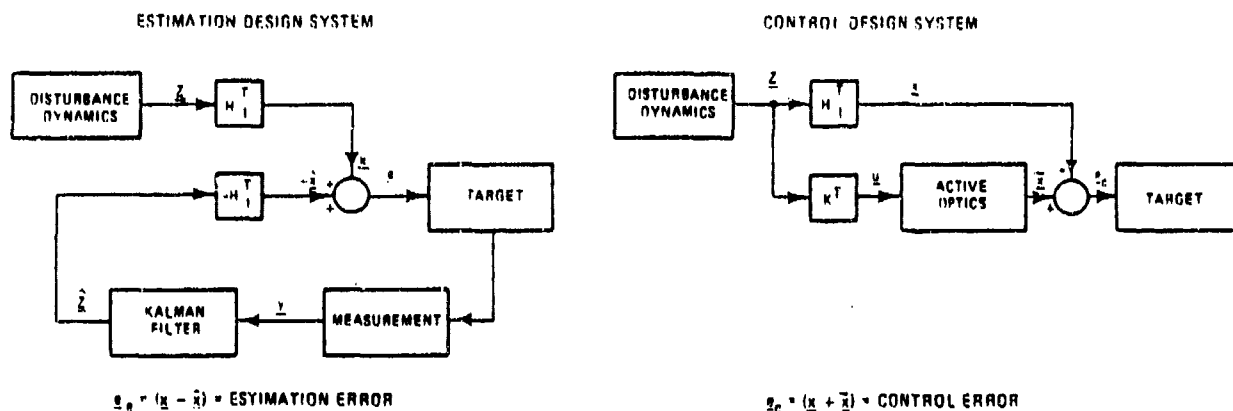


Figure 1.2-2 Separation of Estimation and Control Syntheses

design technique; computer simulation of the integrated estimation and control system validates the success (or failure) of the system.

### 1.3 OVERVIEW OF THE REPORT

Chapter 2 of this report outlines the active optics and environmental disturbance models used in the present study; relevant parameter values are presented in Appendix A. The AMD and PC estimation algorithms are described in Chapter 3; alternative classical estimation techniques for PC are also described. Optimal disturbance nulling control and its application to the tilt, focus, and deformable mirror control channels are covered in Chapter 4. Chapters 3 and 4 also include preliminary performance evaluations for the estimation with perfect control and control with perfect estimation cases, respectively. Computer simulation results for the integrated estimation and control system evaluation are presented in

Chapter 5. The beam cleanup (BC) system is addressed in Chapter 6; optimization of a three spectral line control system is described, and simulation results for a candidate system are presented. Chapter 7 presents the conclusions and a discussion of areas for further refinement of the adaptive optics system and controller.

2.

## MODELS FOR ADAPTIVE OPTICS CONCEPTS

In this chapter, the mathematical models used in adaptive optics estimation and control algorithm development are described. The models are divided into two major subsets according to whether a particular model simulates an adaptive optics system component (such as a mirror) or an environmental effect (such as beam diffraction effects in propagation). The majority of the models are common to both the AMD and PC systems; the only significant differences between the two systems are the type of sensor used, the distribution of thermal distortion effects, and the target effects modeled.

The models used in this study were simplified to be compatible with control synthesis; the models do, however, include all important phenomena observed in breadboard tests or implied by recent analysis results. Parameter values and control specifications (which are listed in Appendix A) have been chosen to reflect the current state-of-the-art in hardware development.

### 2.1 SYSTEM MODELS

#### 2.1.1 Active Multidither

The component models and component interactions for Active Multidither (AMD) simulation are shown in Fig. 2.1-1. The adaptive optics system consists of the high energy laser (HEL), a deformable mirror, a two axis tilt mirror, a focus mirror, and a photodetector sensing element. Disturbances

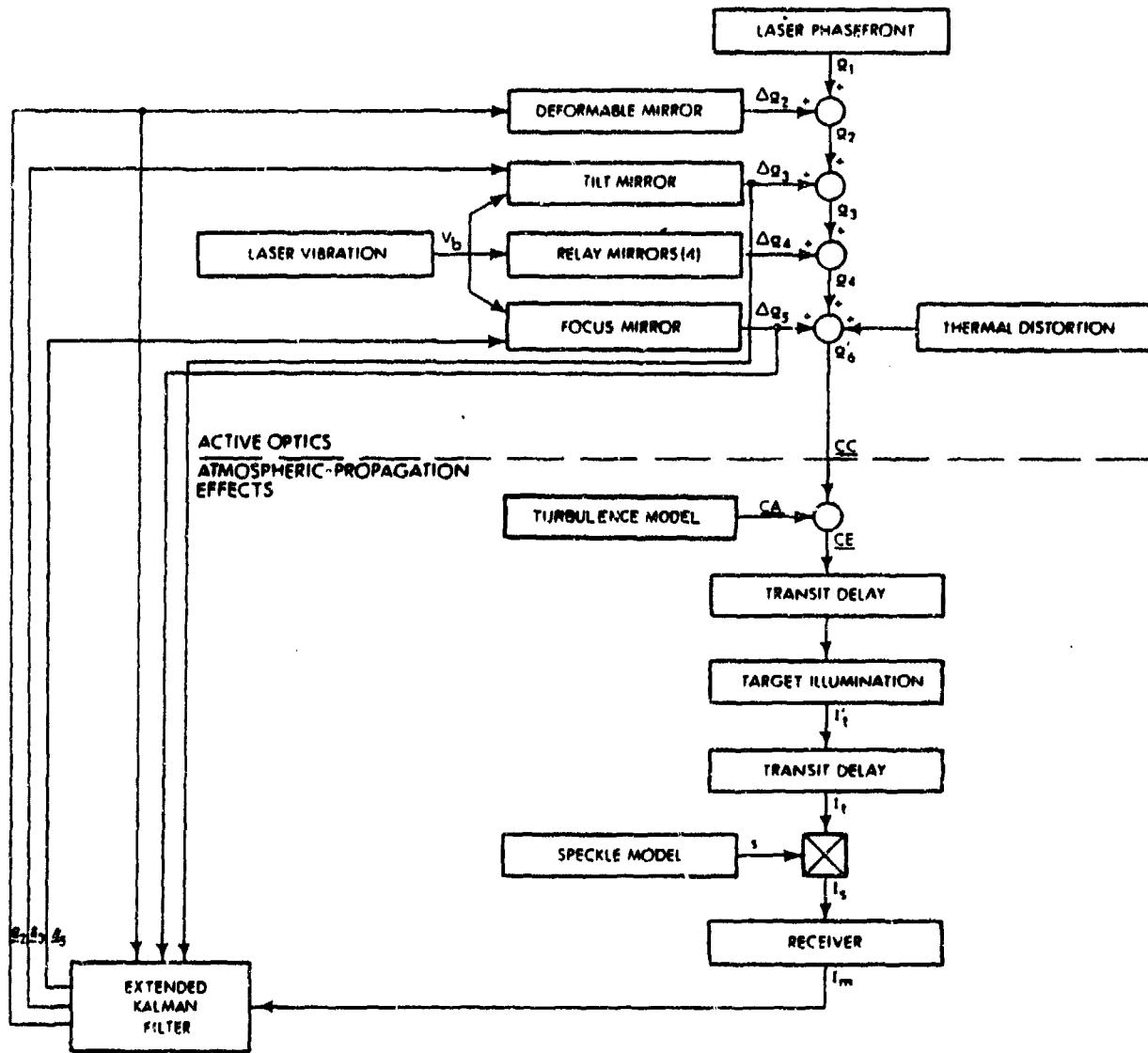


Figure 2.1-1 Active Multidither Model

within the adaptive optics system due to mechanical vibration and mirror heating are generated by the Vibration and Thermal Distortion models, respectively. Atmospheric turbulence and beam propagation effects are considered in the Turbulence and Target Illumination models. Effects of target surface

properties are provided by the Speckle model; the Photodetector model includes the effects of background radiation and internal noise. Transit delays from beam propagation to the target and return to the receiver are also included in the AMD system model.

The phase aberration function, which represents the perturbation of the outgoing wavefront from that of an ideal converging spherical wave, is expressed in terms of Zernike circle functions (Ref. 1), i.e.

$$\phi(x,y) = \frac{2\pi}{\lambda} \sum_{i=1}^{\infty} c_i P_i(x,y) \quad (2.1-1)$$

where:

- $\phi(x,y)$  = the phase aberration function
- $P_i(x,y)$  = the  $i^{\text{th}}$  Zernike circle function
- $c_i$  = the  $i^{\text{th}}$  Zernike coefficient

The expansion of Eq. 2.1-1 is truncated at five terms; the  $P_i$ 's for these five terms are listed in Table 2.1-1.

TABLE 2.1-1  
IMPLEMENTED OPTICAL MODES

T-1755

RELATIONSHIP	OPTICAL MODE SHAPE
$P_1 = x$	Pitch Tilt
$P_2 = y$	Yaw Tilt
$P_3 = x^2 + y^2$	Focus
$P_4 = x^2 - y^2$	Astigmatism
$P_5 = xy$	

The variables  $x$  and  $y$  are distances from the beam center nondimensionalized by the aperture radius, i.e.

$$x = \frac{x_0}{R_{\text{aperture}}} \quad (2.1-2)$$

The intensity measurement of the receiver, the position transducer outputs of the tilt and focus mirrors, and the input command to the deformable mirror are supplied to a digital extended Kalman filter. The state estimates generated by the Kalman filter are the inputs to the active optics components; the sample and hold and analog controller functions are included within the deformable mirror, tilt mirror, and focus mirror modules.

#### 2.1.2 Phase Conjugate

The models and interactions of the Phase Conjugate (PC) system are shown in Fig. 2.1-2. The component and environment models used in the Phase Conjugate system model are quite similar to those of the AMD system; the only significant differences between the two system models are

- The receiver model is a "black box" representation of a shearing interferometer as opposed to a photodetector in the AMD system
- Thermal distortion effects are simulated by two distinct models; a separate model is provided for those optical components which are part of the shared aperture optical train
- Target effects (speckle) do not influence receiver performance.

In phase conjugate adaptive optics a shearing interferometer measures the incoming wave phasefront at the shared aperture exit pupil. As indicated by Fig. 2.1-2

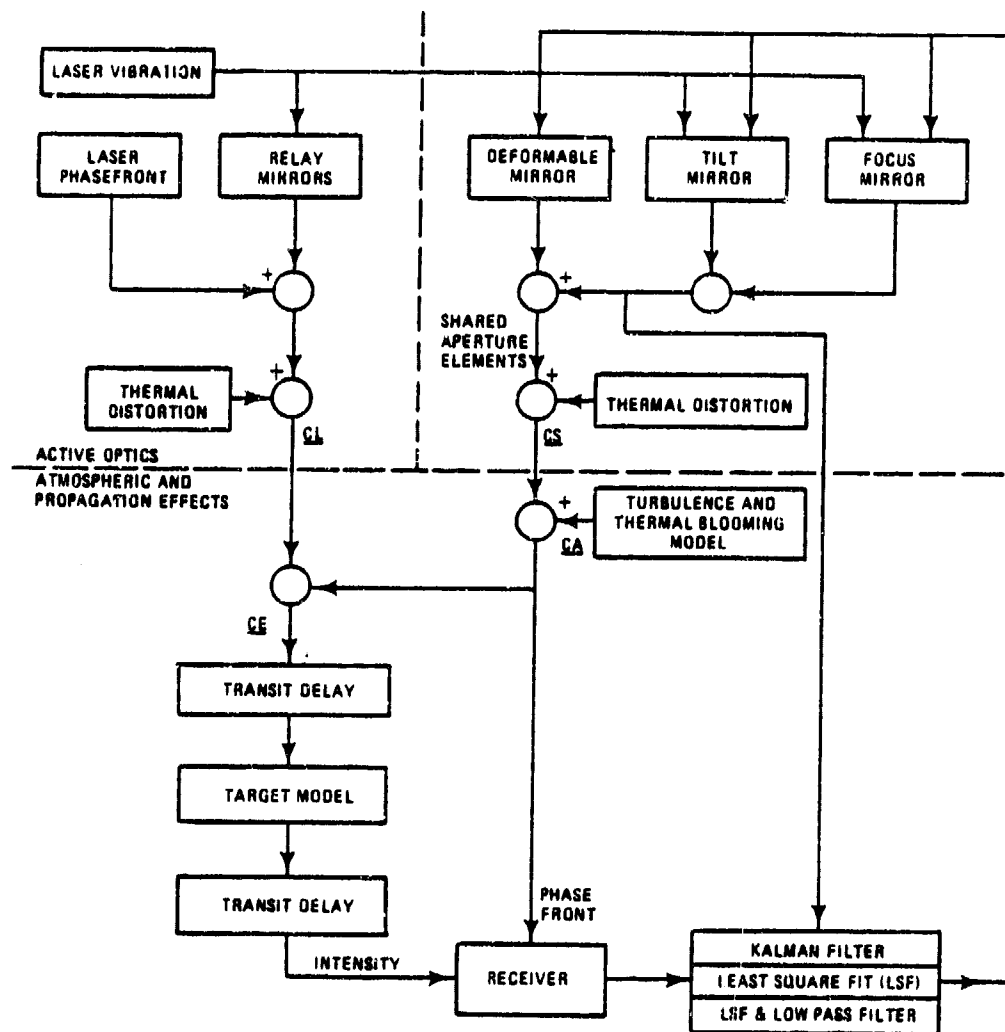


Figure 2.1-2 Phase Conjugate System

this incoming wave is generated by a point source model of the target; in addition to the passive target radiation, laser illumination effects can influence (increase) the signal level at the receiver. Since the incoming wave passes through the shared aperture optical train before



reaching the shearing interferometer, it is affected by thermal distortions of the shared aperture components, i.e., the tilt, focus, and deformable mirrors. Thermal distortions of the relay mirrors affect only the outgoing wave.

## 2.2 OPTICAL COMPONENT MODELS

### 2.2.1 Tilt Mirror Model

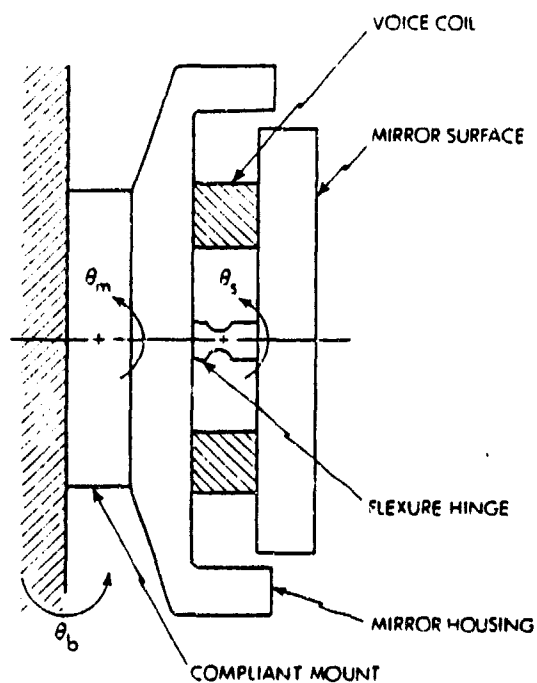
The tilt mirror model was based on component information from Ref. 3 and was structured to include the following effects:

- Mirror-flexure hinge dynamics
- Voice coil actuator dynamics
- Mount compliance dynamics
- Laser induced vibration.

Figure 2.2-1 depicts the physical model and includes a listing of the state variables, inputs, and disturbances used in the mathematical model.

The governing differential equations for the pitch-tilt dynamics are given by Eqs. 2.2-1 to 2.2-4. A listing of the relevant system parameters is shown in Table 2.2-1. The equation format and parameters for yaw tilt (i.e.,  $\psi_s$ ) are identical.

$$\dot{\underline{x}} = \underline{F}\underline{x} + \underline{g}\theta_{\text{cmd}} + \underline{h}\theta_b \quad (2.2-1)$$



MIRROR STATE VECTOR:

$$\underline{x}^T = \left( \theta_s, \dot{\theta}_s, \theta_m, \dot{\theta}_m, \frac{M_{ac}}{K_h} \right)$$

$\theta_s$  = MIRROR SURFACE ANGLE

$\theta_m$  = MOUNT COMPLIANCE ANGLE

$\left( \frac{M_{ac}}{K_h} \right)$  = NORMALIZED VOICE COIL TORQUE

INPUT:

$\theta_{CMD}$  = TILT CONTROL COMMAND

DISTURBANCES

$\theta_b$  = BASE MOTION DERIVED FROM VIBRATION MODEL

Figure 2.2-1 Tilt Mirror Mechanical Model and Variable Definition for Mirror Pitch Motion

TABLE 2.2-1  
TILT MIRROR MODEL PARAMETERS

T-1756

SYMBOL	DEFINITION
$\omega_h$	Surface-flexure hinge natural frequency
$\omega_m$	Mount natural frequency
$I'$	Mirror inertia/mount inertia
$\tau_1$	Voice coil time constant
$R_s$	Mirror Surface Radius

$$F = \begin{bmatrix} 0 & 1 & 0 & 0 & 0 \\ -\omega_h^2 & 0 & \omega_h^2 & 0 & \omega_h^2 \\ 0 & 0 & 0 & 1 & 0 \\ \omega_h^2 I' & 0 & -(\omega_h^2 I' + \omega_m^2) & 0 & -\omega_h^2 I' \\ 0 & 0 & 0 & 0 & -\frac{1}{\tau_1} \end{bmatrix} \quad (2.2-2)$$

$$\underline{g}^T = (0, 0, 0, 0, 1/\tau_1) \quad (2.2-3)$$

$$\underline{h}^T = (0, 0, 0, \omega_m^2, 0) \quad (2.2-4)$$

$$\Delta a_3 = (\Delta c_1, \Delta c_2, 0, 0, 0) \quad (2.2-5)$$

$$\Delta c_1 = 2\theta_s R_s \quad (2.2-6)$$

$$\Delta c_2 = \psi_s R_s \quad (2.2-7)$$

Where  $\theta_s$ ,  $\psi_s$ , and  $R_s$  are the elevation angle, azimuth angle, and beam radius of the mirror surface.

### 2.2.2 Focus Mirror Model

The focus mirror model represents the dynamics of a Cassegrain beam expander with a movable secondary mirror. The mathematical model was structured as the translational motion analog of the tilt mirror model, i.e., the following effects are considered:

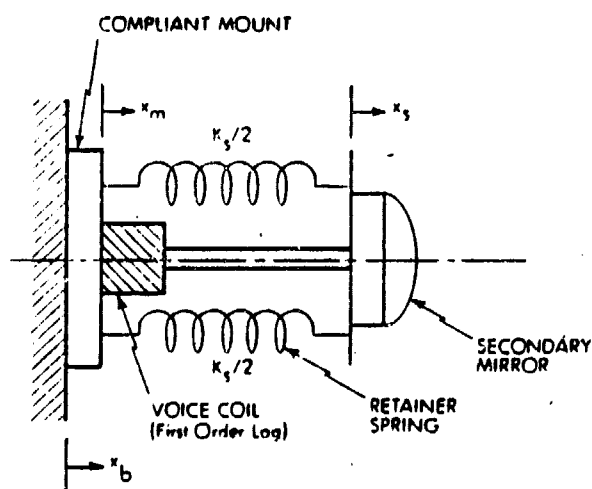
- Mirror-suspension spring dynamics
- Voice coil actuator dynamics
- Mount compliance dynamics
- Laser induced vibration.

Figure 2.2-2 shows the mechanical model of the moveable secondary mirror and includes a listing of the variables used in the mathematical model.

The governing state-space equations for the focus mirror dynamics are given by Eqs. 2.2-8 to 2.2-12. Model parameters are listed in Table 2.2-2.

$$\dot{\underline{x}} = \underline{F}\underline{x} + \underline{g}u + \underline{h}x_b \quad (2.2-8)$$

$$\Delta c_3 = .5x_s \left( \frac{R_p}{f_p} \right)^2 \quad (2.2-9)$$



MIRROR STATE VECTOR:

$$\underline{x}^T = \left( x_s, \dot{x}_s, x_m, \dot{x}_m, \frac{F_{ac}}{k_s} \right)$$

$x_s$  = MIRROR SURFACE DISPLACEMENT

$x_m$  = MOUNT COMPLIANCE DISPLACEMENT

$\left( \frac{F_{ac}}{k_s} \right)$  = NORMALIZED VOICE COIL FORCE

INPUT:

$u$  = FOCUS CONTROL COMMAND

DISTURBANCES

$x_b$  = BASE MOTION DERIVED FROM VIBRATION MODEL.

Figure 2.2-2 Focus Mirror Mechanical Model

TABLE 2.2-2  
FOCUS MIRROR MODEL PARAMETERS

T-1757

SYMBOL	DEFINITION
$\omega_s$	Movable mass-spring natural frequency
$\omega_m$	Mount natural frequency
$m'$	Mirror inertia/mount inertia
$\tau$	Voice coil time constant
$d_{\max}$	Maximum mirror displacement $\geq  x_s $
$f_p$	Primary mirror focal length
$R_p$	Primary mirror radius
$\Delta c_3$	Zernike focus coefficient

$$F = \begin{bmatrix} 0 & 1 & 0 & 0 & 0 \\ -\omega_s^2 & 0 & \omega_s^2 & 0 & \omega_s^2 \\ 0 & 0 & 0 & 1 & 0 \\ \omega_s^2 m' & 0 & -(\omega_s^2 m' + \omega_m^2) & 0 & -\omega_s^2 m' \\ 0 & 0 & 0 & 0 & -\frac{1}{\tau} \end{bmatrix} \quad (2.2-10)$$

$$\underline{g}^T = (0, 0, 0, 0, 1/\tau) \quad (2.2-11)$$

$$\underline{h}^T = (0, 0, 0, \omega_m^2, 0) \quad (2.2-12)$$

### 2.2.3 Deformable Mirror Model

The deformable mirror model was structured to include the predominant effects of mirror structural resonances and spring rate nonlinearities. Generality has been maintained in the model in that variations in structural resonant frequency, damping, and cross-coupling among the optical modes implemented on the deformable mirror can be conveniently effected. The deformable mirror model was structured according to the following assumptions:

- The mirror will be used to implement the optical modes listed in Table 2.1-1
- Dynamics of each optical mode are second order with linear coupling to the remaining modes
- Provisions are made for mirror nonlinear surface spring rate
- Piezoelectric actuator response is instantaneous.

The first two assumptions imply that the zonal dynamics of the mirror are dominated by the actuator structural dynamics and are essentially invariant over the surface of the mirror. Linear coupling between modes implies a variation of the DC gain of the zonal dynamics with respect to actuator applied force over the surface of the mirror; i.e.:

$$\frac{\Delta Z(x_o, y_o, s)}{f_{ac}(s)} = K(x_o, y_o)G(s) \quad (2.2-13)$$

Here  $\Delta Z$  and  $f_{ac}$  are the surface displacement and actuator force, respectively, at actuator position  $(x_o, y_o)$ .  $G(s)$  is a unity DC gain transfer function which is independent of actuator position.  $K(x_o, y_o)$  is an influence function which depends on actuator location.

Allowance for nonlinearity of the mirror surface spring rate characteristic is based on experience with the United Technologies deformable mirror, as described in Ref. 4. The restoring force of the mirror surface will be modeled as a quadratic function of mirror position with adjustable linear and quadratic term coefficients. Approximation of the piezoelectric actuator response by a unity gain is a simplifying assumption which should be acceptable for the anticipated range of dither frequencies. Actuator hysteresis effects have not been included.

The mathematical model which embodies these assumptions is as follows:

$$\dot{\underline{z}} = F(\underline{z})\underline{z} + B\underline{u} \quad (2.2-14)$$

$\underline{z}$  = Vector of mode strength and time derivative of each mode

$\underline{u}$  = Vector of mode commands

For the  $k^{\text{th}}$  mode:

$$\dot{z}_{2k-1} = z_{2k} \quad (2.2-15)$$

$$\dot{z}_{2k} = \underbrace{\left[ \omega_k(z_{2k-1}) \right]^2 z_{2k-1} - d_k z_{2k}}_{\text{Primary Dynamics}} + \underbrace{\sum_{j \neq 2k-1, 2k}^n c_{kj} z_j}_{\text{Coupling}} + \underbrace{\left[ \omega_k(z_{2k-1}) \right]^2 u_k}_{\text{Excitation}} \quad (2.2-16)$$

$$\left[ \omega_k(z_{2k-1}) \right]^2 = \omega_{k_0}^2 + (\omega_k^*) |z_{2k-1}| \quad (2.2-17)$$

$\omega_{k0}^2$  = Zero surface displacement natural frequency squared

$\omega_k^*$  = Nonlinearity constant (related to quadratic surface spring rate characteristic)

#### 2.2.4 Laser Phasefront Model

In the AMD and PC system simulations it is assumed that the HEL output is processed by a beam cleanup system that produces a uniform phasefront. The phasefront disturbance models used in the beam cleanup are described in Section 6.3.

#### 2.2.5 Thermal Distortion Model

The thermal distortion model is based on the results for cooled mirrors given in Ref. 5. Two sources of mirror deformation are considered:

- Thermal expansion effects (mirror surface thickness change)
- Mirror surface sag.

The first is characterized as a mapping of the incident intensity function and depends on nominal mirror dimensions, material properties, beam incidence angle, and elapsed time. The second effect is a function of the average incident intensity, beam incidence angle, and mirror geometric and material properties.

The relationship for the phasefront distortion due to thermal expansion is (Ref. 5):

$$\phi_1(x,y) = \frac{4\pi}{\lambda} a \xi_1 I(x,y) \cos^2 \theta_1 (1 - \exp(-t/\tau_{\text{thermal}})) \quad (2.2-18)$$



The corresponding equation for surface sag is:

$$\phi_2(x,y) = \frac{2\pi}{\lambda} 2aI_{ave} \left[ \left( \frac{r}{d} \right)^2 - \frac{1}{3} \right] \xi_2 \tan \theta_1 \sin \theta_1 (1 - \exp(-t/\tau_{thermal}))$$

(2.2-19)

where:

- $I(x,y)$  = Incident beam intensity
- $I_{ave}$  = Average beam intensity
- $a$  = Surface absorption coefficient
- $r$  = Radius from center of beam
- $d$  = Beam Diameter
- $\theta_1$  = Beam incidence angle
- $\lambda$  = Radiation wavelength
- $t$  = Elapsed time
- $\tau_{thermal}$  = Mirror thermal time constant
- $\xi_1, \xi_2$  = Mirror property dependent factors determined from empirical relationships in Ref. 2.

Here an exponential rise approximation has been made to the more complicated time dependence for  $\phi_1$  presented in Ref. 5; the same time dependence factor was assumed for the mirror sag response.

Both Eq. 2.2-18 and 2.2-19 implicitly include the effects of intensity spread due to beam incidence angle. For beam incidence angles other than  $90^\circ$ , the incident intensity profile on a mirror is the geometric projection of a rotationally symmetric Gaussian function onto the plane of the mirror surface. The mirror surface distortions produced by this nonsymmetric intensity distribution result

in optical path differences which produce the Gaussian and focus phasefront aberrations shown by Eq. 2.2-18 and 2.2-19, respectively.

The thermally induced aberrations of the following optical elements were assumed to add coherently (Ref. 6):

- Deformable mirror
- Tilt mirror
- Relay mirrors (4)
- Beam expander primary and secondary mirrors.

The combined effects of thermal expansion and mirror sag can be decomposed into a focus mode aberration plus a residual rms phasefront term. These two components are separately summed over the set of optical elements as:

$$\Delta a = \sum_{i=1}^8 (\Delta a_i)_{ss} \{1 - \exp(-t/\tau_{\text{thermal}_i})\} \quad (2.2-20)$$

$$\Delta \phi_{\text{rms}} = \sum_{i=1}^8 (\Delta \phi_i)_{ss} \{1 - \exp(-t/\tau_{\text{thermal}_i})\} \quad (2.2-21)$$

where:

$\Delta a_i$  = Focus mode strength of  $i^{\text{th}}$  component due to thermal distortion

$\Delta \phi_i$  = Residual phasefront error of  $i^{\text{th}}$  component due to thermal distortion

ss = Subscript indicating steady state

#### 2.2.6 Laser-Induced Vibration Model

A representative frequency spectrum for laser-induced vibration was taken from Ref. 7. As Fig. 2.2-3 shows, most

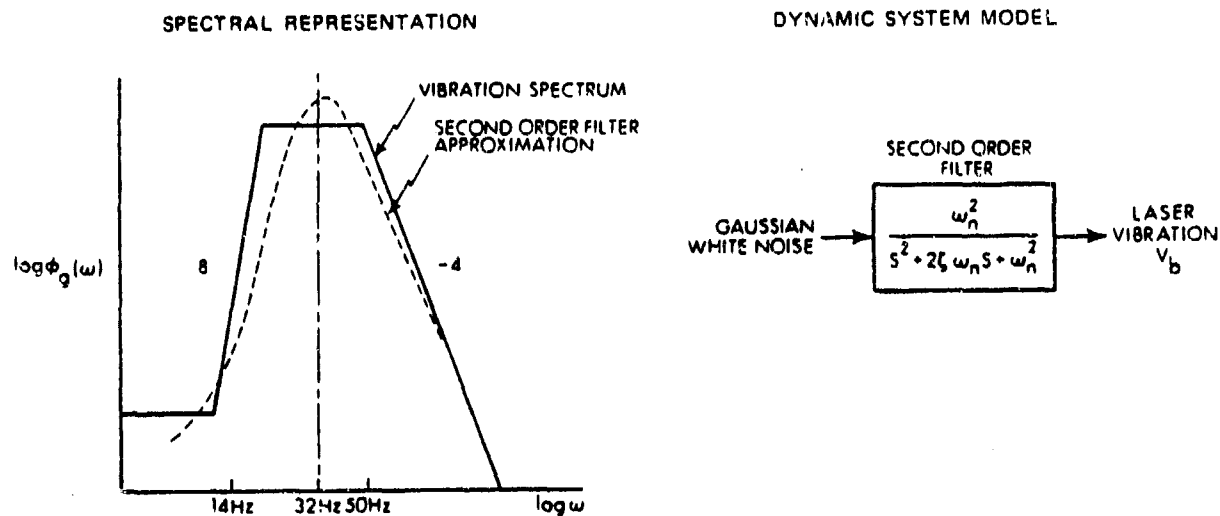


Figure 2.2-3 Laser Induced Vibration Spectrum and Model Approximation

of the spectral energy is located in a band between 14 and 50 Hz. This spectral shape suggests approximation by the output of an underdamped second order filter driven by white noise. The input noise variance and zero frequency gain of the filter are both set equal to unity; the vibration "input gains" of the affected optical components are adjusted to achieve a realistic level of component jitter.

### 2.2.7 Relay Mirror Jitter Model

Figure 2.2-4 shows the assumed relay mirror arrangement; Eqs. 2.2-22 to 2.2-24 define the related mathematical model. The pitch and yaw plane dynamics of each mirror are modeled as second order systems driven by the output of the laser vibration model. Due to the spatial and temporal distribution of the mounting structure response, the amplitudes and phases of the individual mirror responses will not be mounting structure dynamics, each mirror will be assigned a randomly chosen vibration input gain ( $k_i$ ) and a random time

ASSUMED RELAY MIRROR LAYOUT

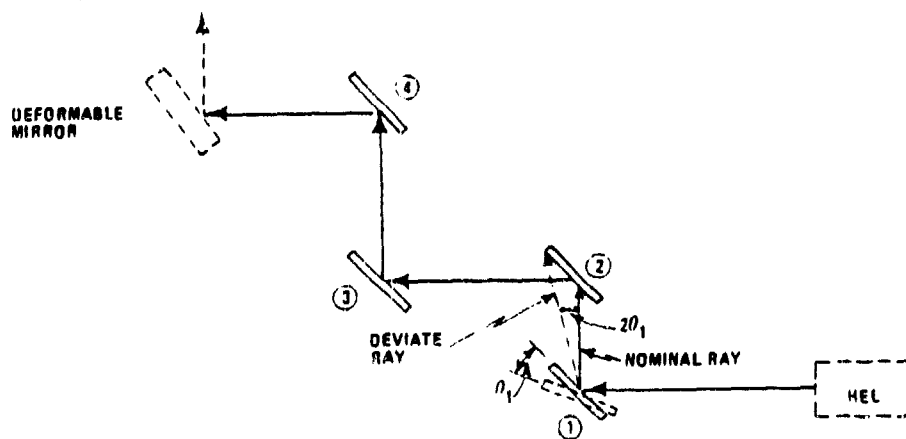


Figure 2.2-4 Assumed Relay Mirror Layout

shift of the laser vibration model output. Geometric analysis shows that a mirror displacement about the pitch axis (as indicated in the figure) results in a pitch tilt aberration of twice the displacement magnitude; displacements about the yaw axis generate an amount of yaw tilt equal to the displacement.

$$\text{Pitch tilt: } \theta_{\text{TOTAL}} = 2 \sum_{i=1}^4 \theta_i \quad (2.2-22)$$

$$\text{Yaw tilt: } \psi_{\text{TOTAL}} = \sum_{i=1}^4 \psi_i \quad (2.2-23)$$

$$\text{Total Dynamics: } \ddot{\theta}_i + 2\zeta_i \omega_{p_i} \dot{\theta}_i + \omega_{p_i}^2 \theta_i = k_i V_b(\tau_i) \quad (2.2-24)$$

$k_i$  = Vibration "input gain" of  $i^{\text{th}}$  mirror

$v_b$  = Vibration model output

$\tau_i$  = Random bias (simulates relative phase of mirror responses)

### 2.2.8 Sensor Models

Receiver Model (AMD only) - The receiver is represented by a fixed gain. The measurement of target return is corrupted by internal noise of the photomultiplier and by ambient radiation. Equation 2.2-25 is used to compute the measured return.

$$I_m = (I_t + N_a)K_{pmt} + N_{pmt} \quad (2.2-25)$$

where:

- $I_m$  = Measured return
- $I_t$  = Speckle corrupted return
- $N_a$  = Ambient radiation level
- $K_{pmt}$  = Photomultiplier gain
- $N_{pmt}$  = Photomultiplier internal noise

Shearing Interferometer - Reference 8 provides an optical analysis and a thorough description of the operation of the shearing interferometer. The net result of the optical analysis of Ref. 8 is Eq. 2.2-26:

$$\underline{z} = H\underline{c} + \underline{\epsilon} \quad (2.2-26)$$

$\underline{z}$  is a 12 element vector of the electrical phases measured by the subapertures of the shearing interferometer. The columns of the H matrix represent the observation of a particular aberration mode  $c_j$ ; i.e.,  $H_{ij}$  is the electrical phase measured by subaperture  $i$  due to a unit value of aberration mode  $j$ . Off-line computation of  $H_{ij}$  is described in Ref. 8.  $\underline{c}$  is the vector of aberration mode strengths at the shearing interferometer due to atmospheric and thermal distortion effects:

$$\underline{c} = \underline{CS} + \underline{CA} \quad (2.2-27)$$

where  $\underline{CS}$ , and  $\underline{CA}$  are the shared aperture optical component and atmospheric aberration modes, respectively (see Fig. 2.1-2).  $\underline{n}$  is a vector of zero mean white noise processes; the variance of these measurement noise processes is inversely proportional to the signal-to-noise ratio at the shearing interferometer. The determination of this signal to noise ratio is described in Section 2.3.3.

## 2.3 ATMOSPHERIC PROPAGATION EFFECTS

### 2.3.1 Atmospheric Turbulence Models

Frequency spectra corresponding to the controlled optical mode shapes defined in Table 2.1-1 are generated using an AFWL-supplied program, Ref. 1. The spectrum for each mode is dynamically modeled as the output of a linear shaping filter driven by white noise. The computed turbulence spectrum and filter spectrum approximation for a tilt mode are shown in Fig. 2.3-1; Fig. 2.3-2 is the shaping filter realization. The output of the turbulence model is also delayed one transit-time-to-target (TTTT) before it is used in the target intensity computation.

### 2.3.2 Intensity at Target

The intensity distribution on the target plane is the squared magnitude of the Fraunhofer transform of the amplitude and phase distribution at the exit aperture. The amplitude distribution is assumed to be uniform over the aperture and the intensity distribution is computed as a function of the phase distribution characterized by Zernike coefficients.

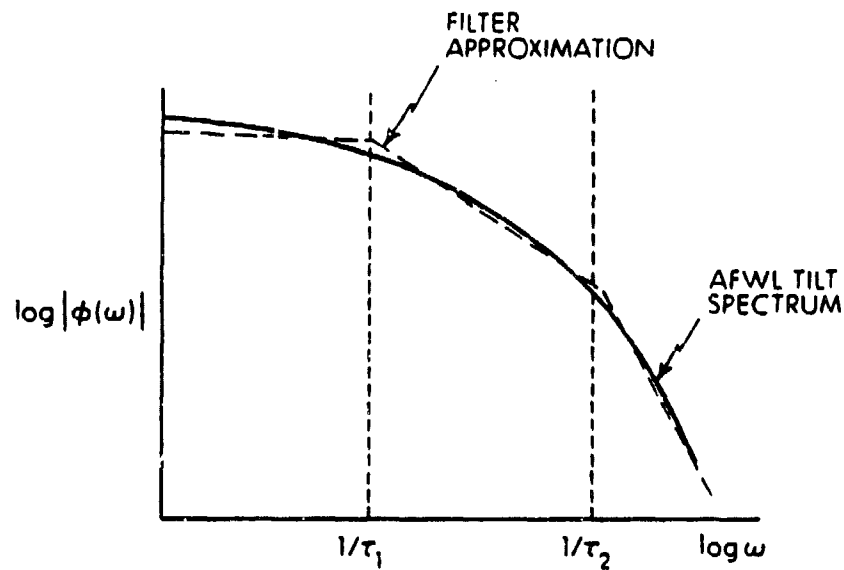
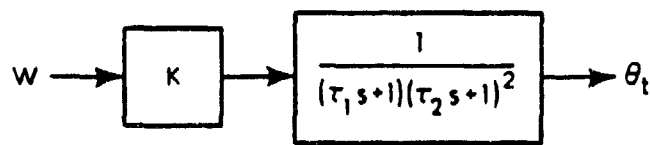


Figure 2.3-1 Turbulence Spectral Representation



$W$  = Unity variance white noise

$K$  : Adjusted to obtain desired rms level of tilt

Figure 2.3-2 Turbulence Dynamic Model

For computational simplicity, the exact distribution is approximated by a Gaussian function of the Zernike coefficients,  $g(\underline{c})$ , as given below.

$$g(\underline{c}) = \frac{\beta P_t}{2\pi\sigma^2} \left[ \exp -\frac{1}{3}(kc_3)^2 \right] \exp \left[ \frac{-\beta\rho^2}{2\sigma^2} \exp \left[ -\frac{1}{3}(kc_3)^2 \right] \right] \quad (2.3-1)$$

where:

$$k = \frac{2\pi}{\lambda} \quad (2.3-2)$$

$$\sigma = \frac{1}{\pi\sqrt{2}} \frac{\lambda Z}{R} \quad (2.3-3)$$

$$\rho = \frac{Z}{R} (c_1^2 + c_2^2)^{\frac{1}{2}} \quad (2.3-4)$$

$$\beta = 1 - \frac{1}{6}k^2 (c_4^2 + c_5^2) \quad (2.3-5)$$

and,

$P_t$  = Transmitted power

$\lambda$  = Laser wavelength

$Z$  = Distance to the target

$R$  = Radius of the aperture

### 2.3.3 Target Effects

In both the phase conjugate and active multidither systems, interactions of the incident laser beam with the target surface affect the optical feedback signal. In the phase conjugate model, the heating of the target surface affects its radiation level; for active multidither, target surface shape, roughness, and reflectivity variations corrupt the return wave with speckle. Mathematical models of target effects are described in this section.

Speckle Model (AMD only) - Speckle is represented as a normalized (unity mean) multiplicative noise which



modulates the target return intensity. In general, the spectral content of the speckle modulation is a complicated function of target surface properties and target motion. Two limiting cases, however, provide useful guidelines for the construction of a simple model. First, if the target surface is perfectly specular, the return intensity is unmodulated; hence, speckle could be regarded as a Gaussian random process of unity mean and zero variance. The other extreme is represented by a totally diffuse target. In this case, the net effect of speckle is modulation of the target return by a random process of unity mean and unity standard deviation. A reasonable structure for a dynamic model, which would represent a case between these two extremes, is a unity mean Gauss-Markov process having a standard deviation proportional to the diffusivity of the target surface.

The dynamic system realization of the simplified model structure is a unity-DC-gain shaping filter driven by white noise and a unity input as shown in Fig. 2.3-3. The appropriate frequency domain representation of the shaping

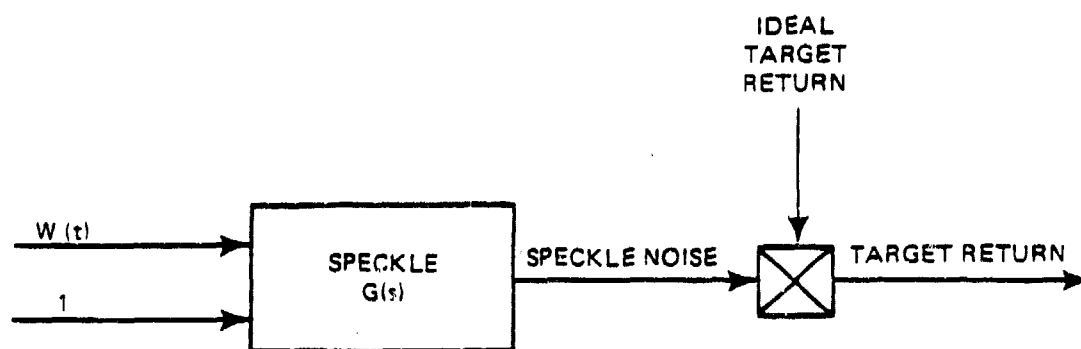


Figure 2.3-3 Speckle Dynamic Model

filter is determined from first order filter cascade approximations to speckle spectra supplied by General Research Corporation, Ref. 9. A cascade of three first order filters, each having a break frequency of 2300 Hz, yields a good approximation to that data (see Fig. 2.3-4). The input variance is adjusted to yield a standard deviation of 0.3.

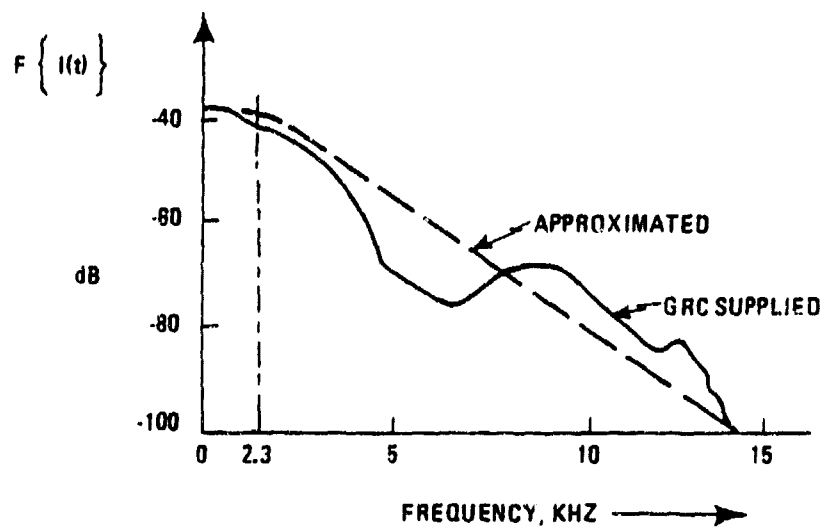


Figure 2.3-4 Speckle Filter Approximation

Target Radiation (PC only) - The passive radiation of a target is a complicated function of target shape, temperature (including heating effects of the incident laser beam), surface characteristics, and of the ambient radiation level. The mathematical analysis of target passive radiation is presented in Ref. 8; the net effect of all of the contributing influences is the signal level at the shearing interferometer. For the purposes of this study the target effects model will be for a rectangular target having a uniform radiation level; the shape and radiation level determine the signal to noise ratio of the shearing interferometer measurements.

3.

### MODE ESTIMATION IN ADAPTIVE OPTICS

#### 3.1 ACTIVE MULTIDITHER

Inaccuracies in the mode estimates for the AMD scheme are caused by measurement noise corrupting the detection of the reflected intensity from the target, as well as by the speckle effects due to reflections from a diffused target surface. The mode estimates can be improved by incorporating in the estimation algorithm statistical information available on the turbulence induced phase fluctuations, measurement noise, and time varying speckle patterns. Conventional (analog or digital) mode estimation algorithms do not use this a priori statistical information explicitly. A Kalman filter uses a priori statistical properties to arrive at the best estimate of the aberrated phasefront. In addition, the Kalman filter algorithm provides estimates of the full states of the disturbances. As described in the next section, optimal control of the adaptive optics components utilizes the full state of the disturbance process it attempts to counteract.

The received intensity is a function of the phasefront introduced by the turbulence existing two transit times in the past; one transit time each for propagation to and from the target. Processing (conventional or Kalman) of the received intensity only provides a two-transit-times delay estimate of the phasefront. Because of significant time delays encountered in long range applications, such estimates differs substantially from the present aberration, i.e., that to be compensated by the active optics elements. However, as the Kalman filter yields delayed estimates of the phasefront as well as its time derivatives, the output of the Kalman filter along with the statistical information on the phase

fluctuations provide a basis for predicting the present aberration from the delayed estimates.

In this report, extended (because of nonlinear measurements) Kalman filtering algorithms are developed to estimate the Zernike modes of the phasefront aberrated by atmospheric turbulence. First, filtering and prediction algorithms for an ideal point target are described. The modification to a Kalman filter made necessary by the time varying speckle pattern in the received intensity is discussed later.

The transfer functions derived for mode fluctuations discussed in Section 2.3.1, and the Gaussian intensity distribution at the target as a function of these modes (described in Section 2.3.2) form the basis of the Kalman filter formulation. From the pole/zero values representing the spectrum of each mode fluctuation due to atmospheric turbulence (Figs. 2.3-1 and 2.3-2), a continuous time state variable equation is formulated as,

$$\dot{\underline{CA}} = F \underline{CA} + GW \quad (3.1-1)$$

The state transition matrix,  $\phi$ , is then computed as

$$\phi(t) = e^{Ft} \quad (3.1-2)$$

For a sampling period,  $T$ , the discrete time Markov model for the mode fluctuations can now be written as

$$\underline{CA}_k = \phi(T)\underline{CA}_{k-1} + \underline{W}_{k-1} \quad (3.1-3)$$

where, the covariance,  $Q$ , of the discrete sequence,  $\underline{W}_k$ , is given by

$$Q = \int_0^T \phi(T-\tau) G Q_c G^T \phi^T(t-\tau) dt \quad (3.1-4)$$

where,

$$E[Gw(\tau) w^T(\tau) G^T] = Q_c \delta(t-\tau) \quad (3.1-5)$$

The mode strengths in the exit pupil phasefront being propagated to the target is the sum of the turbulence induced modes, CA, and the modes out of the adaptive optics components, CC. The measured intensity, I, is the Gaussian function (Eq. 2.3-1) of the exit pupil mode strengths two transit times in the past, corrupted with zero mean, white, Gaussian measurement noise, V. That is,

$$I_k = g(\underline{CA}_{k-\text{delay}} + \underline{CC}_{k-\text{delay}}) + V_k \quad (3.1-6)$$

where the delay equals twice the transit time. The same expression is being used for received intensity or for the intensity distribution at the target, since multiplying factors, e.g., target reflectivity, solid angle of collection, detector responsivity, etc., can be accounted for by choosing an appropriately scaled variance for the measurement noise,  $V_k$ . Equations 3.1-3 and 3.1-5 constitute the "truth" model portion in the evaluation of estimation algorithms for turbulence induced mode fluctuations in an AMD system.

In the Kalman filter formulation, the mode estimates are extrapolated between the sampling intervals by

$$\hat{\underline{CA}}_k(-) = \phi(T) \hat{\underline{CA}}_{k-1} \quad (3.1-7)$$

The residual error between the measured intensity and the expected intensity is given by

$$v_k = I_k - g(\hat{\underline{CA}}_{k-\text{delay}}(-) + \underline{CC}_{k-\text{delay}}) \quad (3.1-8)$$

The estimates are then updated by

$$\hat{CA}_{k\text{-delay}}^{(+)} = \hat{CA}_{k\text{-delay}}^{(-)} + \underline{K}_k v_k \quad (3.1-9)$$

where  $\underline{K}_k$  is the Kalman gain vector defined later. The estimates of the present aberration, which is to be compensated by the active optics component, is then predicted by,

$$\hat{CA}_k = \phi(\text{delay}) \hat{CA}_{k\text{-delay}}^{(+)} \quad (3.1-10)$$

where  $\phi(\text{delay})$  is the state transition matrix corresponding to the turbulence statistics over the length of the delay, i.e., Eq. 3.1-2 recalculated with the argument equalling twice the transit time. Comparing Eqs. 3.1-6 and 3.1-9, it is observed that the optimal prediction is simply optimal filtering in the absence of measurements.

Computation of the Kalman gains requires a measure of estimation error covariance,

$$P_k = E \left\{ (\underline{CA}_k - \hat{CA}_k)(\underline{CA}_k - \hat{CA}_k)^T \right\} \quad (3.1-11)$$

The covariance is extrapolated between the intervals by

$$P_k(-) = \phi(T) P_{k-1}(+) \phi^T(T) + Q \quad (3.1-12)$$

where  $\phi(T)$  and  $Q$  are given by Eq. 3.1-2 and Eq. 3.1-4, respectively. The Kalman gains are computed as

$$\underline{K}_{k+\text{delay}} = P_k(-) H_k^T \left[ H_k P_k(-) H_k^T + R \right]^{-1} \quad (3.1-13)$$

where  $R$  is the covariance of the measurement noise,  $V$ , and the elements of  $H_k$  are given by

$$H_{k,i} = \frac{\partial g}{\partial CA_{k,i}} \bigg|_{CA = \hat{CA}_k(-)} \quad (3.1-14)$$

The error covariance matrix is updated by

$$P_k(+)=\left[I-K_{k+\text{delay}}H_k\right]P_k(-)\quad(3.1-15)$$

The necessity of dithering the modes for estimating them is well understood in a conventional AMD scheme. The dither waveforms provide carriers for the fluctuating mode strengths which are recovered by demodulation. It is of interest to the system engineer to reformulate the problem and substantiate the requirement of dithers for observability of the states from the measurements. Computing the observation matrix,  $H_k$ , for constant mode strengths, it can be shown that the pair  $(\phi, H_k)$  results in an unobservable system without dither signals. This is to be expected, as only the squares of the states enter the measurement equation. Introducing dither signals cause the observation matrix to be time varying even for constant state values, and thus provide observability.

From an engineering standpoint, it is desirable to keep the dither frequency as low as possible while providing a sufficient data rate for compensation of aberration. In the digital implementation, new information enters the system for reestimation of the mode strengths only when a dither signal changes sign. As all the modes are coupled through the observation equation, dithering of a single mode provides information on all the modes. A time multiplexed dither sequence is chosen to provide a high data rate while maintaining a low dither frequency for individual modes, i.e., the modes are dithered, one at a time, in a specified sequence while all the modes are estimated when any of the modes is dithered.

The effect of time varying speckle pattern in the received intensity is discussed in Section 2.3.3. As in the case of turbulence modeling, a discrete-time state variable model

is derived to correspond to the speckle spectrum of Fig. 2.3-4. In the truth model of the simulation, the point target return in Eq. 3.1-5 is multiplied by the output of the speckle model,  $q_k$ , so that the received intensity becomes

$$I_k = (1 + q_k)g(\underline{CA}_{k\text{-delay}} + \underline{CC}_{k\text{-delay}}) + V_k \quad (3.1-16)$$

A filter design can be constructed which estimates the output of the speckle model and thereby recovers the ideal point return from the received intensity. However, any such design will assume a knowledge of the true speckle model, in addition to requiring a very high data rate. For a target dependent phenomenon, availability of such specific information is questionable. In our modification to the extended Kalman filter to account for the speckle effects, only a knowledge of the rms value of the temporal fluctuations caused by speckle (and that it is a broadband effect) is assumed.

To accomplish the aforementioned modification, Eq. 3.1-15 is first rewritten as

$$I_k = g(\underline{CA}_{k\text{-delay}} + \underline{CC}_{k\text{-delay}}) + q_k g(\underline{CA}_{k\text{-delay}} + \underline{CC}_{k\text{-delay}}) + V_k \quad (3.1-17)$$

Note that the first term is the ideal point return, and that the second term is broadband. In the modified extended Kalman filter, the second term is lumped with the detector noise,  $V$ , and the combined variance,  $R_t$ , is given by

$$R_t \approx \sigma_q^2 g(\underline{C})|_{\underline{C} = \underline{CD}} + R \quad (3.1-18)$$

where  $\underline{CD}$  is the vector of dither amplitudes, and it is implicitly assumed that the system is performing near its optimum, i.e., the deflection from the aimpoint is solely due to dither.



The Kalman gains in the modified extended Kalman filter are computed with  $R_t$  replacing  $R$  in Eq. 3.1-12. By appropriately increasing the effective measurement noise variance in the computation of Kalman gains, the effect of speckle is diluted and, consequently, a reduced emphasis is placed on the measurements.

### 3.2 PHASE CONJUGATE

In the PC scheme, inaccuracies in the mode estimates are caused by measurement noise corrupting the sensing of the phasefront of the passive target radiation. As in the AMD scheme, the mode estimates can be improved by incorporating in the estimation algorithm, statistical information available on the turbulence induced phase fluctuations and the measurement noise. The least square fit algorithm described in Section 3.2.1 does not use such a priori statistical information; a least square fit followed by a low pass filter (discussed in Section 3.2.2) makes a partial use of the available information. However, the Kalman filtering algorithm uses all available inputs in an optimal manner to arrive at the best estimate of the aberrated phasefront. Also, the Kalman filter provides the full state vector of the phasefront aberrations required for the optimal control of the active optics components. It should be noted that the phase measurement in the PC scheme correspond to the present aberration (because it corresponds to the return wavefront through the turbulence at or near the aperture), which is unlike the intensity measurement in the AMD scheme which corresponds to the delayed aberration.

The discrete time Gauss-Markov model to simulate the turbulence induced mode fluctuations is given by Eq. 3.1-3, repeated below:

$$\underline{CA}_k = \phi(T)\underline{CA}_{k-1} + \underline{W}_{k-1} \quad (3.2-1)$$

The mode strengths,  $\underline{CE}$ , in the exit pupil phasefront propagated to the target are the sum of the turbulence induced modes,  $\underline{CA}$ , the modes from the elements shared by the outgoing and incoming path,  $\underline{CS}$ , and modes not sensed by the shearing interferometer,  $\underline{CL}$ . The modes sensed by the shearing interferometer are the sum of  $\underline{CA}$  and  $\underline{CS}$ , and as detailed in Ref. 8 the electrical phase measurements,  $\underline{Z}$ , out of the shearing interferometer are given by

$$\underline{Z}_k = H(\underline{CS} + \underline{CA})_k + V_k \quad (3.2-2)$$

Equations 3.2-1 and 3.2-2 constitute the truth model portion in the evaluation of estimation algorithms for turbulence induced mode fluctuations in a PC system.

### 3.2.1 Least Square Fit

In this method, the dynamics of the modes to be estimated and the spectral properties of the measurement noise are ignored. For least square estimation error, the estimate of the net aberration is given by

$$\widehat{(\underline{CS} + \underline{CA})}_k = (H^T H)^{-1} H^T \underline{Z}_k \quad (3.2-3)$$

As the name implies, this estimate of the net aberration achieves the least square fit to the observed data.

### 3.2.2 Least Square Fit Followed By Low Pass Filter

In this method, the exact dynamics of the modes to be estimated are not considered; however, a spectral separation of the modes and the process noise is attempted. The mode estimates are given by:

$$(\underline{CS} + \underline{CA})_k = a(\underline{CS} + \underline{CA})_{k-1} + (1-a)U_k \quad (3.2-4)$$

where  $U_k$  is the least square fit estimate provided by Eq. 3.2-3. The value of 'a' is between zero and unity, and is determined from the desired bandwidth of the low pass filter.

### 3.2.3 Kalman Filter

The Kalman filtering algorithm optimally uses both the modal dynamics and the measurement noise statistics. The filtering equations are essentially a repetition of Eq. 3.1-6 through Eq. 3.1-8, written for the AMD scheme. The mode estimates are extrapolated between the sampling intervals by

$$\hat{\underline{CA}}_k(-) = \phi(T)\hat{\underline{CA}}_{k-1} \quad (3.2-5)$$

The residual errors between the measured phases and the expected phases is given by

$$v_k = z_k - H[\hat{\underline{CA}}_k(-) + \underline{CS}_k] \quad (3.2-6)$$

The estimates are then updated by

$$\underline{CA}_k(+) = \underline{CA}_k(-) + K_k v_k \quad (3.2-7)$$

where  $K_k$  is the Kalman gain vector. For computing the Kalman gains, the covariance of the estimation error (Eq. 3.1-10) is extrapolated between the intervals by

$$P_k(-) = \phi(T)P_{k-1}(+) \phi^T(T) + Q \quad (3.2-8)$$

where  $\phi(T)$  and  $Q$  are given by Eq. 3.1-2 and Eq. 3.1-4, respectively. The Kalman gains are computed as

$$\underline{K}_k = P_k(-)H^T [HP_k(-)H^T + R]^{-1} \quad (3.2-9)$$

where,  $R$  is the covariance of the measurement noise,  $V$ . The error covariance matrix is updated by

$$P_k(x) = [I - K_k H] P_k(-) \quad (3.2-10)$$

In an actual implementation of the Kalman filter, the covariance,  $R$ , of the measurement noise,  $V$ , is not accurately known in computing the Kalman gains (Eq. 3.2-9). The heating of the target after the laser is turned on increases the signal-to-noise ratio at the shearing interferometer output. An algorithm is described to change the value of  $R$  to adapt for a change in the signal-to-noise ratio.

The residual error,  $v_k$ , after the extrapolation (Eq. 3.2-5) is a Gaussian random variable with covariance,  $S_k$ , given by

$$S_k = H P_k(-) H^T + R_t \quad (3.2-11)$$

where  $R_t$  is the true covariance of the measurement noise. A scalar variable,  $b$ , is defined as

$$b_k = \frac{v_k^T}{v_k} [H P_k(-) H^T + R]^{-1} v_k \quad (3.2-12)$$

where  $R$  is the assumed covariance of the measurement noise used in the Kalman gain computations. The expected value of  $b_k$  provides a measure of the mismatch between the true and the assumed values of the measurement noise:

$$E(b_k) = \begin{cases} < 1 & R > R_t \\ = 1 & \text{for } R = R_t \\ > 1 & R < R_t \end{cases} \quad (3.2-13)$$

An adaptive filtering algorithm to change the value of  $R$  to

be used in the Kalman gain computations is therefore formulated as

$$\begin{aligned} R_{k+1} &= R_k - \Delta R & \text{if } b_k < \epsilon_1 \\ R_{k+1} &= R_k & \text{if } \epsilon_1 < b_k < \epsilon_2 \\ R_{k+1} &= R_k + \Delta R & \text{if } b_k > \epsilon_2 \end{aligned} \quad (3.2-14)$$

### 3.3 EVALUATION OF THE ESTIMATION ALGORITHMS

#### 3.3.1 Active Multidither

The Kalman filtering algorithms for the AMD system is evaluated for two ranges, 100 Km and 500 Km. To isolate the effects of the transit delay, the same signal-to-noise ratio of 20 is assumed for both the ranges. The aperture radius is assumed to be 1 m, and the turbulence parameters are listed in Table 3.3-1.

To evaluate the effects of the data rate, the system is simulated at two dither frequencies, 250 Hz and 500 Hz. The filtering algorithm for an ideal point target is described by Eq. 3.1-6 to Eq. 3.1-14; the results of the simulation are listed in Table 3.3-2. The Strehl ratio without the dither loss is intensity computed with estimation error only. In all cases, very significant improvements in the Strehl ratio are achieved over that with no estimation and control.

The modifications in the filtering algorithm due to the speckle effects are described in Eq. 3.1-15 to Eq. 3.1-17. The results of the simulation for a speckle standard deviation of 0.3 and a triple corner frequency of 2.3 kHz, are listed in Table 3.3-3. Although there is a degradation in the Strehl ratio compared to the corresponding point target case, there is still a substantial improvement over that with no estimation and control.

TABLE 3.3-1  
TURBULENCE PARAMETERS (AMD)

T-1904

ZERNIKE MODES	FIRST CORNER FREQUENCY (Hz)	ROOT MEAN SQUARE ( $\mu\text{m}$ )
1. $r \cos \theta$ , TILT	2.25	1.2
2. $r \sin \theta$ , TILT	2.25	1.2
3. $2(r^2 - 1)$ . DEFOCUS	4.5	0.23
4. $r^2 \sin 2\theta$ , ASTIGMATISM	2.0	0.33
5. $r^2 \cos 2\theta$ , ASTIGMATISM	3.5	0.33

TABLE 3.3-2  
AMD WITH POINT TARGET

T-1905

RANGE (Km)	STREHL RATIO				
	WITHOUT ESTIMATION AND CONTROL	WITH ESTIMATION AND IDEAL CONTROL			
		WITH DITHER LOSS		WITHOUT DITHER LOSS	
		250 Hz	500 Hz	250 Hz	500 Hz
100	.315	.698	.730	.887	.966
500	.315	.687	.736	.807	.875

TABLE 3.3-3  
AMD WITH SPECKLE RETURN

T-1906

RANGE (Km)	STREHL RATIO				
	WITHOUT ESTIMATION AND CONTROL	WITH ESTIMATION AND IDEAL CONTROL			
		WITH DITHER LOSS		WITHOUT DITHER LOSS	
		250 Hz	500 Hz	250 Hz	500 Hz
100	.315	.668	.690	.814	.838
500	.315	.600	.550	.689	.636

### 3.3.2 Phase Conjugate

The filtering algorithms for the PC system are evaluated for a range of 5 Km. The aperture radius is assumed to be 0.25 m; the turbulence parameters are listed in Table 3.3-4.

TABLE 3.3-4  
TURBULENCE PARAMETERS (PC)

ZERNIKE MODES	FIRST CORNER FREQUENCY (Hz)	ROOT MEAN SQUARE ( $\mu\text{m}$ )
1. $r \cos \theta$ , TILT	7.5	1.1
2. $r \sin \theta$ , TILT	7.5	1.1
3. $2(r^2 - 1)$ , DEFOCUS	15.0	0.21
4. $r^2 \sin 2\theta$ , ASTIGMATISM	6.7	0.3
5. $r^2 \cos 2\theta$ , ASTIGMATISM	11.6	0.3

The shearing distances are 0.017 m in the X direction, and 0.057 m in the Y direction. The system is simulated for three rms levels of electrical phase measurement noise at the output of the shearing interferometer, 0.1 rad, 0.2 rad and 0.3 rad. The results of the simulations plotted in Fig. 3.3-1 are all for a data rate of 1 kHz.

As the LSF makes no attempt to filter the measurement noise, at a high noise level the performance of LSF is actually worse than attempting no corrections. If the bandwidth of the LPF is too narrow relative to turbulence bandwidth, and the noise level is very low, the performance of LSF-LPF is seen to be worse than simple LSF, because the LPF is filtering out the true signal. As expected the performance of the Kalman filter is superior at all noise levels.

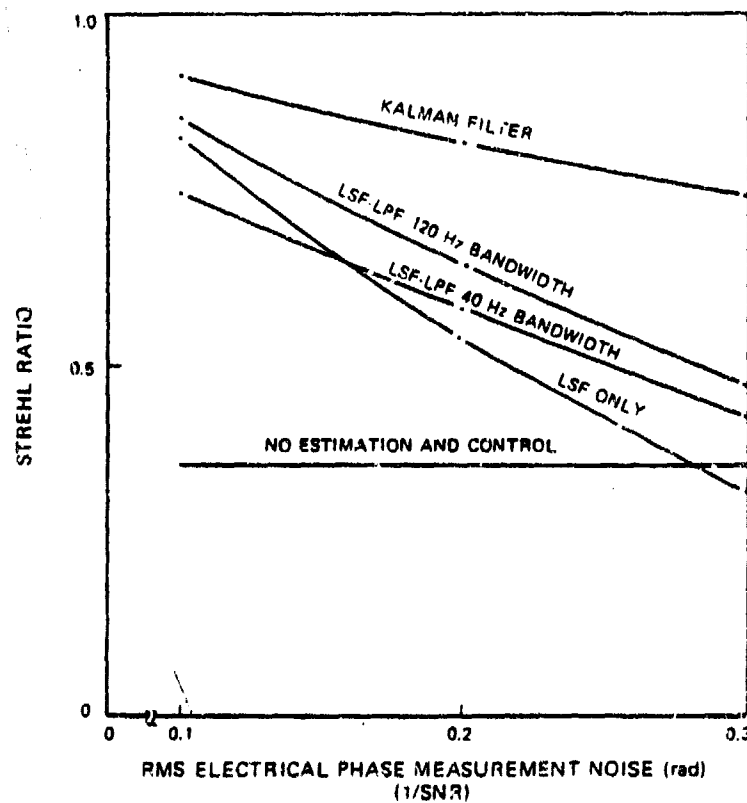


Figure 3.3-1 Phase Conjugate



4.

## OPTIMAL CONTROL IN ADAPTIVE OPTICS

### 4.1 INTRODUCTION

The goal of an adaptive optics control system is to continuously null disturbances arising from such effects as turbulence, vibration, and thermal distortion. Ideally, an active optics component such as a focus system would counteract perfectly the focus disturbances of the system environment. Practically, such realities as finite response time and structural mode excitation preclude the possibility of perfect disturbance nulling. Modern control theory recognizes the non-ideal characteristics of active components and offers a realistic yet ambitious approach; the goal of an optimal controller is to minimize the difference between a disturbance state that degrades system performance and the active element response that attempts to counteract it.

This chapter will deal with the application of optimal control, distinct from the estimation problem, in adaptive optics. Section 4.2 outlines the formulation of the optimal disturbance nulling control problem; quadratic performance indices used in the A/O control synthesis are derived in Section 4.3. The inner control loops used to extend the control bandwidths of the tilt and focus optics are described in Section 4.4. Application of optimal disturbance nulling control to the deformable mirror required an unusual approach which is summarized in Section 4.5. Some preliminary results which demonstrate the advantages of the modern control approach over candidate classical designs are provided in Section 4.6; additional control performance results are presented for the integrated estimation-control system in Section 5.

## 4.2 OPTIMAL DISTURBANCE NULLING CONTROL

The general structure of an optimal disturbance nulling control system is shown in Fig. 4.2-1. The system consists of a linear dynamic model of the disturbance to be nulled, a matrix of feedforward gains which operates on the disturbance states to compute the control  $\underline{u}_1$ , and an active element having a feedback controller. In an adaptive optics system the disturbance model might represent the dynamics of a turbulence-induced aberration while the controllable element would be an active component such as a tile mirror. Here, ideal estimation has been assumed in accordance with the Separation Theorem (Section 1.2); all of the disturbance model states are available to the feedforward controller.

The optimal structure shown in Fig. 4.2-1 utilizes all available knowledge of the dynamics of both the disturbance model and the controllable element, as well as all current information on the disturbance state in computing the controls  $\underline{u}_1$  and  $\underline{u}$ . More specifically, the state vector

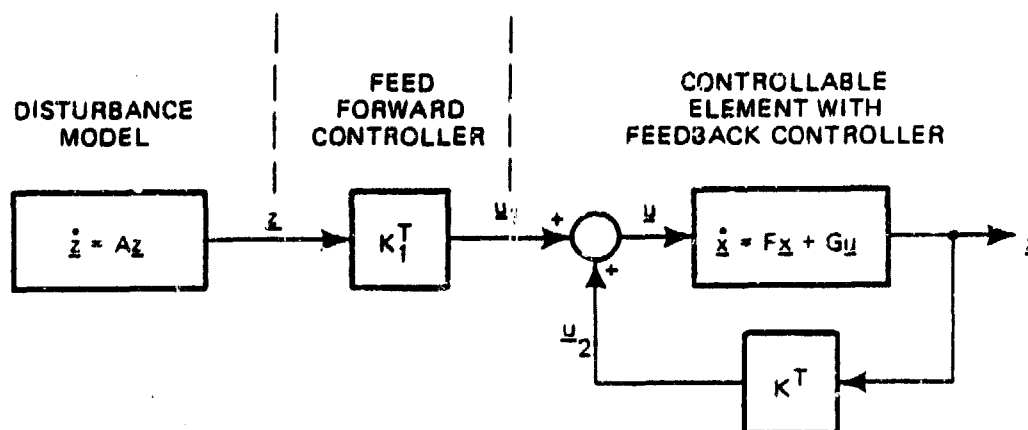


Figure 4.2-1 Disturbance Nulling Control Structure

of the disturbance model provides the present value of the disturbance plus states related to the time derivatives of the disturbance. Using the full state of the disturbance, the control  $u_1$  can be computed not only to counteract the present value of the disturbance but also to anticipate (in part) the future of the process through the derivative states. It will be shown in Section 4.6 that this anticipation effect can lead to a significant alleviation of sample rate and controllable element bandwidth requirements.

The formulation and solution of the mathematical problem to determine  $K$  and  $K_1$  can be facilitated by re-drawing the structure of Fig. 4.2-1 into an optimal regulator format, as shown in Fig. 4.2-2. The augmented plant consists of the dynamics of the controllable element and of the

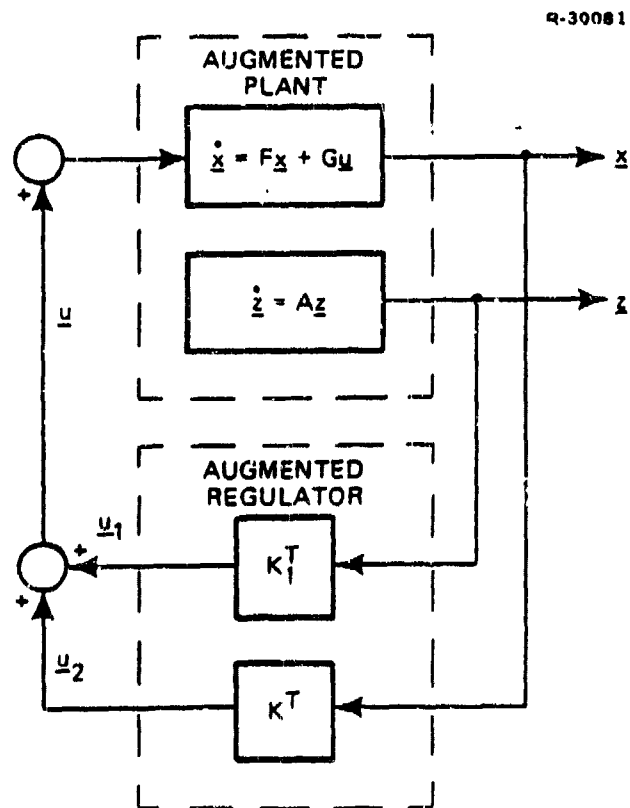


Figure 4.2-2 Equivalent Optimal Regulator Structure

disturbance; the augmented regulator includes both the feed forward and feedback controllers. The optimal regulator problem then specifies that the control gains are:

$$\hat{K}^T = R^{-1} \hat{G}^T \hat{P} \quad (4.2-1)$$

where:

$$\hat{K}^T = (K^T | K_1^T)$$

$R^{-1}$  = Inverse of control weighting matrix

$\hat{G}$  = Control effectiveness of augmented system

$\hat{P}$  = Solution of Ricatti Equation for the augmented system

Following Ref. 2, the mathematical description of the augmented system is given by Eqs. 4.2-2 to 4.2-4.

$$\hat{\underline{x}}^T = (\underline{x}^T | \underline{z}^T) \quad (4.2-2)$$

$$\hat{G}^T = (G | 0) \quad (4.2-3)$$

$$\hat{F} = \begin{bmatrix} F & | & 0 \\ \hline 0 & | & A \end{bmatrix} \quad (4.2-4)$$

with the performance index:

$$J = \int_0^{\infty} \{ \underline{u}^T R \underline{u} + (\underline{y} + \tilde{\underline{y}})^T Q (\underline{y} + \tilde{\underline{y}}) \} dt \quad (4.2-5)$$

$$= \int_0^{\infty} \{ \underline{u}^T R \underline{u} + (H^T \underline{x} + C^T \underline{z})^T Q (H^T \underline{x} + C^T \underline{z}) \} dt \quad (4.2-6)$$

$$= \int_0^{\infty} \{ \underline{u}^T R \underline{u} + \hat{\underline{x}}^T \hat{Q} \hat{\underline{x}} \} dt \quad (4.2-7)$$

where:

$$Q = \left[ \begin{array}{c|c} \hline Q & QH(H^TH)^{-1}C^T \\ \hline (QH(H^TH)^{-1}C^T)^T & C(H^TH)^{-1}H^TQH(H^TH)^{-1}C^T \\ \hline \end{array} \right] \quad (4.2-8)$$

$$= \left[ \begin{array}{c|c} \hline Q & Q_{21}^T \\ \hline Q_{21} & Q_{22} \\ \hline \end{array} \right] \quad (4.2-9)$$

The time invariant Ricatti equation for the augmented system becomes

$$0 = \hat{P}\hat{F} + \hat{F}^T\hat{P} - \hat{P}G\hat{R}^{-1}\hat{G}^T\hat{P} + \hat{Q} \quad (4.2-10)$$

Partitioning  $\hat{P}$  according to:

$$\hat{P} = \begin{array}{cc} \begin{array}{|c|c|} \hline n & m \\ \hline P & P_{21}^T \\ \hline P_{21} & P_{22} \\ \hline \end{array} & \begin{array}{|c|} \hline n \\ \hline m \\ \hline \end{array} \end{array} \quad (4.2-11)$$

The Ricatti equation can be decomposed into Eqs. 4.2-12 to 4.2-14.

$$0 = PF + F^TP - PGR^{-1}G^TP + Q \quad (4.2-12)$$

$$0 = P_{21}(F - GR^{-1}G^TP) + A^TP_{21} + Q_{21} \quad (4.2-13)$$

$$0 = P_{22}A + A^TP_{22} - P_{21}GR^{-1}G^TP_{21}^T + Q_{22} \quad (4.2-14)$$

Note that Eq. 4.2-12 is the Ricatti equation corresponding to the optimal regulation of the controllable element by itself; i.e., the disturbance dynamics do not affect this partition of the  $\hat{P}$  matrix. Equations 4.2-12 to 4.2-14 can be solved sequentially; for convenience Eq. 4.2-13 can be rewritten:

$$P_{21}F_{cl} + A^TP_{21} = -Q_{21} \quad (4.2-15)$$

where  $F_{cl}$  is the closed loop F matrix of the active element.

The optimal control gains are given by:

$$K^T = -R^{-1}G^TP \quad (4.2-16)$$

$$K_1^T = -R^{-1}G^T P_{21}^T \quad (4.2-17)$$

Equations 4.2-15 and 4.2-17 indicate that the optimal feedforward controller is determined by the closed loop dynamics of the controllable element ( $F_{c1}$ ), the dynamics of the disturbance (A), the state penalty matrix ( $Q_{21}$ ), and the control penalty matrix (R). Optimal regulator theory insures that the controller derived from the augmented system analysis will yield the minimum cost J consistent with the weightings and dynamics involved.

#### 4.3 PERFORMANCE INDICES FOR ADAPTIVE OPTICS CONTROL DESIGN

In optimal control analysis, the success of a given system design is measured in terms of scalar "cost functional" or performance index. For a regulator or tracking system the performance index generally reflects the integration of a weighted sum of the system output error and the corresponding control effort over a specified period of time. Once the performance index has been chosen, the optimal control of the system is determined by finding the control time history which minimizes this index.

This section outlines the derivation of quadratic performance indices (PI) for candidate high energy laser adaptive optics systems. Physical considerations lead to an exponential weighting function for the phasefront aberrations of the system; approximation by series expansion reduces the exponential function to a quadratic form. A quadratic form is desirable since linear optimal disturbance nulling synthesis is then possible. The guidelines for quadratic PI construction vary significantly between the active multi-

dither (AMD) and the phase conjugate/beam cleanup concepts; hence, the discussion is divided between the two system types.

#### 4.3.1 Development of the State Penalty Matrix, Q

The performance goal of all of the candidate adaptive optics systems is clearly defined on physical grounds: the system should maximize the intensity of incident radiation at a point fixed to the target. The most precise weighting function would therefore be the difference between the maximum achievable target intensity and that actually produced, i.e.

$$f(c_1, c_2, \dots, c_5) = I_{\max} - I(c_1, c_2, c_3, \dots, c_5) \quad (4.3-1)$$

Conversion of Eq. 4.3-1 into a Q matrix requires approximation. If the  $c_i$ 's are all small (as they would be if successfully controlled),  $I(c_1, c_2, c_3, \dots, c_5)$  can be approximated by a series expansion. The general form of the Taylor series for I is:

$$I(c_1, c_2, c_3, \dots, c_5) \approx I(c_{10}, c_{20}, c_{30}, \dots, c_{50}) + \sum_{i=1}^5 \frac{\partial I}{\partial c_i} \Delta c_i + \frac{1}{2} \sum_{i=1}^5 \sum_{j=1}^5 \frac{\partial^2 I}{\partial c_i \partial c_j} \Delta c_i \Delta c_j + \dots \quad (4.3-2)$$

Here the partial derivatives are evaluated at the maximum intensity values of the  $c_i$ 's, signified by  $c_{i0}$ . If terms up to second order are retained, the approximate intensity degradation function becomes:

$$f(\Delta c_1, \Delta c_2, \dots, \Delta c_5) \approx - \left\{ \sum_{i=1}^5 \frac{\partial I}{\partial c_i} \Delta c_i + \frac{1}{2} \sum_{i=1}^5 \sum_{j=1}^5 \frac{\partial^2 I}{\partial c_i \partial c_j} \Delta c_i \Delta c_j \right\} \quad (4.3-3)$$

Phase Conjugate/Beam Cleanup Q Matrix - The maximum target intensity for the phase conjugate and beam cleanup systems is achieved when all of the  $c_i$ 's are zero. At this point all first partial derivatives of Eq. 4.3-1 are zero so that the intensity degradation function reduces directly to the desired quadratic form:

$$f(c_1, c_2, \dots, c_7) = -\frac{1}{2} \sum_{i=1}^5 \sum_{j=1}^5 \frac{\partial^2 I}{\partial c_i \partial c_j} \Delta c_i \Delta c_j \quad (4.3-4)$$

which is the scalar equivalent of the matrix form:

$$f(c_1, c_2, \dots, c_7) = \Delta \underline{c}^T Q_{pc/bc} \Delta \underline{c} \quad (4.3-5)$$

with

$$q_{ij} = -\frac{1}{2} \frac{\partial^2 I}{\partial c_i \partial c_j} \quad (4.3-6)$$

Again, Eq. 4.3-5 expresses the reduction of target intensity as a function of the deviations of the  $c_i$ 's from null, i.e., the desired maximum intensity.

Since the  $c_i$ 's enter the target intensity function, Eq. 2.3-1, as squares, i.e.  $I = I(c_1^2, c_2^2, \dots, c_5^2)$ , all of the second derivatives also vanish

$$q_{ij} = \frac{\partial^2 I}{\partial c_i \partial c_j} = 0 \text{ for } i \neq j \quad (4.3-7)$$

Q, therefore, is a diagonal matrix with:

$$q_{ii} = -\frac{1}{2} \frac{\partial^2 I}{\partial c_i^2} \quad (4.3-8)$$

Differentiating Eq. 2.3-1 the  $q_{ii}$ 's for the tilt and focus modes are:



$$q_{11} = -\frac{1}{2} \frac{\partial^2 I}{\partial c_1^2} = I_{\max} \frac{k^2}{4} \quad (4.3-9)$$

$$q_{22} = -\frac{1}{2} \frac{\partial^2 I}{\partial c_2^2} = I_{\max} \frac{k^2}{4} \quad (4.3-10)$$

$$q_{33} = -\frac{1}{2} \frac{\partial^2 I}{\partial c_3^2} = I_{\max} \frac{k^2}{3} \quad (4.3-11)$$

The  $q_{ii}$ 's for the remaining modes are proportional to derivatives of the Strehl ratio:

$$q_{44} = q_{55} = I_{\max} \frac{1}{6} k^2 \quad (4.3-12)$$

Physically, the  $q_{11}$ ,  $q_{22}$ ,  $q_{33}$  elements weight intensity degradation due to beam tilt and focus plane displacements;  $q_{44}$  and  $q_{55}$  weight the relative beam-broadening effects of the astigmatism modes.

Active Multidither Q Matrix - When dither signals are introduced, the maximum achievable intensity no longer corresponds to the stationary point of the Gaussian intensity function. If the phasefront is dithered with square waves, as it would be in a digital application, the desired intensity is given by Eq. 2.3-1 evaluated at the nominal dither amplitude, i.e.

$$c_{i0} = d_i, i=1, \dots, 5 \quad (4.3-13)$$

$$I_0 = I(c_{10}, c_{20}, \dots, c_{50}) \quad (4.3-14)$$

Since the nominal operating point is not at the peak of the Gaussian function all of the coefficients of the first order term of Eq. 4.3-3 are nonzero. Neglecting the second order terms of Eq. 4.3-3, the intensity degradation function becomes:

$$f(\Delta c_1, \Delta c_2, \dots, \Delta c_7) \approx - \sum_{i=1}^7 \frac{\partial I}{\partial c_i} \Delta c_i = (\nabla I)^T \Delta \underline{c} \quad (4.3-15)$$

Since the  $\Delta c_i$ 's are independent variables, the distance of the actual operating point from nominal is given by:

$$\left[ \sum_{i=1}^7 \left( \frac{\partial I}{\partial c_i} \right)^2 \Delta c_i^2 \right]^{1/2} = \left\{ \Delta \underline{c}^T \left[ \left( \frac{\partial I}{\partial c_i} \right)^2 \right] \Delta \underline{c} \right\}^{1/2} \quad (4.3-16)$$

$$= \left\{ \Delta \underline{c}^T Q_{AMD} \Delta \underline{c} \right\}^{1/2} \quad (4.3-17)$$

The derived  $Q_{AMD}$  penalizes the square of the "distance" between the operating point and the desired nominal point defined by the dither.

The  $Q$  obtained is diagonal; the  $q_{ii}$ 's for the AMD performance index are given by:

$$q_{ii} = \left( \frac{\partial I}{\partial c_i} \right)^2 \quad (4.3-18)$$

$$q_{11} = \left\{ \frac{I_0}{2} k^2 \beta_0 c_{10} \exp \left[ - \frac{1}{3} k^2 c_{30}^2 \right] \right\}^2 \quad (4.3-19)$$

$$q_{22} = \left\{ \frac{I_0}{2} k^2 \beta_0 c_{20} \exp \left[ - \frac{1}{3} k^2 c_{30}^2 \right] \right\}^2 \quad (4.3-20)$$

$$q_{33} = \left\{ I_0 \frac{2}{3} k^2 c_{30} \left[ 1 - \frac{\beta_0}{4} k^2 (c_{10}^2 + c_{20}^2) \exp \left[ - \frac{1}{3} k^2 c_{30}^2 \right] \right] \right\}^2 \quad (4.3-21)$$

$$q_{44} = \left\{ I_0 \frac{1}{3} k^2 \frac{c_{40}}{\beta_0} \left[ 1 - \frac{\beta_0}{4} k^2 (c_{10}^2 + c_{20}^2) \exp \left[ - \frac{1}{3} k^2 c_{30}^2 \right] \right] \right\}^2 \quad (4.3-22)$$

$$q_{55} = \left\{ I_0 \frac{1}{3} k^2 \frac{c_{50}}{\beta_0} \left[ 1 - \frac{\beta_0}{4} k^2 (c_{10}^2 + c_{20}^2) \exp \left[ - \frac{1}{3} k^2 c_{30}^2 \right] \right] \right\}^2 \quad (4.3-23)$$

The "0" subscript indicates the nominal magnitude.

#### 4.3.2 Development of the Control Penalty Matrix, R

While the Q matrices were derived from explicit system goals and physical arguments, the R matrices will be constructed to reflect the estimated relative cost of control effort, and to maintain performance limits within the capabilities of the adaptive optics components. The rationale for development of an R matrix depends on the particular component involved and, in the present case, will necessarily be a result of the design process. In Section 4.4 the R's for the tilt and focus mirrors are determined in designing inner control loops for these components. The R matrix for the deformable mirror is determined in a rather unconventional manner; Section 4.5 summarizes this design approach.

#### 4.4 INNER LOOP DESIGN - TILT AND FOCUS MIRRORS

In this section the design of the inner control loops for the tilt and focus mirrors is described. Since the tilt and focus mirror dynamic models are rotational and translational analogs of each other, the detailed analysis presented here is restricted to determining the feedback gains for one of the tilt mirror axes. The feedback gains for the focus mirror can be obtained by a procedure identical to that used for the tilt mirror.

##### 4.4.1 Control Objectives - Performance Indices

The control objectives for the tilt mirror are

- Extend mirror surface response bandwidth to 1000 Hz ( $\approx 6280$  rad/sec)
- Maintain a stable mount compliance mode response.

The corresponding specifications for the focus mirror are:

- Extend secondary mirror position response bandwidth to 500 Hz
- Maintain a stable mount compliance mode response.

These specifications reflect a desire to improve hardware response bandwidths to current or soon-expected standards, as well as a concern for potential instabilities of structural (mount compliance) modes that may result from this increased bandwidth.

Since the tilt and focus mirrors are single input-single output devices (the two tilt axes respond independently) the R matrix of the quadratic performance index reduces to a scalar which is balanced against a single diagonal element of the Q matrix derived in Section 4.3. The mathematical results will show that the bandwidth of the closed loop system is determined by the ratio  $q/r$ ,  $q$  and  $r$  being the state and control weighting scalars, respectively. With  $q$  fixed by the results of Section 4.3,  $r$  is chosen to achieve the specified response bandwidth.

#### 4.4.2 The Solution Technique

Determining the optimal feedback gains for a time invariant regulator involves solution of the steady-state Ricatti equation. In the case of the tilt mirror, the coefficient matrices for the Ricatti equation, Eq. 4.4-1, are given by Eqs. 4.4-2 to 4.4-6.

$$PF + F^T P - PGR^{-1}G^T P + Q = 0 \quad (4.4-1)$$

$$F = \begin{bmatrix} 0 & 1 & 0 & 0 & 0 \\ -\omega_h^2 & 0 & \omega_h^2 & 0 & \omega_h^2 \\ 0 & 0 & 0 & 1 & 0 \\ \omega_h^2 I' & 0 & -(\omega_h^2 I' + \omega_m^2) & 0 & -\omega_h^2 I' \\ 0 & 0 & 0 & 0 & -\frac{1}{\tau_1} \end{bmatrix} \quad (4.4-2)$$

$$G^T = (0, 0, 0, 0, 1/\tau_1) \quad (4.4-3)$$

$$R^{-1} = \frac{1}{r}; \quad \text{a scalar} \quad (4.4-4)$$

$$Q = HqH^T \quad (4.4-5)$$

$$H^T = (1, 0, 0, 0, 0) \quad (4.4-6)$$

There are a number of alternative methods for solving Eq. 4.4-1, such as integrating the Ricatti differential equation to steady state or using various numerical iteration techniques. The technique used in the present study was the singular perturbation method as developed by Sannuti and Kokotovic (Ref. 10). Singular perturbation takes advantage of the characteristic frequency disparity between the mirror-flexure hinge dynamics and the mount compliance and actuator responses to effectively reduce the order of the dynamic system. A complete discussion of the technique would be inappropriate here although some of the major features should be mentioned. (The interested reader is encouraged to examine Ref. 10.) The technique:

- Reduces the order of the Ricatti equation down to that of the dominant slow dynamics; the fast

dynamics (such as the mount compliance mode dynamics) are considered as a perturbation

- Control gains are obtained as a two-term perturbation expansion. The leading order term of the expansion controls the dominant slow dynamics; the second term maintains stability of the fast dynamics and "patches up" the control of slow dynamics to account for coupling of the fast modes.

In this particular design, singular perturbation reduces the fifth order system to the second order dynamics of the mirror-flexure hinge mode (i.e.,  $x_1$  and  $x_2$ ); the mount compliance and actuator dynamics are considered as a perturbations. The reduced order Ricatti equation is simple enough that it can be solved analytically. The equations for the second term of the perturbation expansion for the gains can also be solved analytically; the resulting gains are given by:

$$\underline{K}^T = \underline{K}_0^T + \epsilon \underline{K}_1^T \quad (4.4-7)$$

$$= (b, \sqrt{2b}, 0, 0, 0) + \epsilon (-\omega_m \tau_1 \sqrt{2b}, \omega_m \tau_1 b, 0, \frac{\sqrt{2b}}{\omega_m}, \omega_m \tau_1 \sqrt{2b}) \quad (4.4-8)$$

with:

$$\epsilon = \frac{\omega_h}{\omega_m} \ll 1 \quad (4.4-9)$$

$$b = -1 + \sqrt{1 + \left(\frac{q}{r}\right)} \quad (4.4-10)$$

The first term of Eq. 4.4-8 feeds back position and rate of the mirror surface motion, thereby extending the mirror bandwidth and improving the damping of the mirror-flexure hinge mode. The second term is of small magnitude compared to the first since it is multiplied by a small number,  $\epsilon$ . The first

two elements of the second term "patch up" the mirror position and rate terms to account for the destabilizing effects of mount compliance mode coupling and actuator lag. Mirror position feedback is decreased slightly; rate feedback is increased slightly; the net effect is a small increase in the damping of the mirror surface dynamics. The fourth element of the second term feeds back a control proportional to the rate of the mount compliance mode. The metastable (undamped) dynamics of this mode became unstable as a result of the  $K_0$  feedbacks; a small amount of rate feedback will restabilize it. Finally, the bandwidth of the actuator is increased slightly by the fifth element of the second term.

The natural frequency and, hence, the bandwidth of the reduced order dynamics (second order mirror-flexure hinge dynamics and  $K_0$  gains) is:

$$\omega^2 = \omega_h^2 + \omega_h^2 b \quad (4.4-11)$$

$$= \omega_h^2 \sqrt{1 + \left(\frac{q}{r}\right)} \quad (4.4-12)$$

$$\omega = \omega_h^4 \sqrt{1 + \left(\frac{q}{r}\right)} \quad (4.4-13)$$

$\approx$  Mirror response bandwidth

Using Eq. 4.4-13, a bandwidth specification can be readily converted to a q/r ratio:

$$\frac{q}{r} = \left(\frac{\omega}{\omega_h}\right)^4 - 1 \quad (4.4-14)$$

Equations 4.4-8 to 4.4-10 can be modified to yield gains for the focus mirror by a few simple changes in notation:

$$\underline{K}_0^T + \epsilon \underline{K}_1^T = (b, \sqrt{2b}, 0, 0, 0) + \epsilon(-\omega_m \tau_1 \sqrt{2b}, \omega_m \tau_1 b, 0, \frac{\sqrt{2b}}{\omega_m}, \omega_m \tau_1 \sqrt{2b})$$

(4.4-15)

$$\epsilon = \frac{\omega_s}{\omega_m} \ll 1$$

(4.4-16)

In summary, a controller has been designed which meets the specifications listed in Section 4.4.1. The solution technique used yielded the optimal regulator gains in closed form, as well as approximate expressions for the closed loop bandwidth. Using the closed form expressions, new gains can be readily computed to accommodate changes in mirror parameters or control specifications.

#### 4.5 DEFORMABLE MIRROR CONTROLLER DESIGN

In a number of practical design situations, synthesis of an optimal control system is hampered by the presence of an inalterable dynamic element. In flight vehicle control engineering, for example, the lag dynamics of the control surface actuators may be inalterable due to the lack of a feedback measurement; i.e. the actuator dynamics states are unobservable. In man-vehicle control analysis, the dynamics of the neuro-muscular lags of the pilot are fixed; one cannot close an inner loop around the pilot himself. In the control of higher order aberrations in adaptive optics a deformable mirror is used which has inalterable dynamics, i.e., no measurement of the mirror figure is available to construct an inner feedback loop.

The inalterable dynamics of the deformable mirror call for a unique approach to the optimal disturbance nulling control problem; this approach and the resulting feedforward controller design are described in this section.



#### 4.5.1 Pseudo-Optimal Control Design

An approach to optimal control synthesis for systems having inalterable elements is pseudo-optimal control. The pseudo-optimal control concept is to identify a dynamic subsystem within a desired optimal system structure that can be replaced by the dynamics of the inalterable elements. After the inalterable element is substituted into the role of the dynamic subsystem, the remainder of the desired system control is optimized about that starting point. This design methodology yields the "best" control system which can exist while also incorporating the inalterable element.

The application of the pseudo-optimal design philosophy to control of a deformable mirror is illustrated by a comparison of Fig. 4.5-1 with Fig. 4.5-2. The design goal is to find the best gain matrix  $K_1^T$  to be used with the existing mirror dynamics. To this end, the dynamics of the deformable mirror are cast in the role of the closed loop element encircled in Fig. 4.5-2. As Fig. 4.5-1 and 4.5-2 suggest, the pseudo-optimal control synthesis consists of finding a fictitious regulator problem having the deformable mirror dynamics as the final closed loop solution, and then solving the remainder of the optimal disturbance nulling control problem. The general mathematical procedure to be used in pseudo-optimal control design for the deformable mirror is outlined in the following section.

#### 4.5.2 The Mathematical Design Procedure

The computation of the optimal gains  $K_1^T$  to be used with the deformable mirror is considered as two subproblems:

- Construction of an appropriate fictitious regulator problem

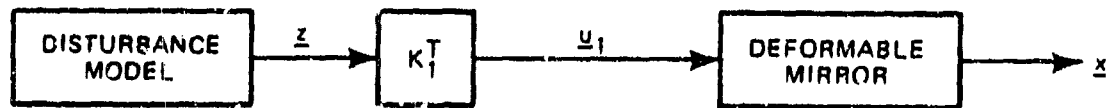


Figure 4.5-1 Deformable Mirror Controller

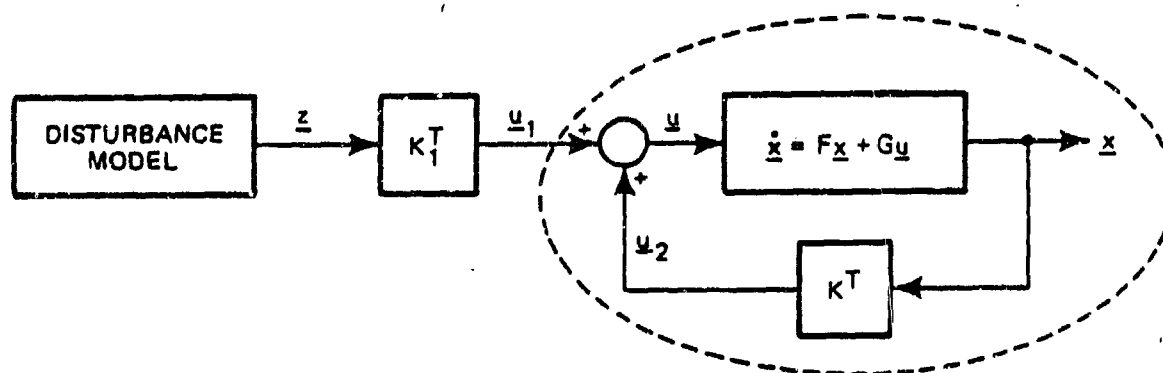


Figure 4.5-2 Optimal Model Following (Nulling) Control Structure

- Design of the feedforward controller.

The first subproblem is an involved process which requires some reader familiarity with asymptotic (perturbation) techniques. A detailed solution of the fictitious regulator problem is presented in Ref. 11; the major points of the design process will be summarized here:

- Mirror dynamics are characterized as a set of weakly coupled second order systems (see Section 2.2.3)

- Mirror dynamics and associated Ricatti equations are decomposed through asymptotics
  - Primary second order dynamics become uncoupled
  - Cross-coupling effects are treated as a perturbation to primary dynamics
- Fictitious regulator is developed for the decomposed mirror model.

The result required from the fictitious regulator problem is the  $R^{-1}$  matrix (inverse of the control weighting matrix). Using the asymptotic approach, the elements of the  $R^{-1}$  matrix were obtained in closed form; formulae for the elements are given by Eq. 4.5-1 and 4.5-2:

$$R_{mm}^{-1} = \frac{4}{q_m} \zeta^2 (1 - \zeta^2) \quad (\text{diagonal elements}) \quad (4.5-1)$$

$$R_{mn}^{-1} = R_{nm}^{-1} = \frac{-2\zeta\omega}{\omega^4 q_m q_n} \left\{ \zeta\omega (q_m f_{1_{mn}} + q_n f_{1_{nm}}) + \omega^2 (1 - 2\zeta^2) (q_m f_{2_{mn}} + q_n f_{2_{nm}}) \right\} \quad (4.5-2)$$

where:

$\zeta, \omega$  are the damping ratio and natural frequency of the primary second order dynamics

$f_{1_{mn}}, f_{2_{mn}}$  are the position and rate coupling terms of primary mode n into primary mode m

With Eq. 4.5-1 and 4.5-2 the feedforward controller can be designed directly; the fictitious regulator problem need not be solved for every design. Repeating results from Section 4.2:

$$K_1^T = -R^{-1} G^T P_{21}^T \quad (4.5-3)$$

where  $P_{21}$  is derived from the mirror and disturbance dynamics according to:

$$P_{21}F + A^T P_{21} = -Q_{21} \quad (4.5-4)$$

where  $F$  and  $A$  are the dynamics matrices of the mirror and disturbance, respectively.

In summary, the essential steps in designing a pseudo-optimal controller for the deformable mirror are:

- Compute the elements of the  $R^{-1}$  matrix of the fictitious regulator using Eq. 4.5-1 and 4.5-1
- Determine  $P_{21}$  from Eq. 4.5-4 using the mirror  $F$  matrix and the  $A$  matrix of the disturbance models
- Calculate the feedforward gains  $K_1^T$  from Eq. 4.5-3.

A final scalar adjustment of the  $K_1^T$  matrix is required; the justification of this adjustment is given in Section 4.6.

#### 4.5.3 Description of the Deformable Mirror Controller

The controller  $K_1^T$  has primary and secondary functions. The primary function of the controller is to command a linear combination of the states of a disturbance model to its corresponding primary dynamics in the deformable mirror. The secondary function is to crossfeed linear combinations of the remaining disturbance model states to suppress cross-coupling. These two control functions are depicted for a two disturbance system in Fig. 4.5-3 and 4.5-4.

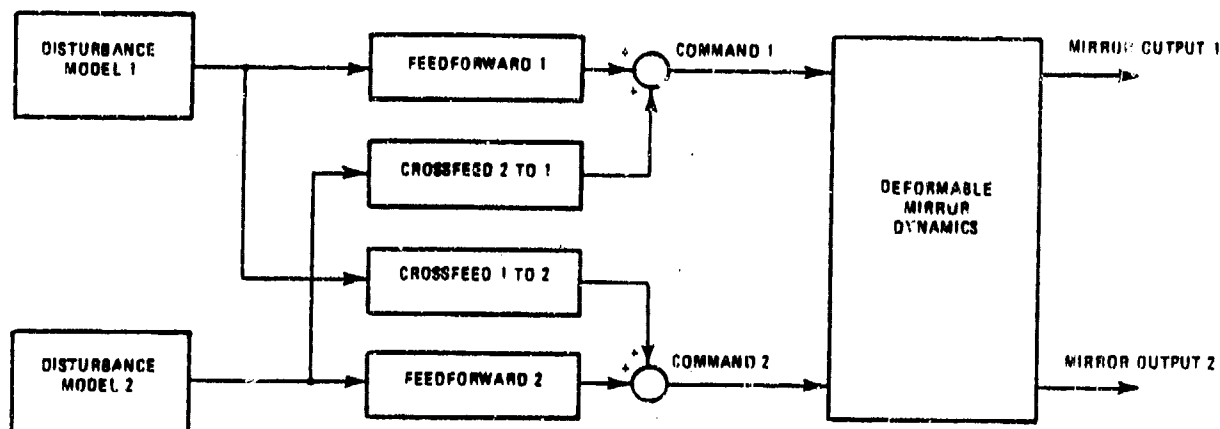


Figure 4.5-3 Functional Block Diagram of Two-Disturbance Controller

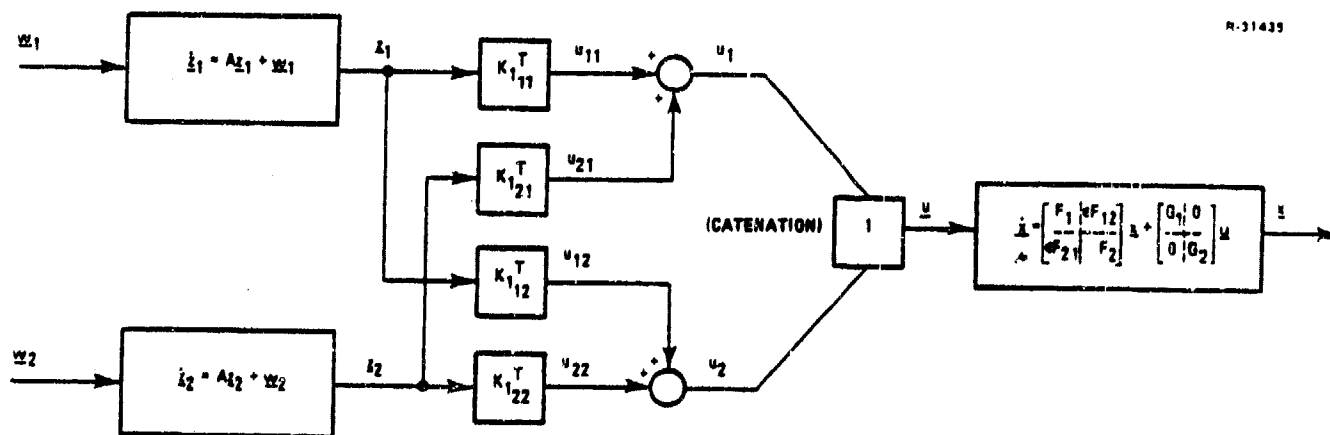


Figure 4.5-4 Mathematical Block Diagram of Two-Disturbance Controller

The primary and secondary functions can be readily extended to an arbitrary number of coupled second order systems, i.e. the dynamics of the deformable mirror as described in Section 2.2.3. This extension is described in Ref. 11.

#### 4.6 PRELIMINARY PERFORMANCE EVALUATION

Performance and sensitivity studies of modern control designs for adaptive optics components are presented in this section. Again, the estimation problem has been separated from the control design (disturbance states are available directly from the truth model) so that control performance can be isolated from all other effects that may influence system performance. Studies were conducted for the tilt channel and the deformable mirror channel; since the focus channel has directly analogous disturbance and mirror dynamics, performance results similar to those for the tilt channel are implied.

The following studies will be presented here:

- Tilt Channel (and Focus)
  - Disturbance nulling performance compared to that of a classical design
  - Sensitivity of optimal controller performance to tilt mirror bandwidth
  - Sensitivity of optimal controller performance to truth model/design model mismatches
- Deformable Mirror Channel
  - Disturbance nulling performance including mirror modal cross-coupling effects
  - Comparison of performance with classical inverse filter controller.

#### 4.6.1 Tilt Channel Performance/Sensitivity

Figures 4.6-1 and 4.6-2, respectively, show block diagrams of an optimal disturbance nulling controller and a classical direct measurement-command controller for the tilt channel. The exponential hold in Fig. 4.6-1 has continuous dynamics identical to those of the tilt disturbance; its purpose is to smooth the sampled  $z$  between updates. The tilt mirror and feedback loop are identical for the two systems; the control specifications and control design are described in Section 4.4. The scalar gain  $K$  provides a unity DC gain from  $C_1(t_k)$  to  $C_1'$  in the classical system.

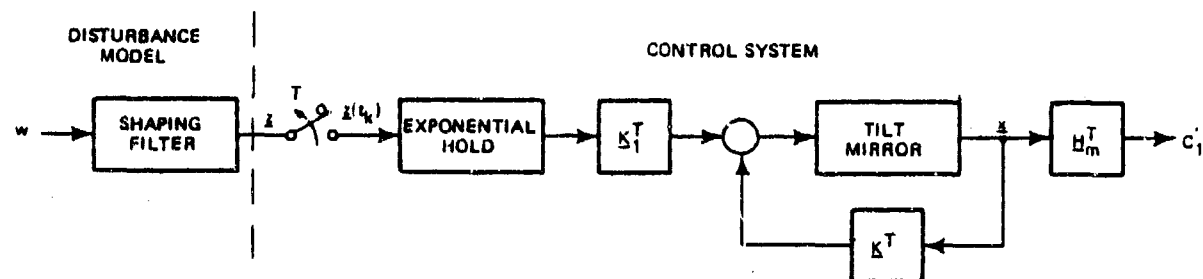


Figure 4.6-1 Optimal Model Following Controller for Turbulence-Induced Tilt

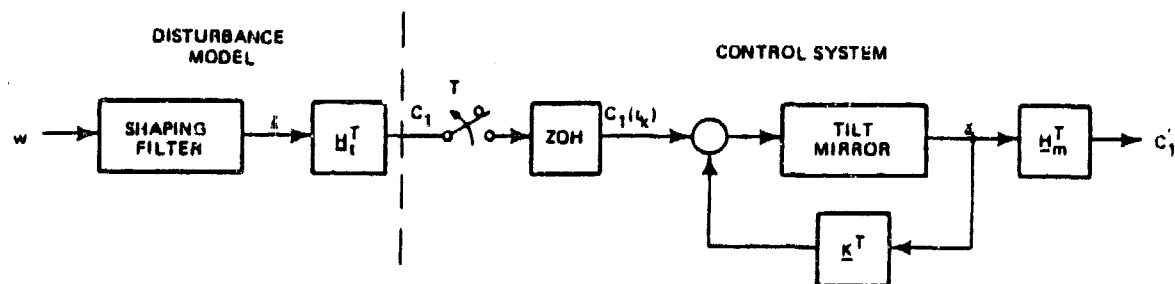


Figure 4.6-2 Classical Direct-Command Controller

Figure 4.6-3 shows the nulling error variances for the two systems as a function of control sample rate. The autocorrelation function for a first order shaping filter (9 Hz bandwidth) was used to derive the third curve; this curve establishes an upper bound on transport lag effects. The continuous system lines are asymptotic limits of the digital system curves for high sample rates.

The optimal system shows consistently superior performance at all sample rates and exceeds the performance of the continuous classical system at a sample frequency of 1200 Hz. The optimal system offers significant advantages over the classical in data processing (sample rate) requirements.

In addition to an alleviation of sample rate requirements the optimal controller can maintain good performance with lower grade hardware (lower response bandwidth). Figure 4.6-4

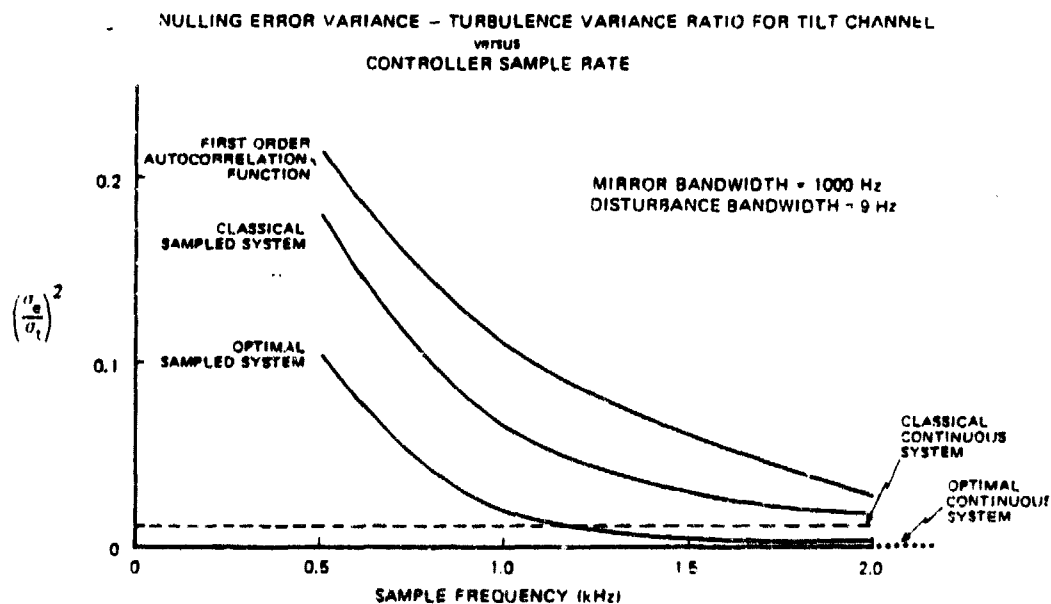


Figure 4.6-3 Nulling Error Comparison Between Classical and Optimal Controllers



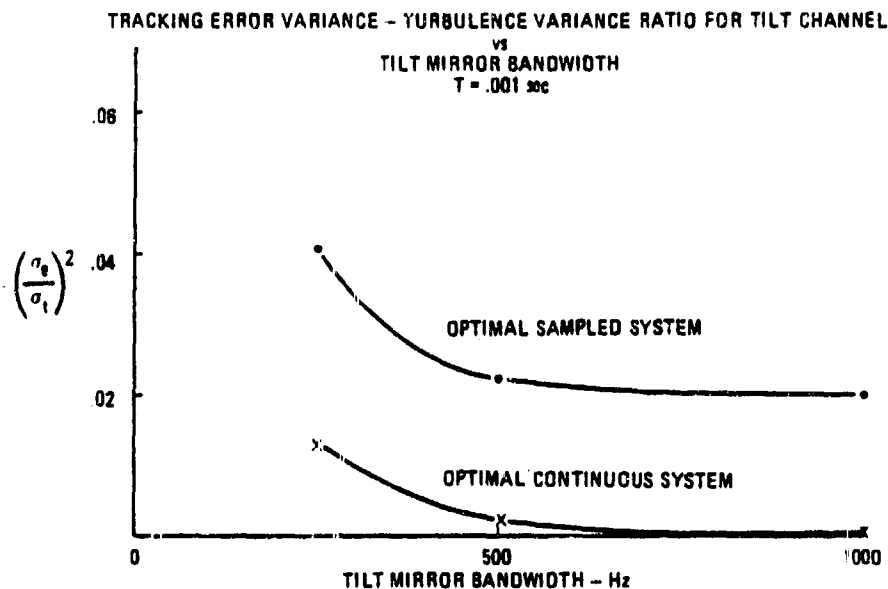


Figure 4.6-4 Nulling Error Variance Versus Tilt Mirror Bandwidth

shows the nulling error variance of the tilt channel controller as a function of tilt mirror bandwidth. The error variance reaches a point of diminishing return at 500 Hz; there is little to be gained by increasing mirror bandwidth. Since a higher response bandwidth generally implies high quality (expensive) hardware, use of an optimal controller could have a significant impact on component development goals and cost.

The optimal system is quite insensitive to mismatches between the design disturbance model (used to design controller and holding circuit) and the truth model. Figure 4.6-5 shows that design model bandwidth errors of  $\pm 20\%$  yield insignificant changes in nulling error variance. The bandwidths of the turbulence disturbances are proportional to the local wind velocity (Ref. 1); hence, the optimal controller might be thought to be

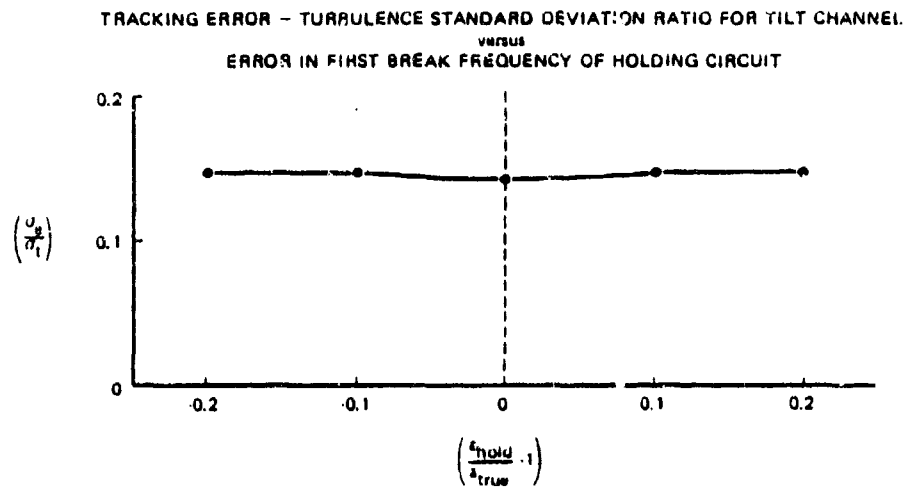


Figure 4.6-5 Tilt Channel Mismatch Sensitivity

tolerant to  $\pm 20\%$  errors in measured wind velocity; however, errors in the turbulence model bandwidths will also be present due to uncertainty in the modeled relationship between wind velocity and turbulence bandwidth.

In summary, the tilt channel optimal controller offers:

- Disturbance nulling performance superior to that of a typical classical design
- Compensation of low bandwidth hardware to yield performance comparable to that of higher quality components
- Insensitivity of the design to disturbance model mismatches.

#### 4.6.2 Deformable Mirror Control Evaluation

In early evaluation of the deformable mirror it was found that a final scalar adjustment of the gain matrix derived from the pseudo-optimal control results (summarized in Section 4.5) is required to achieve proper disturbance nulling. The inadequacy of the pseudo-optimal feedforward control is evidenced in Fig. 4.6-6 which shows an astigmatism time history and the mirror output (negated) that attempts to counteract it. The mirror output is, very nearly, a scalar attenuation of the desired signal; this attenuation is a result of a spurious restriction on control magnitude imposed by the  $R^{-1}$  matrix of the fictitious regulator. Consider the relationship for the diagonal elements of the  $R^{-1}$  matrix, i.e., those elements which determine the magnitude of the primary disturbance nulling control commands.

$$r_i^* = R_{ii}^{-1} = \frac{4}{q_i} \zeta^2 (1 - \zeta^2) \quad (4.5-1)$$

The magnitude of this term determines how much of the disturbance states "gets through" to command the mirror. For example, with:

$$\zeta = .1 \quad (4.6-1)$$

$$r_i^* = \frac{.0396}{q_i} \quad (4.6-2)$$

The maximum value of  $r_i^*$  occurs when  $\zeta = \sqrt{2}/2$ ; i.e.:

$$\text{for } \zeta = \sqrt{2}/2$$

$$r_i^* = \frac{1}{q_i} \quad (4.6-3)$$

If the damping ratio of the mirror is less than  $\sqrt{2}/2$ ,

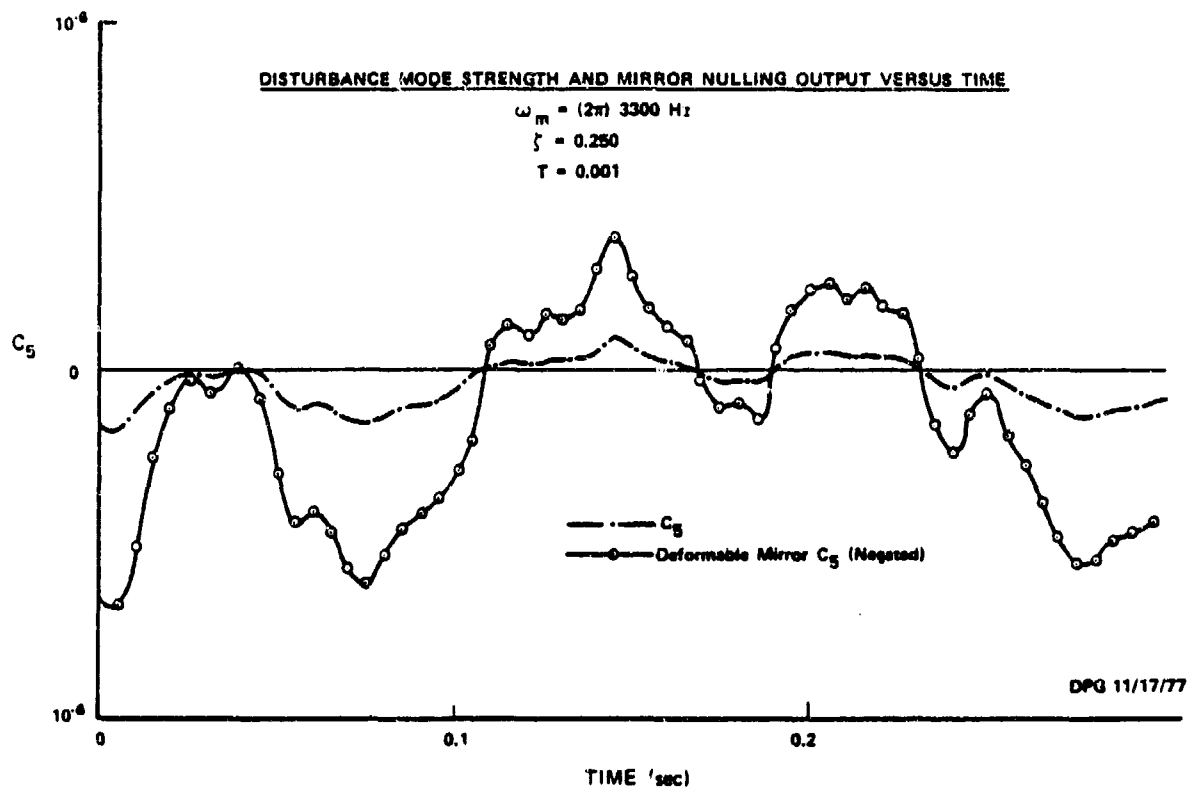


Figure 4.6-6 Disturbance and Deformable Mirror Time Histories

the fictitious regulator derived will represent an optimization problem for which there is a restriction on control magnitude; i.e., the value of  $r_1^*$  serves to attenuate control commands.

A simple artifice to relax this undesirable restriction is to scale up the derived  $R^{-1}$  matrix by the factor:

$$\text{S.F.} = \left[ 4\zeta^2(1-\zeta^2) \right]^{-1} \quad (4.6-4)$$

This scaling has the effect of making the diagonal elements of the  $R^{-1}$  matrix equal to those for the  $\zeta = \sqrt{2}/2$  case (which imposes no attenuation of control commands) and increasing the off-diagonal elements to maintain the proper proportion of

crossfeed. The success of the  $R^{-1}$  scaling artifice is illustrated by the results of the following example problem.

Figures 4.6-7 and 4.6-8 are block diagrams which show, respectively, the optimal control system for the deformable mirror developed in Section 4.5 and a classical inverse-filter control system.

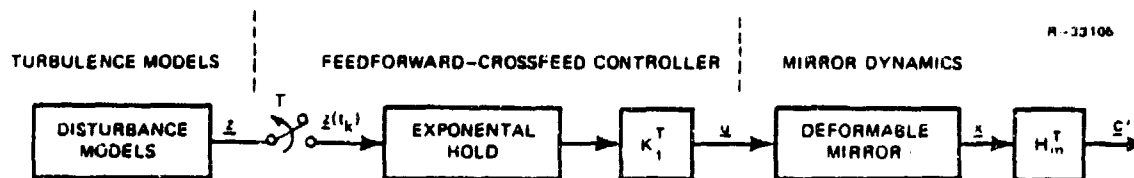


Figure 4.6-7 Deformable Mirror Optimal Control System

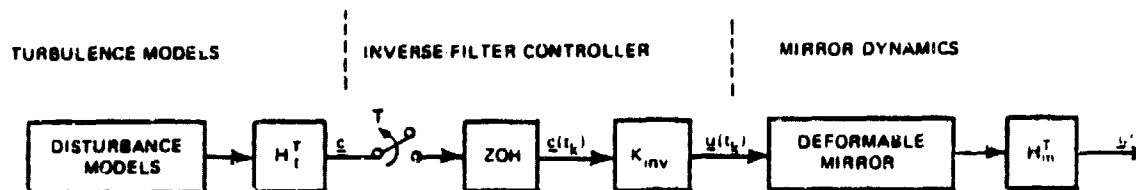


Figure 4.6-8 Classical Inverse Filter Control System

The inverse filter computes controls assuming that the deformable mirror reaches steady state between samples: i.e. with the mirror dynamics defined by:

$$\dot{\underline{x}} = F\underline{x} + G\underline{u} \quad (4.6-5)$$

in steady state:

$$0 = F\underline{x}(t_k) + G\underline{u}(t_k) \quad (4.6-6)$$

and

$$\tilde{\underline{x}}(t_k) = (H_m H_m^T)^{-1} H_m \underline{c}(t_k) \quad (4.6-7)$$

therefore:

$$\underline{u}(t_k) = - (G^T G)^{-1} G^T F (H_m H_m^T)^{-1} H_m \underline{c}(t_k) \quad (4.6-8)$$

The inverse filter approach depends primarily on high mirror bandwidth to achieve the steady state assumption and high sample rate to avoid transport lag effects.

Primary control of the two astigmatism disturbances with suppression of mirror focus cross-coupling was used as a test case to compare the performance of the two systems. The astigmatism truth models chosen were those for the phase conjugate scenario. For very low disturbance bandwidths, such as those of the AMD scenario, the optimal controller for the 3300 Hz bandwidth deformable mirror reduces (very nearly) to an inverse filter controller; the classical and optimal controllers are identical. Amplitude cross-couplings into focus of 2% and 3%, respectively, for the two astigmatism modes were included in the mirror dynamics; i.e. the coefficient coupling amplitude of optical mode 4 into optical mode 3 is

$(-.02)\omega_m^2$ ; the coefficient for mode 5 into mode 3 is  $(-.03)\omega_m^2$ .

Figures 4.6-9 through 4.6-11 summarize the error nulling performance of the two systems. Figure 4.6-9 shows the nulling error variances of the two astigmatism modes as a function of damping ratio; the optimal controller outperforms the inverse filter controller at all damping ratios. Figure 4.6-10 shows the variance of the focus mode produced by cross-coupling. The curve for the optimal controller shows a very low variance for the focus coupling: roughly  $10^{-16}m^2$  as opposed to  $10^{-12}m^2$  for atmospheric turbulence focus disturbances. The focus cross-coupling variances for the inverse filter controller are roughly two orders of magnitude lower than those of the optimal system; the primary control responses of the optimal controller produce cross-couplings which are more difficult to suppress than those produced by the piecewise constant inverse filter commands. Figure 4.6-11 shows the normalized intensity degradation for the two systems, i.e. the intensity degradation produced with control of astigmatism divided by that produced with no control of astigmatism. The optimal controller again outperforms the inverse filter; .052 normalized intensity degradation for the optimal system versus .072 for the inverse filter.

In summary, the optimal controller for the deformable mirror has the following qualities:

- Primary control of astigmatism superior to that of an inverse filter controller
- Adequate suppression of cross-coupling dynamics
- Lower overall intensity degradation than inverse filter controller.

**NULLING ERROR VARIANCE VERSUS DEFORMABLE MIRROR DAMPING RATIO**

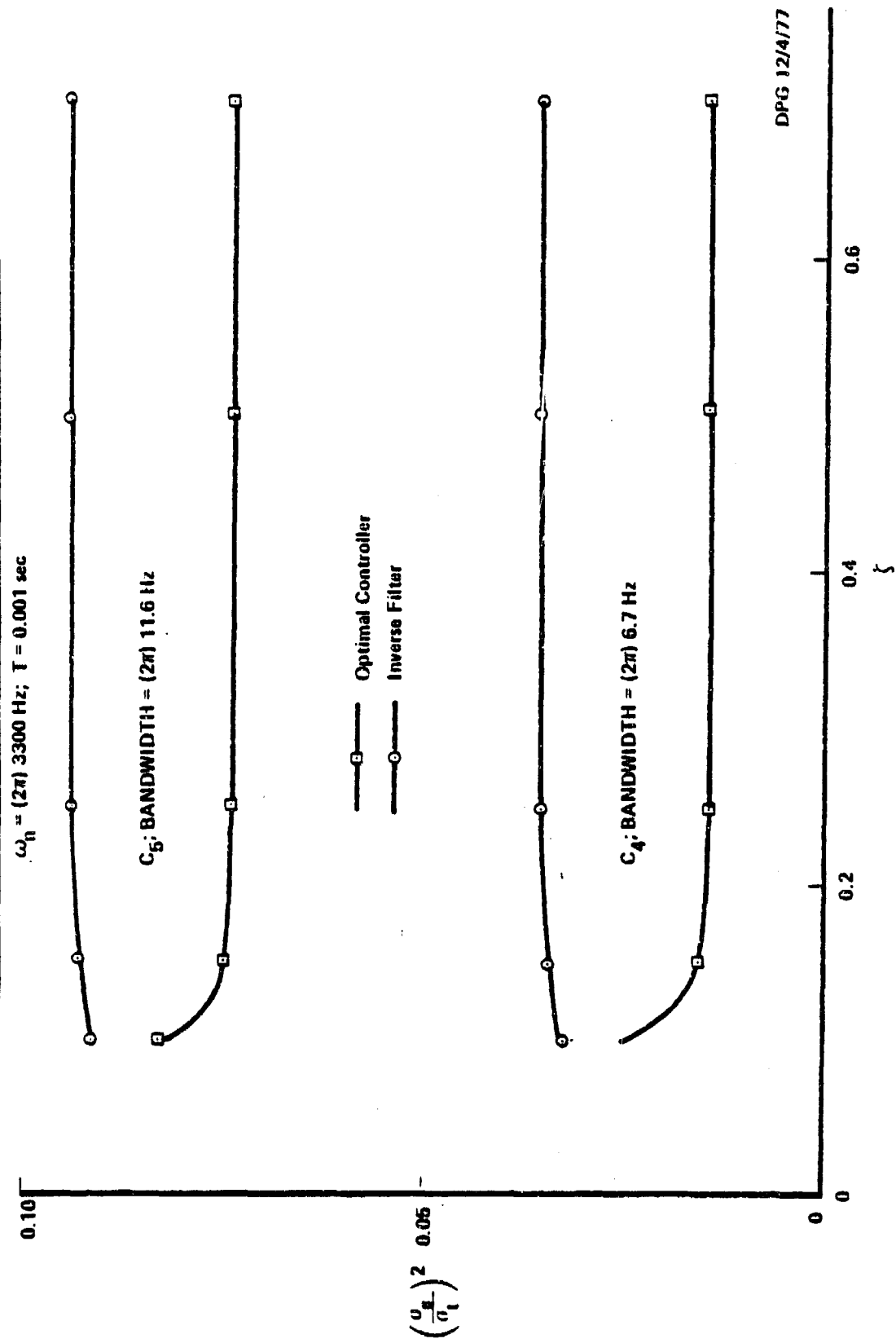


Figure 4.6-9 Astigmatism Nulling Error Variances



FOCUS COUPLING VARIANCE VERSUS DEFORMABLE MIRROR DAMPING RATIO

$$\omega_n = (2\pi) 3300 \text{ Hz}$$

$$T = 0.001 \text{ sec}$$

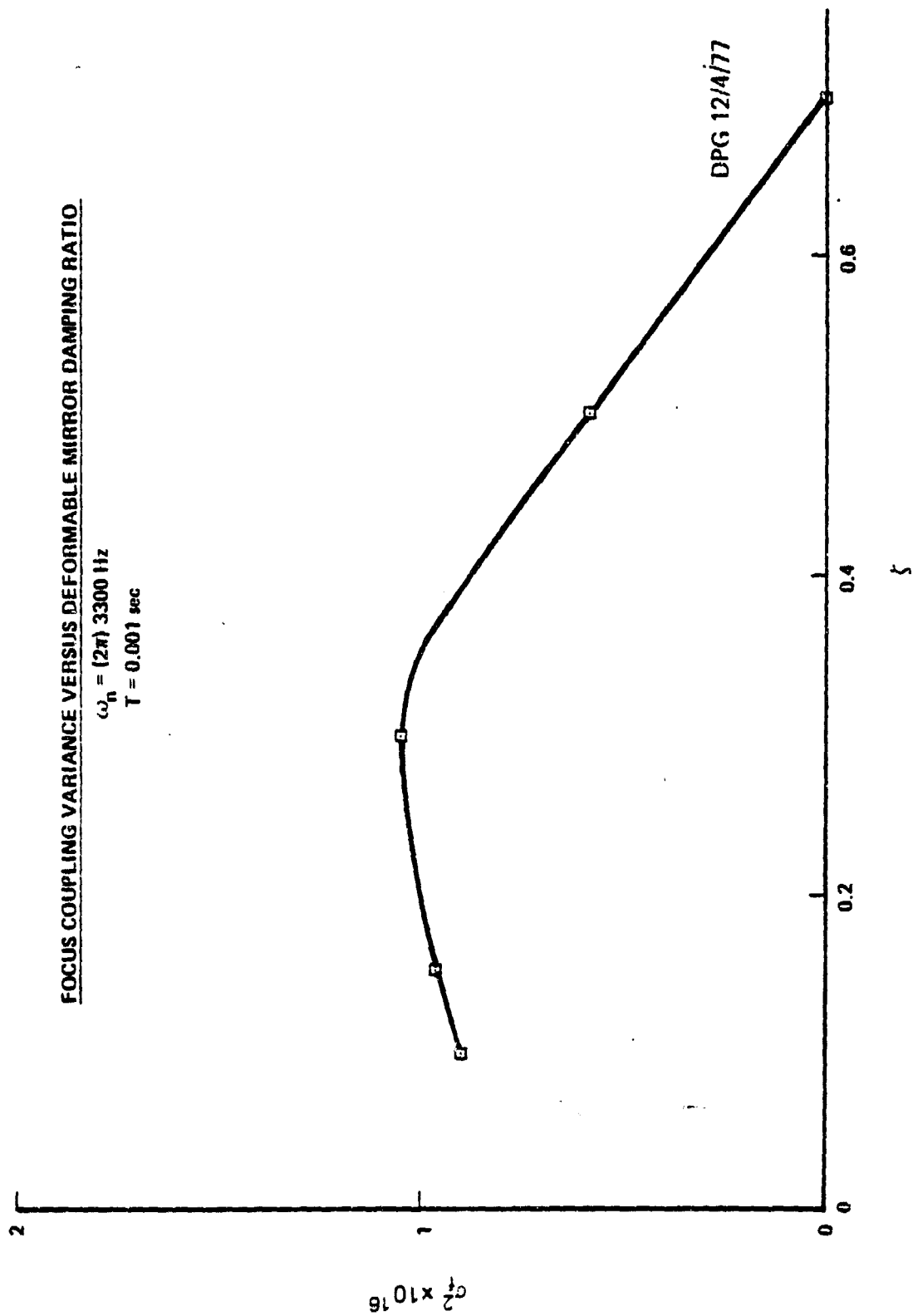


Figure 4.6-10 Focus Cross-Coupling

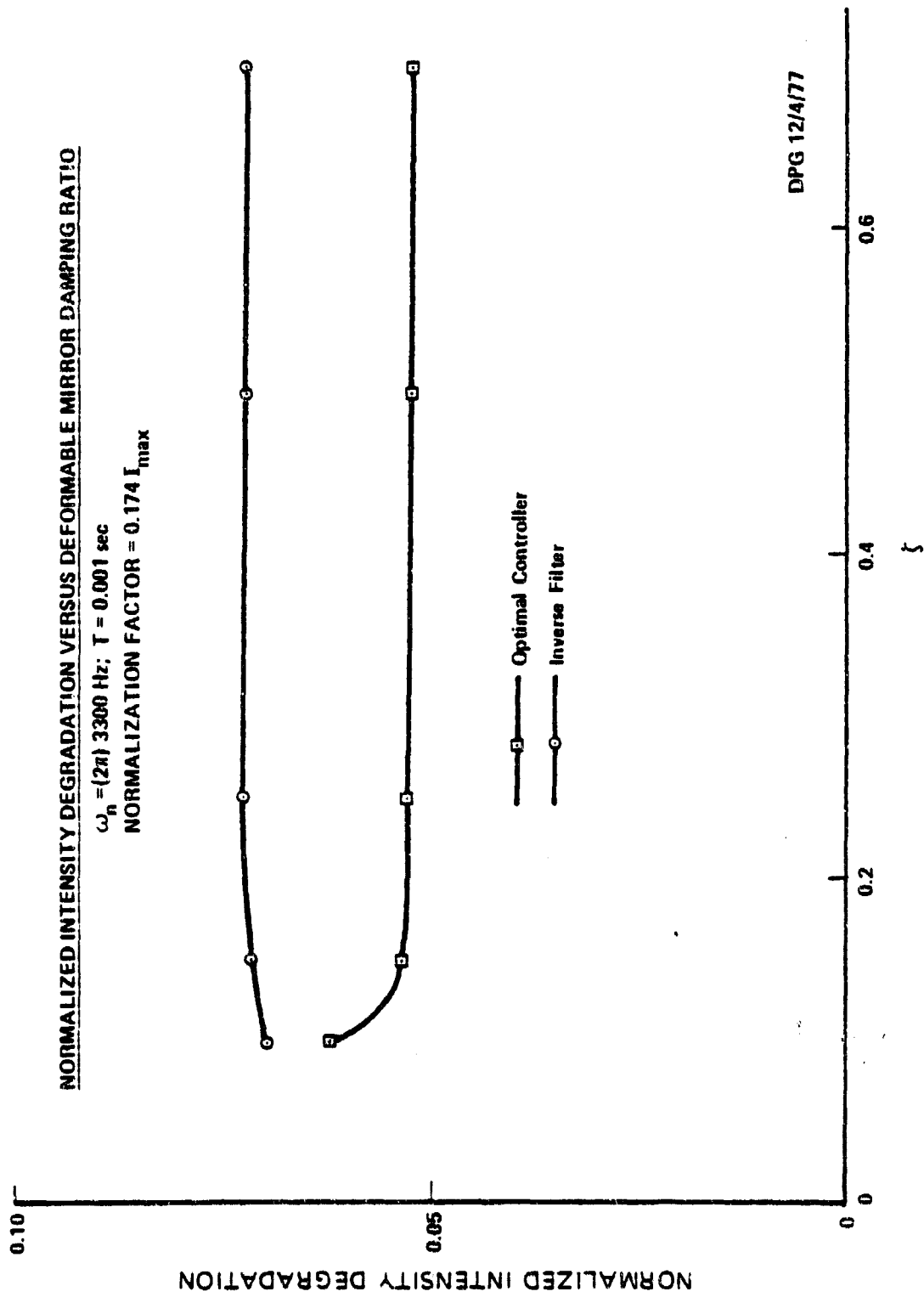


Figure 4.6-11 Normalized Intensity Degradation

## 5. INTEGRATED ESTIMATION-CONTROL SIMULATION RESULTS

In this chapter results of the performance evaluation of the integrated estimation-control algorithms for AMD and PC are presented. In addition to full disturbance estimation (five truth model optical modes and five estimator modes), a number of limited mode estimation and control cases were run. For example, the PC system was implemented with estimation and control of the two tilt modes and focus while the truth model included all five optical disturbance modes. An interim divergence of the AMD estimator was discovered during the integrated simulations; the source of this divergence and methods to avoid it are discussed in this chapter, also.

### 5.1 INTEGRATED PHASE CONJUGATE SYSTEM RESULTS

Figure 5.1-1 shows the integrated estimation and control simulation results for the phase conjugate system as a function of sensor noise level. In addition to the curve shown for the five mode case, curves are provided for simulations in which only modes 1, 2, and 3 (xtilt, ytilt, focus) and only modes 1 and 2 were controlled. In all cases the truth model included all five aberration modes. A curve for the Kalman filter with perfect control and the no estimation and control line are included for comparison.

The five mode estimation-control curve shows a 5 to 7 percent intensity degradation from the Kalman filter with perfect control line; this is a reasonable degree of degradation considering the results of Section 4.6.1. That is,

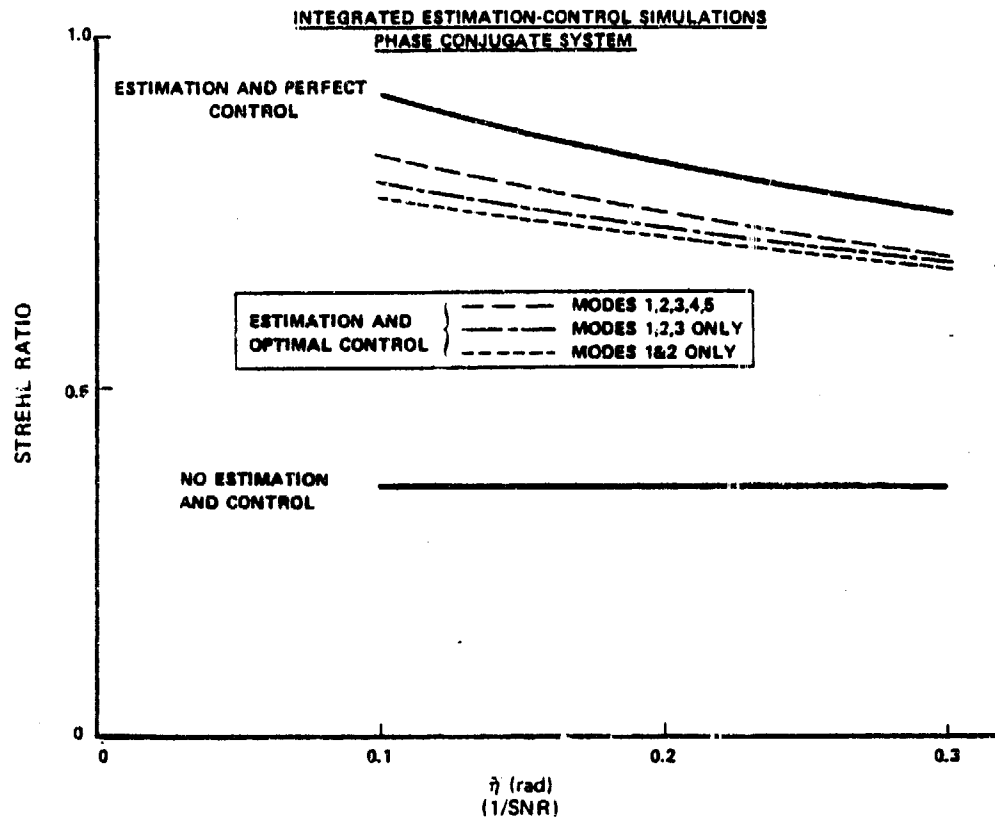


Figure 5.1-1 Phase Conjugate System Performance

roughly 1 to 2% nulling error degradation is to be expected for each of the tilt channels; similar degradations should be expected for the focus and deformable mirror channels. As a consequence of the separation theorem (Ref. 2), the five mode estimation and control results represent the performance of the optimal system consistent with the modeling assumptions and parameters used in the present study.

Additional simulations were run to evaluate the system performance for limited disturbance estimation and control. Again, all five disturbance models were present in the truth model; the filtering algorithm was structured to

estimate only limited combinations of aberration modes. No alteration to the filtering algorithm was made to account for the presence of the neglected disturbances; it was assumed that the orthogonality of the aberration modes and the spatial filtering properties of the shearing interferometer itself would "wash out" undesired errors due to neglected higher order aberrations. The mode 1, 2, 3 case in which astigmatism was neglected shows Strehl ratio degradations from the five mode correction case ranging from 1 percent at the high sensor noise value to 4 percent at the low sensor noise level. The case in which only the two tilt modes were controlled shows degradations of 2 percent at high noise to 6 percent at low noise levels. One can infer from these results that at high sensor noise levels there is little to be gained by estimation and control of higher order aberration modes; indeed, the savings in required hardware (i.e., focus and deformable mirrors) may justify neglect of these modes.

## 5.2 INTEGRATED ACTIVE MULTIDITHER SYSTEM

### 5.2.1 Test Cases and Simulation Results

Integrated estimation and control simulations were performed for the AMD system of a dither frequency of 250 Hz. The 500 Hz dither was not evaluated for two reasons:

- The tilt and focus mirror bandwidths specified (1000 Hz and 500 Hz, respectively) would yield poor following of a 500 Hz dither signal.
- Preliminary estimation evaluation (Section 3) indicated that with speckle performance was nearly identical at 250 Hz and 500 Hz dither frequencies.

The first concern could be obviated by dither command signal shaping (i.e. a "lead" prefilter), increased dither amplitude, or by implementation of a separate high bandwidth dither mirror. The dither signal processing approaches would require experimentation; the hardware alternative would require a sophisticated and expensive optical component. The estimation performance with speckle, the most realistic representation of the AMD system, indicates negligible improvement at the higher dither frequency; efforts to dither at 500 Hz will yield little, if any, reward.

The performance of the integrated AMD system at a range of 500 km is indicated in Fig. 5.2-1. The no speckle case and the no estimation and control case establish upper and lower bounds, respectively, on system performance. In the presence of speckle the integrated estimation and control system achieves a Strehl ratio of .550: a significant improvement over the no estimation and control value of .300, but not a very encouraging result from the standpoint of overall system

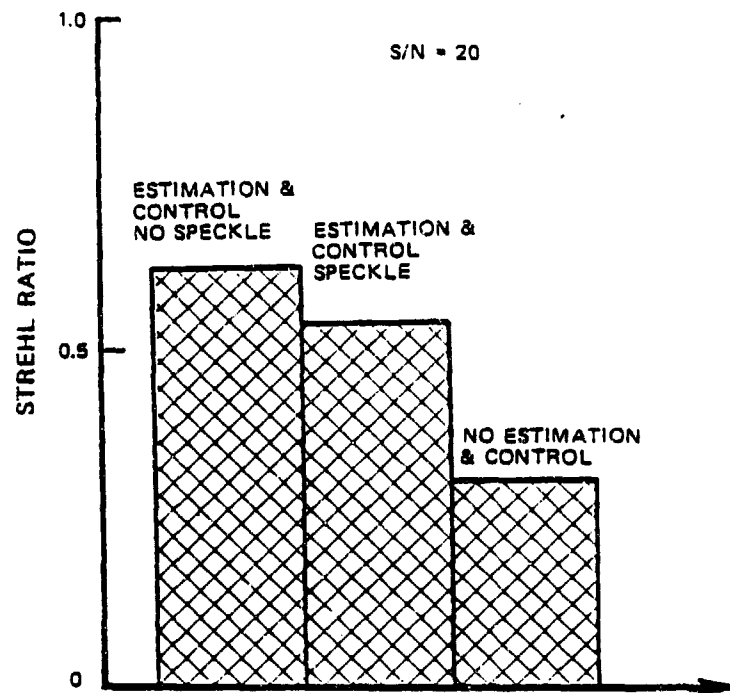


Figure 5.2-1 Integrated AMD Performance,  
Range = 500 km

efficiency. Again, speckle effects cause a very severe degradation in measurement quality, reducing the effective signal-to-noise ratio of the photodetector to roughly 3. With measurement noise levels of such high magnitude even an optimal system cannot offer totally favorable results. It should be mentioned that the estimator underwent an interim divergence in the no speckle case (no divergence was detected with speckle). This divergence was avoided by reinitialization of the filtering algorithm; the Strehl ratio shown in Fig. 5.2-1 corresponds to the "fixed" filter. The nature and correction of the filter divergence are discussed in Section 5.2.2.

Figure 5.2.2 shows the performance of the AMD system at 100 km range. Again, the no speckle and no control results

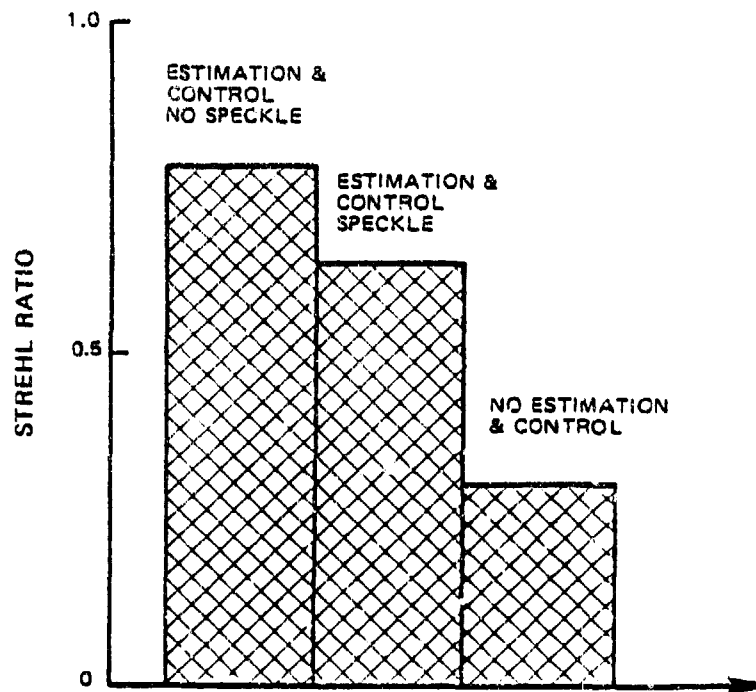


Figure 5.2-2 Integrated AMD Performance,  
Range = 100 km

are presented for comparison; the no speckle results are considerably better than those for the 500 km range as a result of the smaller transit delay lag and an increased signal-to-noise ratio at the closer range. As the estimation and control with speckle line indicates, speckle washes out any improvement in the signal-to-noise ratio, thereby degrading performance to a Strehl ratio of .63. No divergence of the filter was detected in either the no speckle or speckle cases.

### 5.2.2 Filter Divergence

Filter divergence (instability) is a common problem of extended Kalman filters and generally arises from the linear approximations used in the filtering algorithm. In



the AMD estimator there is a linearization of the measurement; this approximation is an additional source of error to the filter estimates that is not accounted for explicitly in the algorithm. A divergence of the estimation algorithm occurred in the 500 km range with no speckle simulation. While the no speckle simulations do not represent physically realistic conditions, the nature and correction of the divergence should be examined to determine why no divergence occurred with speckle.

The time history of the turbulence mode strengths and the corresponding filter estimates near the divergence is shown in Fig. 5.2-3. The mode strengths and estimates all approach a small value simultaneously; as the mode strengths move apart the estimates begin to oscillate with increasing amplitude (diverge). A similar problem was observed by Lewantowicz (Ref. 12) in which a conical scan estimator developed a sign error in the estimate and diverged.

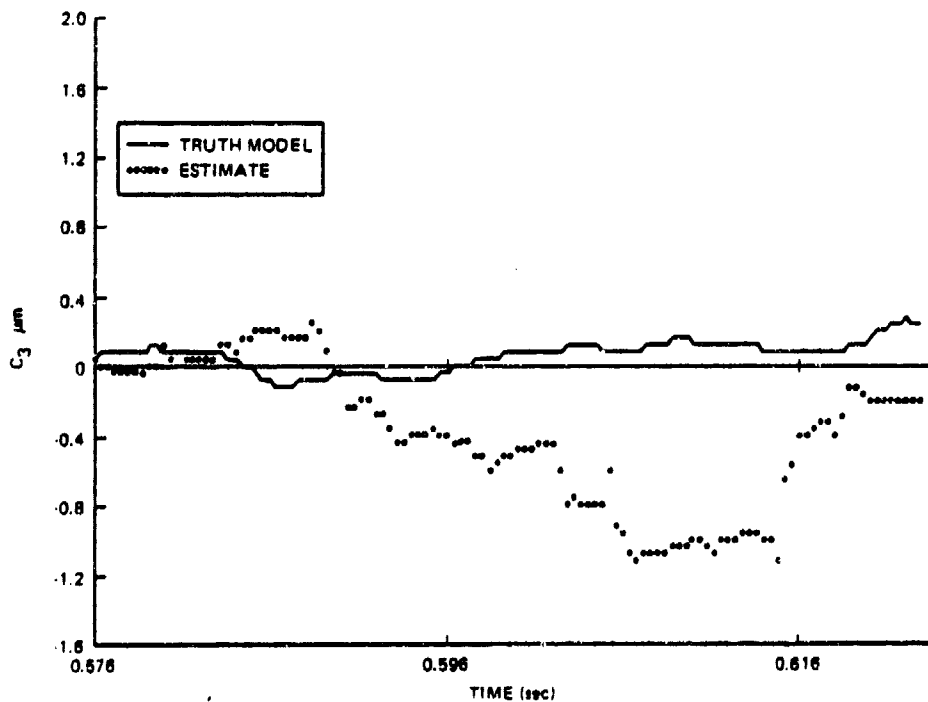


Figure 5.2-3(a) Divergent Filter Time History

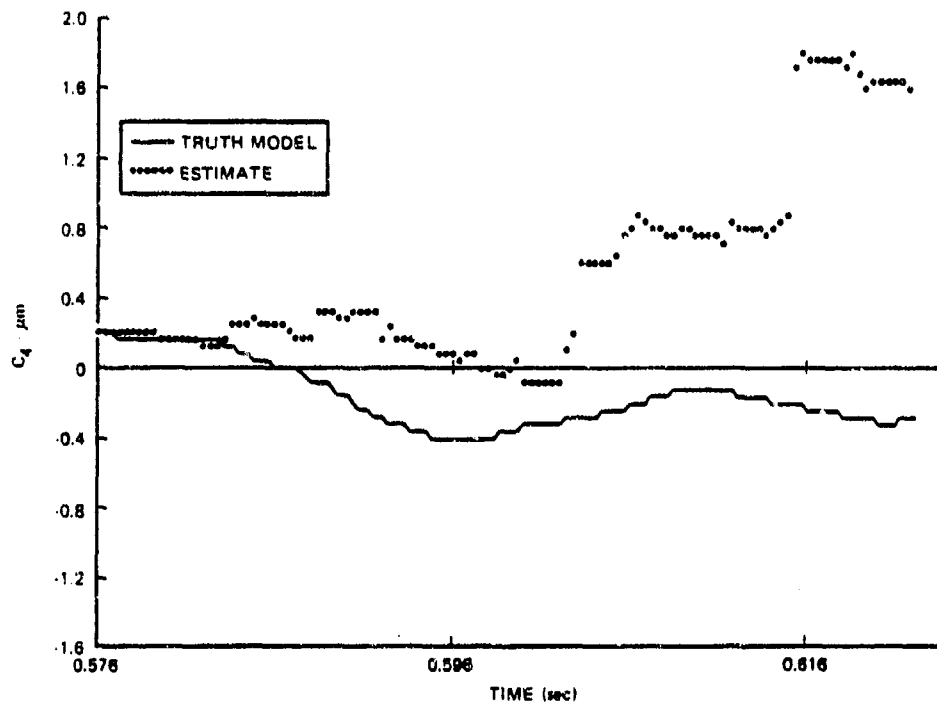


Figure 5.2-3(b) Divergent Filter Time History (Continued)

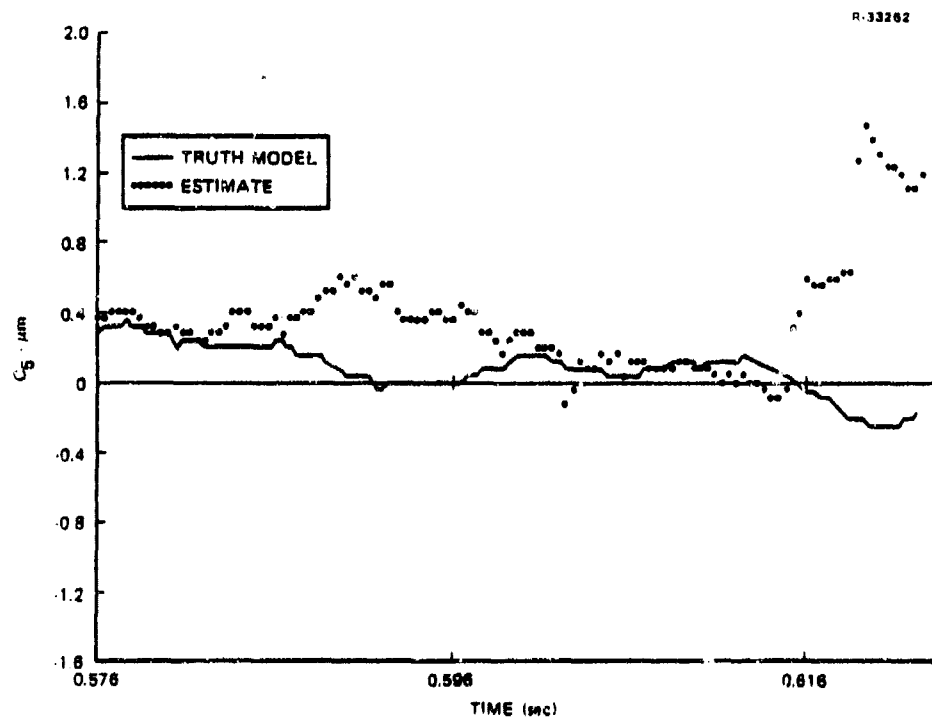


Figure 5.2-3(c) Divergent Filter Time History (Continued)

There are a number of artifices that can be used to correct divergence of an extended Kalman filter. In Ref. 11, for example, the filter residual was monitored; if the residual appeared to be growing, a sign error would be assumed and the sign of the estimate changed. A similar logic could be applied to the present case; the residual could be monitored to detect the divergence and the filter reinitialized. Table 5.2-1 shows the estimation errors for the divergent and "fixed" filters (dynamic logic was not implemented; the filter was simply reinitialized at the time the divergence occurred). The estimation error for the focus mode (Mode 3) is still quite large; this is a result of a very large defocus excursion (approximately  $10 \sigma_d$  peak with a time constant of 0.15 sec) following reinitialization. The estimation errors shown in Table 5.2-1 imply that no additional divergence of the filter occurred after reinitialization.

TABLE 5.2-1  
ESTIMATION ERRORS FOR DIVERGENT  
AND FIXED FILTERS

T-1901

MODE		1	2	3	4	5
Disturbance rms ( $\sigma_d$ ) ( $\mu\text{m}$ )		1.20	1.20	0.23	0.33	0.33
Estimation Errors ( $\mu\text{m}$ )	Divergent	1.07	1.00	0.22	0.30	0.30
	Reinitialized	0.69	0.46	0.30	0.17	0.22

No divergence was detected in simulations which included speckle. As outlined in Section 3.1, the filter was altered to account for speckle by making a sizeable increase in the assumed detector noise; this increase causes the filtering algorithm to put less weight on the measurements relative to the extrapolations in computing the estimates. This approach to dealing with speckle introduces additional stability into the filtering algorithm; this increased stability also accommodates the errors resulting from the linearization of the measurement.

The beam cleanup controller, used to control phase-front aberrations generated by the laser device itself, is described in this chapter. The design discussed here deals only with the control problem; since the laser power levels involved exceed the sensor noise levels by several orders of magnitude, "perfect" state reconstruction is possible via a Luenberger state estimator (observer, Ref. 2). The first section of this chapter will deal with the development of an optimum error budget; in the second section a feedforward controller-deformable mirror system is designed to meet the optimum error budget in a best-least-squares sense; simulation results and evaluation of the control system are presented in the third section.

### 6.1 OPTIMUM ERROR BUDGET

The prime limitation of a beam cleanup control system stems from the fact that a single deformable mirror must attempt to null phasefront aberrations associated with a number of different radiation wavelengths. In the present case, for example, the total laser power is divided among three distinct wavelengths or radiation spectrum lines; the single deformable mirror cannot null simultaneously the aberrations of all three lines.

Since perfect disturbance nulling is impossible, the best alternative is to find a time history of mirror output that will minimize the intensity degradations due to the

disturbances, Eq. 6.1-1 is a quadratic performance index which is appropriate to this design goal:

$$J = \int_0^{\infty} [(\underline{c}_1 + \underline{\tilde{c}})^T Q_1 (\underline{c}_1 + \underline{\tilde{c}}) + (\underline{c}_2 + \underline{\tilde{c}})^T Q_2 (\underline{c}_2 + \underline{\tilde{c}}) + (\underline{c}_3 + \underline{\tilde{c}})^T Q_3 (\underline{c}_3 + \underline{\tilde{c}})] dt \quad (6.1-1)$$

or, in more compact notation:

$$J = \int_0^{\infty} \sum_{i=1}^3 (\underline{c}_i + \underline{\tilde{c}})^T Q_i (\underline{c}_i + \underline{\tilde{c}}) dt \quad (6.1-2)$$

Here  $\underline{c}_i$  is the vector of optical mode disturbances associated with the  $i^{\text{th}}$  radiation spectrum line,  $\underline{\tilde{c}}$  is the vector of deformable mirror outputs which attempts to counteract the phasefront aberrations of the three lines. The  $Q_i$ 's are the intensity degradation matrices derived in Section 4.3.1; these are diagonal matrices which are functions of both radiation power and wavelength of a given line; i.e. for  $Q_i$  the diagonal elements are:

$$q_{11} = I_{\max_i} \frac{k_i^2}{4} \quad (4.3-9)$$

$$q_{22} = I_{\max_i} \frac{k_i^2}{4} \quad (4.3-10)$$

$$q_{33} = I_{\max_i} \frac{k_i^2}{3} \quad (4.3-11)$$

$$k_i = \frac{2\pi}{\lambda_i} \quad (2.3-2)$$

The problem is to find the mirror output,  $\underline{\tilde{c}}$ , that minimizes the performance index Eq. 6.1-1. Differentiating  $J$  with respect to  $\underline{\tilde{c}}$  one obtains:

$$\frac{\partial J}{\partial \underline{\tilde{c}}} = \int_0^{\infty} \left\{ \sum_{i=1}^3 [Q_i \underline{c}_i + Q_i \underline{\tilde{c}}] \right\} dt \quad (6.1-3)$$

The minimum degradation occurs when  $\frac{\partial J}{\partial \underline{c}}$  is equal to a zero vector; this implies that the integrand of Eq. 6.1-3 is zero for all  $t$ :

$$\sum_{i=1}^3 Q_i \underline{c}_i + Q_i \underline{\tilde{c}} = 0 \quad (6.1-4)$$

or

$$\left( \sum_{i=1}^3 Q_i \right) \underline{\tilde{c}} = - \sum_{i=1}^3 Q_i \underline{c}_i \quad (6.1-5)$$

$$\therefore \underline{\tilde{c}} = - \left( \sum_{i=1}^3 Q_i \right)^{-1} \sum_{i=1}^3 Q_i \underline{c}_i \quad (6.1-6)$$

Eq. 6.1-6 defines the optimum time history of the deformable mirror output in counteracting the phasefront aberrations of the three lines. Since the  $Q_i$ 's are all equal up to a multiplicative factor, further simplification of Eq. 6.1-6 is possible, i.e.:

$$Q_i = I_{\max_i} k_i^2 Q \quad (6.1-7)$$

$$Q = \begin{bmatrix} 1/2 & 0 & 0 \\ 0 & 1/2 & 0 \\ 0 & 0 & 2/3 \end{bmatrix} \quad (6.1-8)$$

$$\therefore Q_i = P_i Q \quad (6.1-9)$$

$$\sum_{i=1}^3 Q_i = P_t Q \quad (6.1-10)$$

with

$$P_i = I_{\max_i} k_i^2 \quad (6.1-11)$$

$$P_t = \sum_{i=1}^3 I_{\max_i} k_i^2 \quad (6.1-12)$$

Substituting Eq. 6.1-9 and 6.1-10 into Eq. 6.1-6 one obtains:

$$\underline{\tilde{c}} = - \sum_{i=1}^3 \frac{P_i}{P_t} c_i \quad (6.1-13)$$

Eq. 6.1-13 indicates that the deformable mirror should follow the power weighted sum of the phasefront aberrations of the three lines.

## 6.2 THE BEAM CLEANUP CONTROL SYSTEM/SIMULATION MODEL

A control system will now be designed to follow the optimum output time history derived in Section 6.1. The design will be a direct adaptation of the feedforward controller-deformable mirror system derived in Section 4.5. The design approach is to derive the optimal feedforward controller for the phasefront disturbances of each line, by itself; the single line controller outputs are then attenuated by the fraction of the total laser power of that line. Figure 6.2-1 is a block diagram of the resulting control system.

The control system as shown is analog. The disturbance bandwidths involved were in the kilohertz range; a digital control implementation would require prohibitively high sample rates. Again, the phasefront aberration measurements are assumed to be perfect; in steady state the  $\underline{x}_i$ 's used in computing the control will be identical to the states of the disturbance model. In the computer simulation of the beam cleanup system the truth model disturbance states are used directly in the control computation; thus, the simulation results of Section 6.3.2 will reflect the steady state performance of the system.



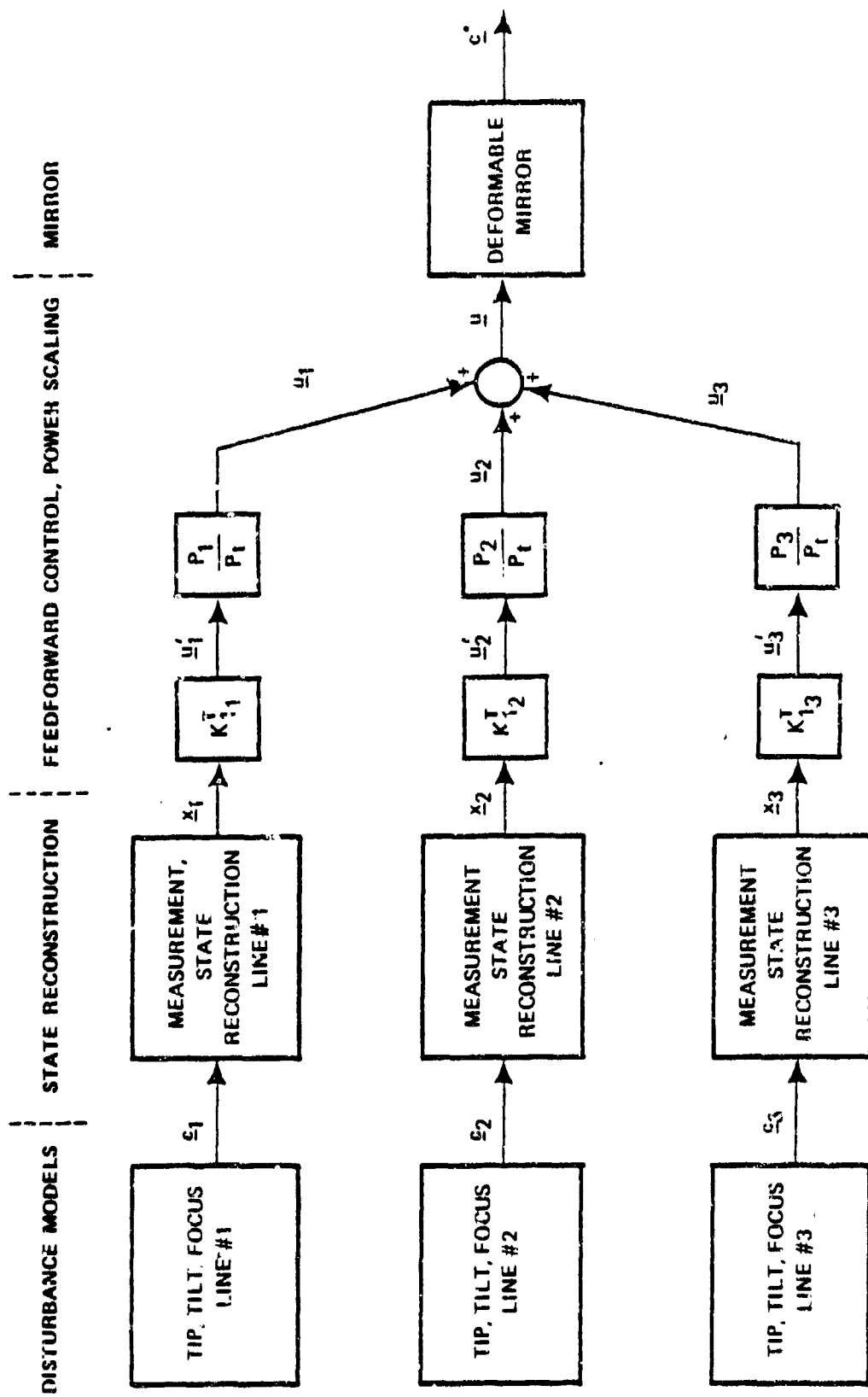


Figure 6.2-1 Beam Cleanup Control System

## 6.3 BEAM CLEANUP SIMULATION

### 6.3.1 Test Case Parameters

The test case used to evaluate the beam cleanup design is described in this section. The problem is to control the phasefront aberrations of three radiation spectrum lines; the wavelengths and radiation power levels are given in Table 6.3-1.

TABLE 6.3-1  
RADIATION WAVELENGTHS AND POWER LEVELS

T-1848

LINE NO.	WAVELENGTH ( $\mu\text{m}$ )	$P_i/P_t$
1	3.714	.113
2	3.800	.792
3	3.927	.085

Phasefront disturbances for each line are modeled by the dynamics of three optical modes (two tilt modes and focus). The spectrum for a typical phasefront disturbance mode is shown in Fig. 6.3-1; break frequencies and rms levels for all nine disturbance models are listed in Table 6.3-2. These spectra are simulated in the time domain by the outputs of linear shaping filters driven by white noise.

### 6.3.2 Simulation Results

Figure 6.3-2 shows the efficiency of the beam cleanup system as a function of deformable mirror bandwidth. The asymptote labeled "perfect control" indicates that the rms

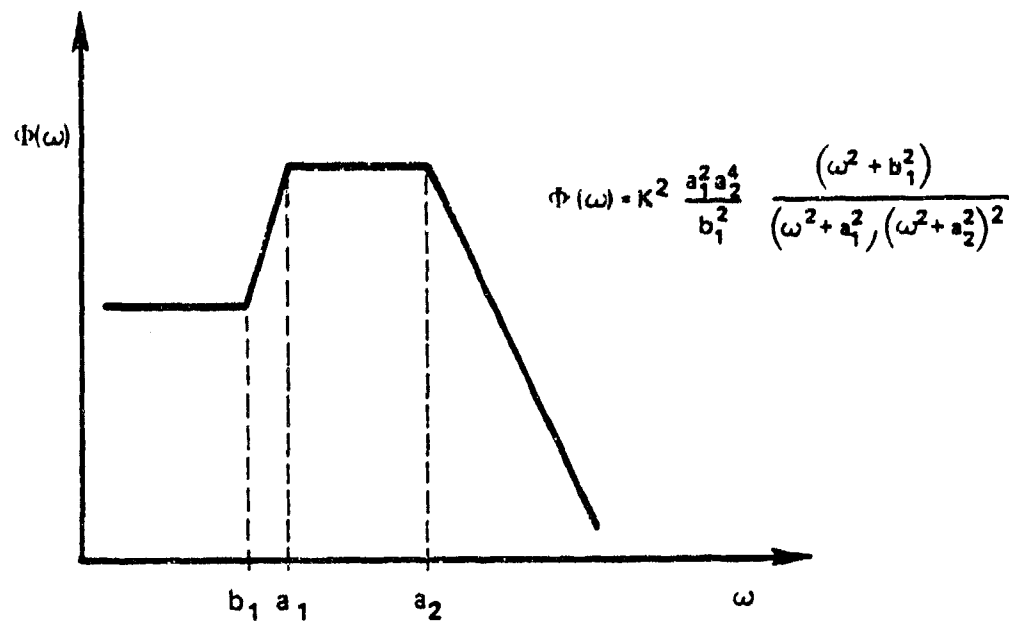


Figure 6.3-1 Phasefront Disturbance Spectrum

TABLE 6.3-2  
DISTURBANCE SPECTRA PARAMETERS

T-1849

LINE NO.	MODE	$a_1$	$a_2$	$b_1$	RMS ( $\mu\text{m}$ )
1	XTILT	$2\pi(1000)$	$2\pi(1400)$	$2\pi(15)$	1.8
	YTILT	$2\pi(1000)$	$2\pi(1400)$	$2\pi(15)$	1.8
	FOCUS	$2\pi(1200)$	$2\pi(1500)$	$2\pi(20)$	1.6
2	XTILT	$2\pi(800)$	$2\pi(1000)$	$2\pi(60)$	1.2
	YTILT	$2\pi(800)$	$2\pi(1000)$	$2\pi(60)$	1.2
	FOCUS	$2\pi(900)$	$2\pi(1100)$	$2\pi(40)$	.5
3	XTILT	$2\pi(1200)$	$2\pi(1450)$	$2\pi(12)$	2.6
	YTILT	$2\pi(1200)$	$2\pi(1450)$	$2\pi(12)$	2.6
	FOCUS	$2\pi(1750)$	$2\pi(2000)$	$2\pi(50)$	1.0

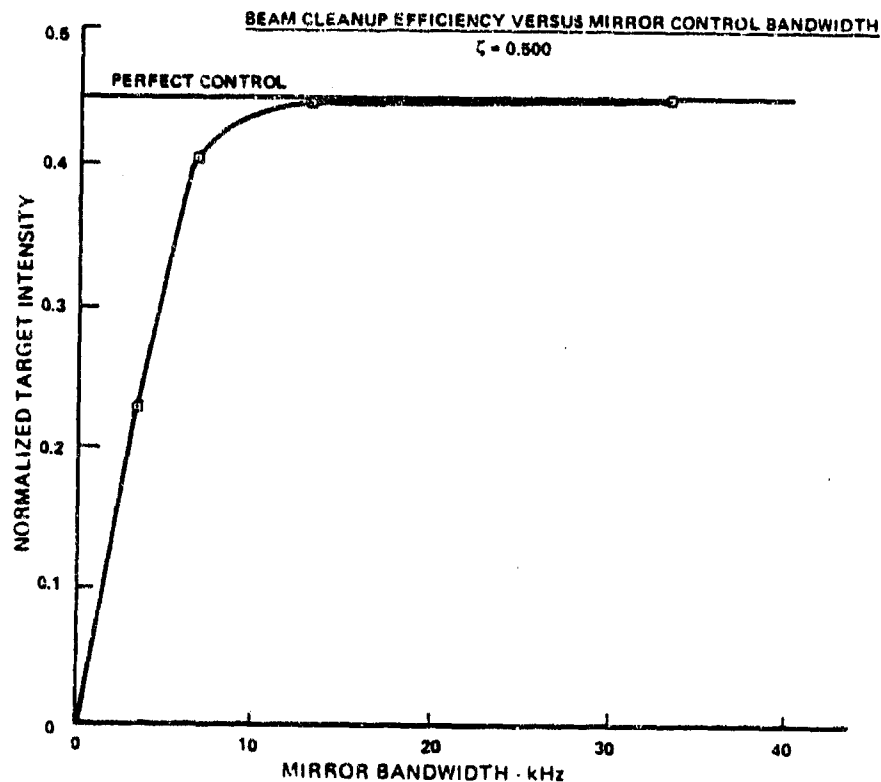


Figure 6.3-2 Beam Cleanup System Performance

levels chosen cause a severe intensity degradation; even with exact following of the optimal time history derived in Section 6.1 roughly 55% of the potential target intensity is lost. Although the disturbance levels may be unrealistically high, the example problem does give some indication of hardware requirements for the beam cleanup system. With a mirror bandwidth of 3300 Hz, the bandwidth assumed for the PC and AMD systems, the target intensity is degraded to .225; even with an optimal controller the mirror is simply too slow to follow the high bandwidth disturbances. Indeed, a mirror bandwidth near 10 kHz would be required for disturbance nulling approaching the maximum possible at the specified disturbance bandwidth.

The example problem results also indicate that the performance index, Eq. 6.1-1, is inappropriate in situations having high rms levels of phasefront distortion. Equation 6.1-1 is based on a quadratic approximation of the intensity pattern at the target (see Section 4.3.1); this approximation is accurate only near the origin of the intensity function. For high levels of phasefront aberration the quadratic approximation breaks down and may yield normalized intensity degradations which exceed unity as indicated by Fig. 6.3-3.

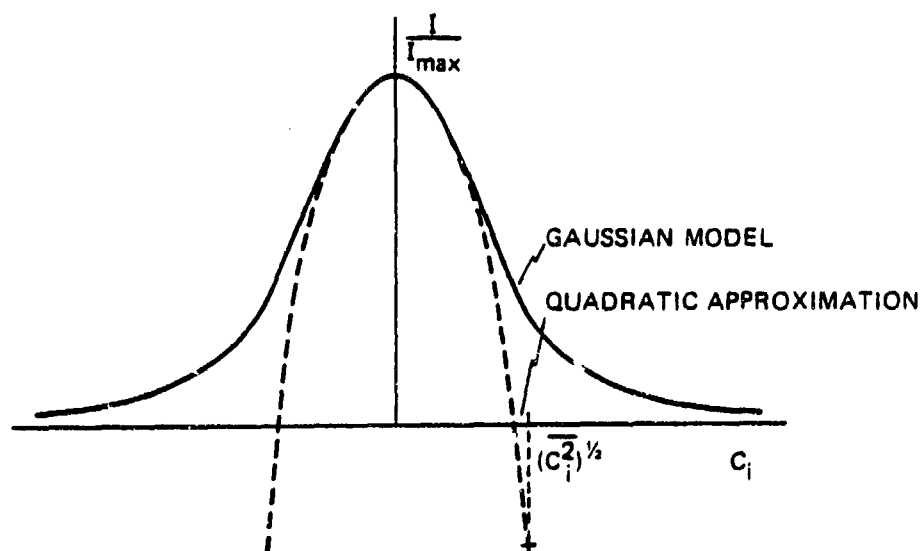


Figure 6.3-3 Gaussian Intensity Pattern and Quadratic Approximation

The inaccuracy of the quadratic approximation adversely affects the performance index and the optimal control time history derived from it. Two approaches to the derivation of a more accurate control methodology are:

- Use the assumed Gaussian intensity function (Eq. 2.3-1) to characterize target intensity degradations in the performance index, i.e.:

$$J = \int_0^{\infty} \left\{ \left[ I_{\max_1} - g_1(c_1 + \tilde{c}) \right] + \left[ I_{\max_2} - g_2(c_2 + \tilde{c}) \right] + \left[ I_{\max_3} - g_3(c_3 + \tilde{c}) \right] \right\} dt$$

- Null only the phasefront disturbances of the line having the largest fraction of the total power.

The first alternative is the more precise of the two; the  $\left[ I_{\max_i} - g_i(c_i + \tilde{c}) \right]$  terms represent a more accurate representation of intensity degradations than the quadratic approximations used in Eq. 6.1-1. Since the performance index is no longer quadratic, the minimization of  $J$  is no longer a simple matter of taking the derivative of the performance index with respect to  $\tilde{c}$  and setting it equal to zero. A time invariant error nulling budget similar to Eq. 6.1-13 could be derived by parameter optimization methods; i.e., the optimal control would be a weighted sum of the phasefront aberrations of the three lines. The weighting factors would have to be determined through monte-carlo analysis; this can be a very costly and time consuming process. While admittedly suboptimal, the second approach is simple to derive, implement, and analyze. In situations similar to the test case, in which 80% of the laser energy was in a single spectral line, adequate performance can be obtained. With a mirror and control system capable of accurately nulling the phasefront aberrations of the high power spectral line, nearly 80% of the laser power could be rendered unaberrated (i.e., nearly all of the power in the 3.8  $\mu\text{m}$  line could be cleaned up). A normalized maximum intensity of 0.8 is a considerable improvement over the value of 0.45 obtained with the controller based on Eq. 6.1-13.

## 6.4 CHAPTER SUMMARY

The beam cleanup design and evaluation indicates:

- For low disturbance levels (i.e., levels for which the quadratic approximation (Eq. 6.1-1) is accurate) the optimal beam cleanup time history is the power weighted sum of the phasefront disturbances of the three lines.
- A mirror bandwidth of 10 kHz is required for accurate optimal time history tracking of disturbances in the 1 kHz range.
- With high disturbance levels (i.e., levels for which the quadratic approximation (Eq. 6.1-1) is not accurate) the optimal beam cleanup time history is no longer the power weighted sum of the phasefront disturbances of the three lines. The optimal weighting of the phasefront disturbances of the three lines must be derived through monte carlo analysis using a Gaussian performance index.

7.

## CONCLUSIONS AND RECOMMENDATIONS

### 7.1 CONCLUSIONS

The extended Kalman filter developed in the present program is an effective algorithm for active multidither phasefront estimation. The Kalman filter successfully estimates the states of five turbulence induced phasefront disturbance modes in the presence of severe speckle and beam transit delays. The performance of the extended Kalman filter (in terms of an average Strehl ratio for the scenario) was found to be essentially the same for dither frequencies of 250 Hz and 500 Hz; the use of the lower dither frequency reduces the mirror bandwidth required to follow the dither commands.

The Kalman filter developed for phase conjugate aberration estimation yielded Strehl ratio increases of 0.05 to 0.28 (depending on sensor noise) over a candidate least-squares-fit low pass filter estimator. Sensitivity studies to determine the effects of truth model/filter signal to noise mismatches which may result from target heating indicate negligible degradation of estimator performance.

Optimal disturbance nulling control was shown to yield significant performance improvements over typical classical designs. Superior performance of the optimal controller is attributable to the use of the full disturbance state (i.e., states related to the time derivatives of the disturbance process as well as the disturbance magnitude) in computing control commands. Using the time derivative states, the controller can compute commands which anticipate the future of the disturbance process in addition to nulling present disturbances. The optimal controller for the tilt channel outperformed a candidate classical controller at all sample rates and had



nulling error variances lower than that of a continuous classical controller for sample rates higher than 1.2 kHz. Similarly, an optimal feedforward controller designed for the deformable mirror outperformed a classical inverse-filter controller in nulling astigmatism errors while suppressing mirror surface figure cross-coupling. Parametric studies showed that use of optimal control algorithms can relax hardware performance requirements; for example, increases in tilt mirror bandwidth beyond 500 Hz yield negligible improvement in disturbance nulling. Optimal controller performance also was found to be insensitive to 20 percent mismatches of the design model and truth model disturbance bandwidths.

Simulations of the integrated estimation and control systems indicate good performance: non-ideal control had negligible effect on convergence of the active multidither estimator; non-ideal control reduces the Strehl ratio produced by the phase conjugate system 0.05 to 0.07 (depending on sensor noise) below the corresponding ideal control results.

The results of the beam cleanup system design and evaluation indicated that the optimal control time history depends on the phasefront disturbance levels as well as the power contained within each line. For low disturbance levels, i.e., levels for which the Gaussian intensity can be approximated by a quadratic function, the optimal beam cleanup time history is the power weighted sum of the phasefront disturbances of the three spectral lines. At disturbance levels for which a quadratic approximation is inaccurate, the optimal weighting of the phasefront disturbances must be derived through monte carlo analysis using a Gaussian performance index. Parametric studies also indicated that a mirror bandwidth of 10 kHz is required for accurate optimal time history tracking of disturbances in the 1 kHz range.

In summary, optimal estimation and control have been shown to offer:

- An effective approach to active multidither estimation in the presence of severe speckle
- Phase conjugate estimation superior to classical methods
- Disturbance nulling control performance superior to that of typical classical designs
- Insensitivity of control performance to disturbance model mismatches
- Potential relaxation of active component bandwidth requirements
- Spatial, temporal optimization of deformable mirror control

## 7.2 RECOMMENDATIONS

Isoplanaticism Correction - At long ranges (i.e., 100 to 500 km) an additional spatial (isoplanaticism) delay exists. Filter estimates are for turbulence effects along the line-of-sight; if a significant aim-ahead is required to fire at a moving target, the beam will be aberrated by a section of the atmosphere displaced from the line-of-sight by the lead angle. A predictor similar to that used to compensate transit time delays in the active multidither estimator could be implemented to account for the aim-ahead delay. Using a spectral description of the spatial characteristics of the turbulence, a Markov model approximation could be constructed; using this Markov model, the line-of-sight turbulence estimates could be propagated (predicted) through the lead angle.

Disturbance Model Refinement - The success of the optimal estimation and control approach is attributable to the

use of a precise mathematical definition of the disturbance dynamics. In the present study, the turbulence disturbances were characterized as five independent random processes. In actual fact, the modal turbulence processes are cross-correlated; this is reasonable since the five turbulence aberration modes are all produced by the same atmosphere. Knowledge of these cross-correlations, based on cross-spectra for the five modes, for example, could be incorporated into the state estimation algorithms; this additional information could be particularly advantageous to the active multidither estimator which, in the present study, must estimate the states of five independent processes from a single measurement. Cross-spectra derived from a mathematical model similar to that used by Hogge and Butts (Ref. 1) would provide the basis for a detailed characterization of modal turbulence dynamics including cross-correlations of the modal dynamics.

Phase Conjugate System - Efforts to refine the phase conjugate system should be directed towards the shearing interferometer. As Fig. 5.1-1 showed, reduction of sensor noise level results in a commensurate improvement in Strehl ratio. Optimization of the spatial filtering of the shearing interferometer, i.e., optimal number and location of subapertures, is another potential area for system improvement.

Development of a Practical Algorithm - In a real time implementation, problems arise which are not given close attention in the preliminary design stage. Specifically, the algorithm computation time and the transport lag it introduces becomes a primary concern. In addition to attempting to develop the most efficient software possible, a tradeoff between algorithm complexity (i.e., disturbance model order) and computation lag may be necessary to "optimize" a real time imple-

mentation. The effects of computation lag can be artificially introduced into a non-real-time computer model, allowing sensitivity studies to be carried out. The true computation lag must be assessed through actual implementation of the algorithm on the control system computer.

Test Bed Implementation - The results of Section 3 shown that the Kalman filter approach to phase conjugate estimation yields a considerable performance improvement over classical estimation methods. Because of the superior performance offered by the optimal estimation and control approach, serious consideration should be given to its use in test bed implementations (i.e., the adaptive optics portion of the Shared Aperture Medium Range Tracker).

## REFERENCES

1. Hogge, C.B. and Butts, R.R., "Frequency Spectra for the Geometric Representation of Wavefront Distortions Due to Atmospheric Turbulence," IEEE Transactions on Antennae and Propagation, Vol. AP-24, No. 2, March 1976. (Related AFWL FORTRAN Program supplied by R.R. Butts.)
2. Anderson, B.D.O. and Moore, J.B., Linear Optimal Control, Prentice-Hall, Inc., Englewood Cliffs, New Jersey, 1971.
3. "Shared Aperture Medium Range Tracker (SAMRT)(U)," Aeronutronics Ford Corporation, Report No. S-6175, October 1975.
4. "TASC Proposal to Develop Advanced Adaptive Optics Control Techniques," The Analytic Sciences Corporation, Report No. TP-996, 10 August 1976.
5. Brandewie, et. al., "Long Range Optical System Study (LROSS)," Rockwell International, Report No. AFWL-TR-75-291, May 1976.
6. "Adaptive Optics System Models, In-Progress Technical Review," SP-871-1, The Analytic Sciences Corporation, Reading, Massachusetts, 13 September 1977.
7. Rodriguez, D.A., "Aberration Control for a Large Telescope (U)," Aeronutronics Ford Corporation, Report No. AFWL-TR-75-275, May 1976.
8. Bures, K.J., "Analysis of the Shearing Interferometer," The Analytic Sciences Corporation, Report No. TIM-996-8, 16 August 1977.
9. Unpublished Speckle Spectra received from General Research Corporation, January 1977.
10. Sannuti, P. and Kokotovic, "Near-Optimum Design of Linear Systems by a Singular Perturbation Method," IEEE Tran. Auto. Control, Vol. AC-14, No. 1, February 1969.
11. Glasson, D.P., "Pseudo-Optimal Control of a Deformable Mirror," The Analytic Sciences Corporation, Report No. TIM-996-9, 21 October 1977.

REFERENCES (CONTINUED)

12. Lewantowicz, Z.H., "Laser Pointing and Tracking Using Adaptive Extended Kalman Filter", M.S. Thesis. Air Force Institute of Technology, 1976.

## APPENDIX A

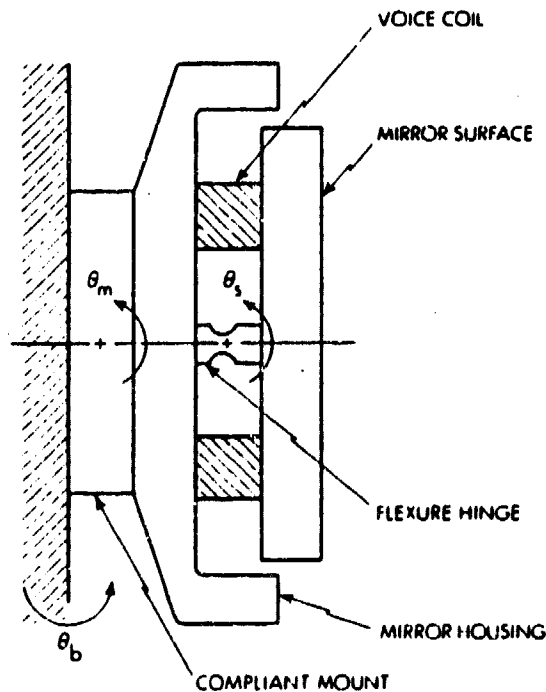
### ADAPTIVE OPTICS MODEL PARAMETER VALUES

#### A.1 LASER/ADAPTIVE OPTICS MODELS

##### A.1.1 Tilt Mirror

The mechanical model of the tilt mirror for pitch motion is shown in Fig. A.1-1. Table A.1-1 lists the model parameters for the open loop dynamics.

R-28C42



MIRROR STATE VECTOR:

$$\underline{x}^T = \left( \theta_s, \dot{\theta}_s, \theta_m, \dot{\theta}_m, \frac{M_{ac}}{K_h} \right)$$

$\theta_s$  = MIRROR SURFACE ANGLE

$\theta_m$  = MOUNT COMPLIANCE ANGLE

$\left( \frac{M_{ac}}{K_h} \right)$  = NORMALIZED VOICE COIL TORQUE

INPUT:

$\theta_{CMD}$  = TILT CONTROL COMMAND

DISTURBANCES

$\theta_h$  = BASE MOTION DERIVED FROM VIBRATION MODEL

Figure A.1-1 Tilt Mirror Mechanical Model and Variable Definition for Mirror Pitch Motion

TABLE A.1-1  
TILT MIRROR MODEL PARAMETERS

T-1856

SYMBOL	DEFINITION	VALUE
$\omega_h$	Surface-flexure hinge natural frequency	$(2\pi)11\text{Hz}$
$\omega_m$	Mount natural frequency	$(2\pi)5000\text{Hz}$
$I'$	Mirror inertia/mount inertia	0.5
$\tau_1$	Voice coil time constant	0.0002sec
$\theta_{\max}$	Maximum mirror displacement $\geq  \theta_s - \theta_m $	2mrad
$\sigma_{\theta_b}$	Rms level of base vibration input. Equivalently: rms level of mirror surface jitter due to laser vibration	(used 0.)

The following control objectives will be the basis of inner loop design for the tilt mirror.

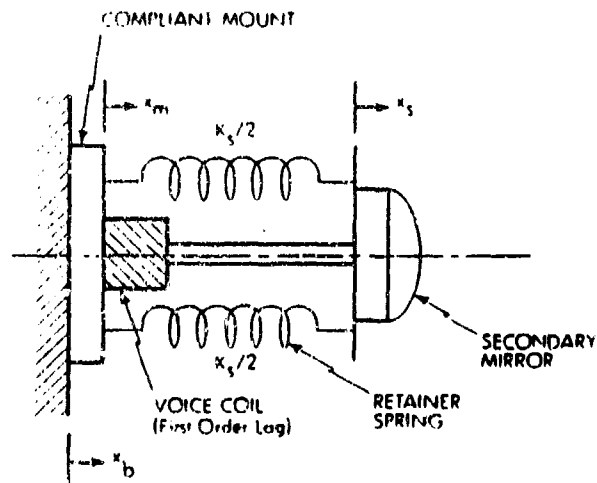
- Extend mirror surface response bandwidth to 1000Hz (=6280 rad/sec)
- Maintain a stable mount compliance mode response.

#### A.1.2 Focus Mirror

Figure A.1-2 shows the mechanical model of the moveable secondary mirror of the focus mirror. Table A.1-2 lists the model parameters for the open loop dynamics.

The following control objectives specify the inner loop design for the focus mirror.





MIRROR STATE VECTOR:

$$\underline{x}^T = \left( x_s, \dot{x}_s, x_m, \dot{x}_m, \frac{F_{ac}}{k_s} \right)$$

$x_s$  = MIRROR SURFACE DISPLACEMENT

$x_m$  = MOUNT COMPLIANCE DISPLACEMENT

$\left( \frac{F_{ac}}{k_s} \right)$  = NORMALIZED VOICE COIL FORCE

INPUT:

$u$  = FOCUS CONTROL COMMAND

DISTURBANCES

$x_b$  = BASE MOTION DERIVED FROM VIBRATION MODEL.

Figure A.1-2 Focus Mirror Mechanical Model

TABLE A.1-2  
FOCUS MIRROR MODEL PARAMETERS

T-1837

SYMBOL	DEFINITION	VALUE
$\omega_s$	Movable mass-spring natural frequency	92.7 rad/sec
$\omega_m$	Mount natural frequency	$(2\pi)2000\text{Hz}$
$m'$	Mirror inertia/mount inertia	0.5
$\tau$	Voice coil time constant	0.0002sec
$d_{\max}$	Maximum mirror displacement $\leq x_s - x_m$	(used $\infty$ )
$f_p$	Primary mirror focal length	1m
$\sigma_{x_b}$	Rms level of vibration input. Equivalently: rms level of mirror surface jitter due to laser vibration	(used 0.)

- Extend secondary mirror response bandwidth to 500Hz = (3140 rad/sec)
- Maintain a stable mount compliance mode response.

### A.1.3 Deformable Mirror

The equations describing the dynamics of the deformable mirror model developed in Section 2.2.3 are given by Eq. A.1-1 to A.1-4. Table A.1-3 lists the primary and coupling dynamics parameters

$$\dot{\underline{z}} = F(\underline{z})\underline{z} + B\underline{u} \quad (\text{A.1-1})$$

$\underline{z}$  = vector of mode strength and time derivative of each mode

$\underline{u}$  = vector of mode commands

TABLE A.1-3  
DEFORMABLE MIRROR PRIMARY DYNAMICS PARAMETERS

T-1859

SYMBOL	DEFINITION	VALUE
$\omega_0^2$	Zero displacement natural frequency squared	$(2\pi)^2 (3300\text{Hz})^2$
$\alpha_k$	Nonlinearity constant	(used 0.)
$d_k$	Modal damping coefficient	$.2\omega_0$
$z_{\text{max}}$	Maximum mirror displacement	10 $\mu\text{m}$

For the  $k^{\text{th}}$  mode:

$$\dot{z}_{2k-1} = z_{2k} \quad (\text{A.1-2})$$

$$\dot{z}_{2k} = \underbrace{\omega_k(z_{2k-1})^2 z_{2k-1} - d_k z_{2k}}_{\text{Primary Dynamics}} + \underbrace{\sum_{j \neq 2k-1, 2k}^n c_{kj} z_j}_{\text{Coupling}} + \underbrace{\omega_k(z_{2k-1})^2}_{\text{Excitation}} \quad (\text{A.1-3})$$

$$\omega_k(z_{2k-1})^2 = \omega_{k0}^2 + (\omega_k^*) |z_{2k-1}| \quad (\text{A.1-4})$$

#### A.1.4 Thermal Deformation

Parameters required by the thermal deformation model of Section 2.2.5 are given by Table A.1-4.

#### A.1.5 Laser Induced Vibration

Figure A.1-3 shows the spectral representation of the laser induced vibration, its second order shaping filter approximation, and dynamic system realization as developed in Section 2.2.4.

Parameters to be used in the shaping filter are:

$$\omega_n = (2\pi)(32\text{Hz}) \quad (\text{A.1-5})$$

$$\zeta \approx .1 \quad (\text{A.1-6})$$

The variance of the noise input to the filter is taken as unity; the DC gain of the filter is also unity. The disturbance "input gains" of the active optics components are adjusted to achieve a desired rms jitter; e.g.  $\bar{\epsilon}_b$  in Table A.1-1.

TABLE A.1-4  
THERMAL DEFORMATION MODEL PARAMETERS

T-1861

SYMBOL	DESCRIPTION	VALUE
$I_{ave}$	Average incident beam intensity. Derived from power levels cited in Ref. 5 and internal beam radius	-
$r_{int}$	Internal beam radius	0.10 m
$a$	Surface absorption coefficient	0.001
$\theta_1$	Beam incidence angle	45° all mirrors except beam expander. 90° beam expander primary and secondary
$\lambda$	Radiation wavelength	3.8 $\mu$ m
$\xi_1, \xi_2$	Mirror property dependent factors. Determined from empirical relationships in Ref. 3	(used 0.)
$\tau_{thermal}$	Thermal response time (cooled mirrors)	.1 sec
$K_{thermal}$	Thermal growth rate (uncooled mirrors)	.003 $\mu$ m/sec

#### A.1-6 Relay Mirror Jitter

The equation of motion for vibration induced pitching of the  $i^{th}$  relay mirror, as developed in Section 2.2.7, is given by Eq. A.1-7. The corresponding yaw equation of motion is of the same format with  $\psi_1$  replacing  $\theta_1$  and subscript y replacing subscript p.

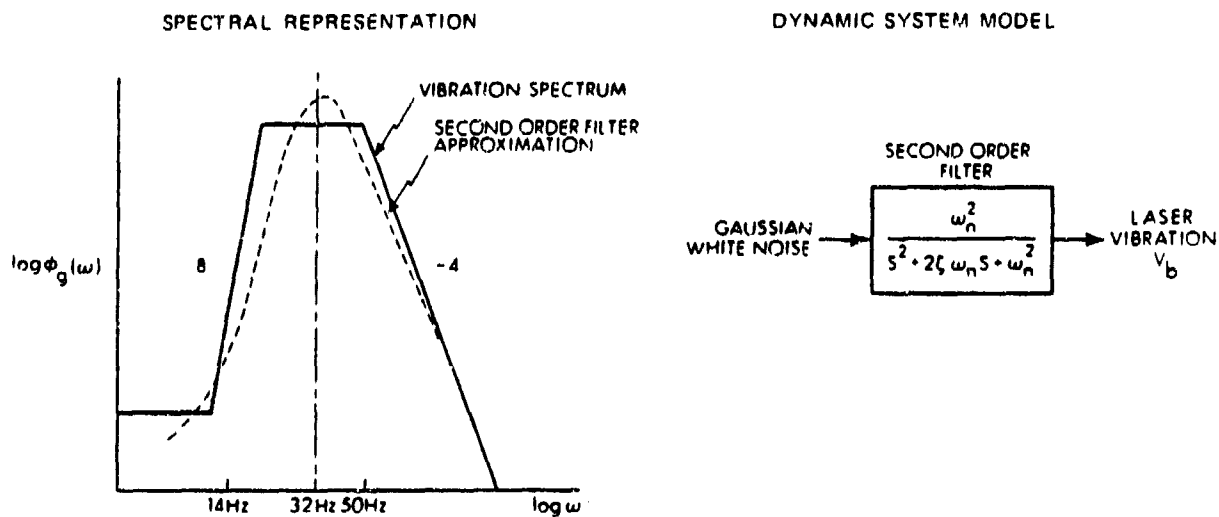


Figure A.1-3 Laser Induced Vibration Spectrum and Model Approximation

$$\ddot{\theta}_i + 2\zeta_{p_i}\omega_{p_i}\dot{\theta}_i + \omega_{p_i}^2\theta_i = k_i v_b(t+\tau_i) \quad (\text{A.1-7})$$

Table A.1-5 lists the parameters that will be used in this model.

In order to simulate the relative excitation levels of the individual relay mirrors as described in Section 2.2.7, the  $k_i$ 's will be generated by a random draw (on the initial cycle only) from the uniform probability distribution function shown in Fig. A.1-4.

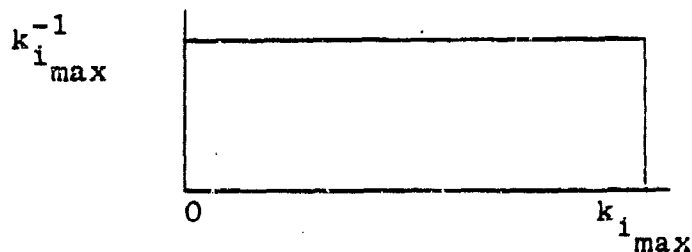


Figure A.1-4 PDF for Relay Mirror Vibration Gains

TABLE A.1-5  
RELAY MIRROR JITTER MODEL PARAMETERS

T-1860

SYMBOL	DEFINITION	VALUE
$\omega_{p_i}$	$i^{\text{th}}$ relay mirror natural frequencies in pitch	$(2\pi)5\text{Hz};$ $i = 1 \text{ to } 4$
$\xi_{p_i}$	$i^{\text{th}}$ relay mirror damping ratio in pitch	0.9; $i = 1 \text{ to } 4$
$\omega_{y_i}$	$i^{\text{th}}$ relay mirror natural frequency in yaw	$(2\pi)5\text{Hz};$ $i = 1 \text{ to } 4$
$\xi_{y_i}$	$i^{\text{th}}$ relay mirror damping ratio in yaw = .01; $i = 1,4$	0.9; $i = 1 \text{ to } 4$
$k_i$	$i^{\text{th}}$ relay mirror vibration input gain. Randomly chosen from a uniformly distributed probability density function on initial cycle.	*
$\tau_i$	$i^{\text{th}}$ relay mirror vibration input phase shift randomly chosen from a uniformly distributed probability density function on initial cycle.	$0 \leq \tau_i \leq \frac{2\pi}{\omega_{p_i}}$

$k_{i_{\text{max}}}$  is determined from the maximum expected mirror jitter variance by working backwards through the dynamics of the relay mirror and laser induced vibration models.

#### A.1.7 Beam Expander

Table A.1-6 lists the parameters that will be used to describe beam expander effects.

TABLE A.1-6  
BEAM EXPANDER PARAMETERS

T-1862

SYMBOL	DEFINITION	VALUE
M	Demagnification Factor	5
D	Output Aperture Diameter	1 m

## A.2 ATMOSPHERIC PROPAGATION EFFECTS

### A.2.1 Atmospheric Turbulence Models

Table A.2-1 lists the shaping filter parameters to be used in simulating atmospheric turbulence effects for the AMD scenarios; Table A.2-2 lists the filter parameters for the PC scenario. When driven by unity variance white noise, the spectral content of a given filter output approximates spectra generated by the methods of Hogge and Butts (Ref. 1).

TABLE A.2-1  
SHAPING FILTER PARAMETERS FOR AMD

T-1864

GENERAL FORM OF TRANSFER FUNCTION: $K \frac{abc}{d} \frac{(s+d)}{(s+a)(s+b)(s+c)}$					
MODE	K	a	b	c	d
x	$4.4 \times 10^{-7}$	14.14	659.5	659.5	$\infty$
y	$3.9 \times 10^{-7}$	14.14	659.5	659.5	$\infty$
$x^2 + y^2 - \frac{R^2}{2}$	$7.2 \times 10^{-8}$	28.25	1005.	1005.	$\infty$
$x^2 - y^2$	$1.3 \times 10^{-7}$	12.55	773.0	773.0	$\infty$
xy	$1.2 \times 10^{-9}$	1.410	22.00	880.0	.0157

TABLE A.2-2  
SHAPING FILTER PARAMETERS FOR PC

T-1863

GENERAL FORM OF TRANSFER FUNCTION: $K \frac{abc}{d} \frac{(s+d)}{(s+a)(s+b)(s+c)}$					
MODE	K	a	b	c	d
x	$2.6 \times 10^{-7}$	47.10	2200.	2200.	$\infty$
y	$2.4 \times 10^{-7}$	47.10	2200.	2200.	$\infty$
$x^2 + y^2 - \frac{R^2}{2}$	$3.3 \times 10^{-8}$	94.20	3350.	3350.	$\infty$
$x^2 - y^2$	$5.4 \times 10^{-8}$	41.80	2576.	2576.	$\infty$
xy	$6.0 \times 10^{-10}$	4.710	73.30	2932.	.0523



### A.2.2 Speckle Model

Figure A.2-1 is a block diagram of the speckle model developed in Section 2.3.3.

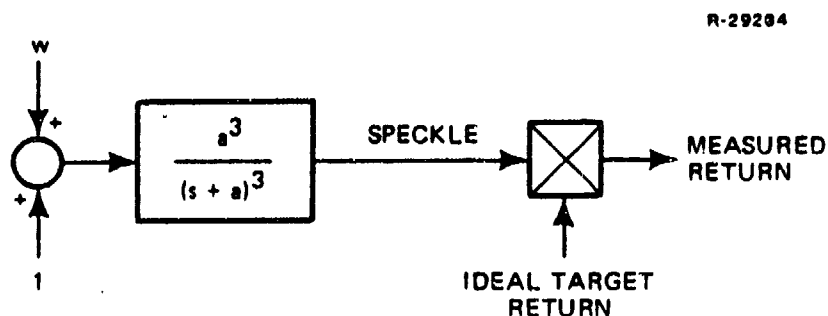


Figure A.2-1 Speckle Dynamic Model

For the AMD scenario:

$$a = 2\pi(2300\text{Hz}) \quad (\text{A.2-1})$$

$$\sigma_{\text{speckle}} = .3 \quad (\text{A.2-2})$$

### A.2.3 Receiver Model

The mathematical model for the photomultiplier presented in Section 2.2.8 is given by Eq. A.2-3. Table A.2-2 gives the parameter definitions and the values to be used in the system simulation. The critical parameter ratio is the signal to noise ratio of the photodetector; since  $N_a$  is simply a deterministic bias, it will be set to zero.

$$I_m = (I_t + N_a)K_{\text{pmt}} + N_{\text{pmt}} \quad (\text{A.2-3})$$

TABLE A.2-3  
RECEIVER MODEL PARAMETERS

T-1865

SYMBOL	DESCRIPTION	VALUE
$N_a$	Ambient Radiation Level	0.
$K_{pmt}$	Photomultiplier Gain	1.
$E(N_{pmt}^2)$	Standard Deviation of Photomultiplier Noise (white)	(.05) maximum target intensity